Transition Metal Complexes Anchored on Europium Oxide Nanoparticles

Joan Marie D. Zapiter

Thesis submitted to the faculty of the Virginia Polytechnic Institute and State University in partial fulfillment of the requirements for the degree of

Master of Science
in
Chemistry

Brian M. Tissue, Chair
Karen J. Brewer
James M. Tanko

Novermber 8, 2013
Blacksburg, Virginia

Keywords: lanthanide, spectroscopy, photochemistry, energy transfer, luminescence, inert-gas condensation, ruthenium, rhodium, iridium, bipyridine

Transition Metal Complexes Anchored on Europium Oxide Nanoparticles

Joan Marie D. Zapiter

ABSTRACT

Polypyridyl transition metal complexes containing ruthenium, rhodium and iridium centers are mainly studied due to their light absorbing and emitting properties. Lanthanide oxides such as europium oxide absorb light as well and exhibit strong luminescence and long lifetimes. The optical properties of these materials were significant especially in solar energy utilization schemes and optical applications. Energy transfer across a surface is important in several applications including phosphors and biomedical applications. Excited states of metal complexes with a carboxylate-containing ligand such as deeb = diethyl-2,2'-bipyridine-4,4'-dicarboxylate were studied on nanoparticle surfaces. In this work, $[Rh(deeb)_2Cl_2](PF_6)$, $[Ir(deeb)_2Cl_2](PF_6)$ and $[Ir(deeb)_2(dpp)](PF_6)_3$ were synthesized using the building block approach. The metal complexes were characterized using ^1H NMR spectroscopy, mass spectrometry, electronic absorption spectroscopy and electrochemistry. The ^1H NMR spectra of the complexes were consistent with those of their ruthenium analogs. Mass spectra contain fragmentation patterns of the $(M\text{-}PF_6)^+$ molecular ion for $[Rh(deeb)_2Cl_2](PF_6)$ and $[Ir(deeb)_2Cl_2](PF_6)$, and $(M\text{-}3PF_6)^{3+}$ molecular ions for $[Ir(deeb)_2(dpp)](PF_6)_3$. The electronic absorption spectrum of $[Rh(deeb)_2Cl_2](PF_6)$ shows a maximum at 328 nm, which is assigned as $^1\pi\rightarrow\pi^*$ transition. The electronic absorption spectrum of $[Ir(deeb)_2Cl_2](PF_6)$ shows maxima at 308 nm and 402 nm, which are assigned as $^1\pi\rightarrow\pi^*$ and metal-to-ligand charge transfer transitions, respectively. The $[Ir(deeb)_2(dpp)](PF_6)_3$ complex exhibits peaks due to $^1\pi\rightarrow\pi^*$ transitions at 322 nm and 334 nm. $[Rh(deeb)_2Cl_2](PF_6)$ has emission maxima from the ^3LF state at 680 nm and 704 nm for the solid and glassy solutions at

77 K, respectively. $[Ir(deeb)_2Cl_2](PF_6)$ has emission maxima from the ^{3}MLCT state at 538 nm in acetonitrile and 567 nm in the solid state at room temperature, with lifetimes of 1.71 μs and 0.35 μs, respectively. $[Ir(deeb)_2Cl_2](PF_6)$ has an unusually higher quantum yield than analogous compounds. $[Ir(deeb)_2(dpp)](PF_6)_3$ has emission maxima from the ^{3}IL state at 540 nm in acetonitrile and 599 nm in the solid state at room temperature, with lifetimes of 1.23 μs and 0.14 μs, respectively. Cyclic voltammetry of $[Ir(deeb)_2Cl_2](PF_6)$ and $[Ir(deeb)_2(dpp)](PF_6)_3$ yield reversible and quasi-reversible couples corresponding to deeb ligand and $Ir^{3+/+}$reductions, respectively. Attachment of the complexes were conducted by equilibration of complex solutions in acetonitrile with europium oxide nanoparticles. Europium oxide nanoparticles, which were synthesized by gas-phase condensation, have 11-nm diameters and exhibit sharp *f*-based luminescence in the visible and near IR regions. EDX, TEM, IR and reflectance spectroscopy measurements indicate substantial coating through various modes of attachment of the nanoparticle surface by the metal complexes while retaining the excited state properties of the metal complexes. Surface adsorption studies indicate monolayer coverage of the nanoparticle surface by the metal complexes, consistent with limiting surface coverages of previously reported analogous systems. Eu_2O_3 nanoparticles modified with $[Rh(deeb)_2Cl_2]^+$ exhibit minimal to no energy transfer from emission spectra, and a reduction in the lifetime at 77K could be due to the rhodium complex preventing the excitation of Eu^{3+}. Upon attachment of the Ir complexes $[Ir(deeb)_2Cl_2]^+$ and $[Ir(deeb)_2(dpp)]^{3+}$ on as-prepared nanoparticles, Eu^{3+} luminescence was observed for nanoparticles modified with iridium complexes at room temperature, which could be due to energy transfer among other possibilities. Efficiencies of 68% and 50%, and energy transfer rate constants of 1.1×10^{-5} and 1.0×10^{-5} were calculated from lifetime data for $[Ir(deeb)_2Cl_2]^+$ and $[Ir(deeb)_2(dpp)]^{3+}$ on Eu_2O_3 nanoparticles, respectively. Since iridium

complexes are used as components of light-emitting diodes, europium oxide nanoparticles modified with iridium complexes have potential in optical applications which make studies of these compounds interesting.

Acknowledgement

I wish to extend my sincerest gratitude to the following for their generous help in this work:

Profs. Karen Brewer and Brian Tissue for all the knowledge they have imparted and their invaluable help, guidance, patience and understanding.

Prof. Paul Deck, for his incredible concern and support for the graduate students in the Chemistry Department.

Profs. James Tanko, Gordon Yee and Diego Troya, for their useful comments and feedback.

Past and present members of the Brewer and Tissue groups, especially Shamindri Arachchige, Avijita Jain, Ran Miao, Mark Elvington, David Zigler, Sheng Zhao, Jared Brown, Matt Mongelli, Travis White, Sam Hopkins, Jessica Knoll, Jing Wang, Elise Naughton, Rongwei Zhou, Roberto Padilla, Gerry Manbeck and Wes Gordon, for all their help in the lab.

Prof. John Morris, Steve Burrow and the Morris group, for the IR measurements under vacuum.

David Hobart and Frank Cromer, for the EDX and XPS measurements.

Prof. Robert Moore, Gilles Divoux, Prof. Sarah Stoll and Michele Pablico-Lansigan, for the X-ray diffraction measurements.

Steve McCartney, for the SEM and TEM measurements.

John Burleson, Geno Iannacone, Hugo Azurmendi, Tom Glass, Tom Wertalik, Bill Bebout and Larry Jackson for their assistance in NMR, IR, MS, glassware and electronics trouble.

The Chemistry Dept. administrative staff, for always being wonderful in assisting students on everything.

Profs. Joe Merola, Alan Esker and T. Daniel Crawford, for their recommendations and faith in my abilities in teaching.

Jessica Lu, Paula Weiss, Hiro Motegi, for their friendship and moral support.

The Filipino community in Blacksburg/Christiansburg, especially Rob Rebodos, Jess Calata, Alan Batongbacal, Melanie Victoria, Jason Maupin, Jessie Luo, Roy Tan, Allan Sioson, Richard Yao, Lynn Rallos, Noah Badayos, Cathy Aragon, Jen Colcol, and the Folledo, Ozaraga, Buyhoff and Ballweg families, for being my home away from home.

And to my family: Mummy, Janice, Karla and Cholo, for always being there for me as I am for them.

Table of contents

List of Figures

List of Tables

List of Abbreviations

1D	One-dimensional
2D	Two-dimensional
5,6-Mephen	5,6-dimethyl-1,10-phenanthroline
A	acceptor
ATR-FTIR	Attenuated Total Reflectance-Fourier Transform Infrared
COSY	Correlation Spectroscopy
CT	Charge Transfer
bpy	2,2′-bipyridine
Cy5	Cyanine 5
D	donor
dcb	2,2′-bipyridine-4,4′-dicarboxylic acid
deeb	diethyl-2,2′-bipyridine-4,4′-dicarboxylate
DMF	dimethylformamide
dpp	2,3-bis(2-pyridyl)pyrazine
DSSC	Dye-Sensitized Solar Cell
ET	Energy Transfer
FAB-MS	Fast Atom Bombardment-Mass Spectrometry
HOMO	Highest Occupied Molecular Orbital
IL	Internal Ligand
IR	Infrared
LB	Langmuir-Blodgett

LED	Light Emitting Diode
LMCT	Ligand-to-Metal Charge Transfer
MLCT	Metal-to-Ligand Charge Transfer
LF	Ligand Field
mcb	4-methyl-2,2′-bipyridine-4′-carboxylic acid
NMR	Nuclear Magnetic Resonance
NOESY	Nuclear Overhauser Effect Spectroscopy
NP	Nanoparticle
phen	1,10-phenanthroline
ppy	2-phenylpyridine
QD	Quantum Dot
RT	Room temperature
SEM	Scanning Electron Microscopy
TBP	Trisbipyridin
UV	Ultraviolet
EDX	Electron Dispersive X-ray

Chapter 1 - Introduction and Motivation

1.1 Thesis Statement

Light absorbing and emitting ruthenium, rhodium and iridium polypyridyl complexes anchored onto luminescent europium oxide nanoparticles through carboxylate groups were prepared and studied to determine if energy transfer could occur between metal complexes and nanoparticles, and if so, determine how the energetics of excited states involved and other factors would affect the extent of energy transfer.

1.2 Europium Oxide Nanoparticles

Lanthanide oxides such as Eu_2O_3 are used in optical,[1,2] electronic,[3] and catalytic[4] applications because of their optical properties. For instance, Eu^{3+} doped in Y_2O_3, being the red phosphor coating for early tricolored fluorescent lamps and cathode ray tubes, is vital in the development of this type of materials.[5,6] This is due to the fact that Eu^{3+} and other lanthanide ions exhibit strong and sharp emission bands in the visible and near IR regions with long lifetimes because of Laporte- and spin-forbidden transitions from the 4f orbitals.[7-9] Dieke summarized the different energy states of Eu^{3+} and other trivalent lanthanide ions, as shown in Figure 1.1.[7,8] Energy states are designated using term symbols $^{2S+1}L_J$ where S = total spin quantum number, L = atomic term symbol for the total orbital quantum number and J = multiplet energy level that can be split up to 2J + 1 sublevels. Excited state energies of the 4f orbitals are only slightly changed with coordination environment because of shielding from the outer 5s and 5p electrons, a factor which reduces complications in employing lanthanides in energy transfer schemes. The spectrum of Eu_2O_3 has bands due to relaxation of the ^5D_J states upon excitation from the $^7F_0$ ground state, as observed in free Eu^{3+}, as well as a ligand-to-metal charge transfer

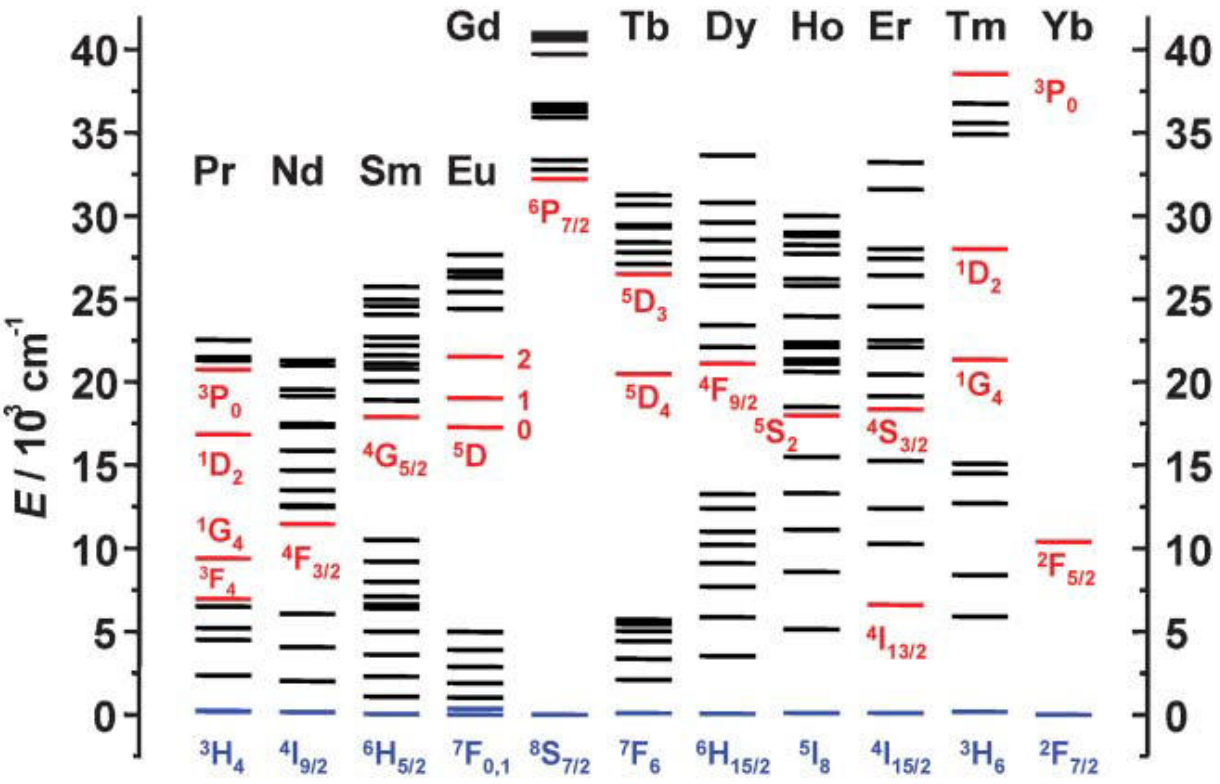

Figure 1.1. Dieke energy diagram of trivalent lanthanide ions.[10-16]

(LMCT) band that is formed from exciting an electron from an O^{2-} 2p orbital to a 4f Eu^{3+} orbital.[7,8] Unlike the sharp 4f transitions, the CT state is broad and its energy is highly dependent on the coordination environment. In the emission spectrum, the transition at $^5D_0 \rightarrow {}^7F_2$ at around 615 nm is most intense, although the $^5D_0 \rightarrow {}^7F_1$ and $^5D_0 \rightarrow {}^7F_3$ are also observable. Also, due to the forbidden nature of the 4f transitions, emission lifetimes are in the order of microseconds to milliseconds.

Lanthanide ions in phosphors are mostly incorporated in a solid matrix because higher luminescence quantum efficiencies are achieved in ionic solids than in solutions due to lower vibrational frequencies and consequently lower nonradiative loss in solids.[6] In this work, Eu_2O_3 is chosen as a model system due to the inherent thermodynamic stability of lanthanide oxides[17] and to avoid inhomogeneous dopant distribution despite the reduced luminescence.[18]

Nanomaterials have gained increasing interest due to technological advances and their enhanced optical, electronic and magnetic properties due to size, confinement, and surface and interfacial effects.[19,20] Although Eu_2O_3 nanoparticles have decreased luminescence quantum efficiency and lifetimes compared to bulk material due to surface defects,[21-24] coupling of vibrational states and emission wavelengths are not critically dependent on size compared to other nanometer-sized particles, such as quantum dots.[25] Nanoparticles also provide high surface-to-volume ratios for efficient addition of surface functionality.

Luminescence from lanthanide ions are rarely obtained by direct excitation due to the weak oscillator strength of *4f-4f* transitions.[26] Hence, sensitizers are usually employed for light absorption which consequently affords lanthanide luminescence by energy transfer (ET). Lanthanides can be sensitized *via* ET because they have large Stokes shifts and narrow emission bands which prevent donor emission from leaking into the acceptor emission band.[27,28] *d*-block transition metal complexes are known to sensitize lanthanide luminescence in hybrid systems[29] mainly due to their broad metal-to-ligand (MLCT) and internal ligand (IL) absorption bands with high molar absorptivities in the UV and visible regions.[29,30] Inorganic metal complexes can be attached on the surface of lanthanide oxides in a similar manner to the metal oxides commonly used in DSSCs. The study of energy transfer between europium oxide nanoparticles and metal complexes would be useful for phosphor applications, sensing or in DSSCs where metal oxide-metal complex interactions are prevalent.

1.3 Light-Absorbing Transition Metal Complexes

Transition metal complexes containing polypyridyl ligands such as 2,2'-bipyridine (bpy) have been studied extensively due to their ability to absorb light and form excited states that are crucial for several applications including photovoltaics and catalysis. The use of metal

complexes in photochemical reactions is prevalent due to several advantages.[24,25] One is that they have large molar absorptivities and quantum yields throughout the UV and visible regions of the electromagnetic spectrum, a property that is important for efficient use of solar energy. Another is that changing the metal center in the complex not only varies the absorption and emission maxima but the type of excited states that form and hence the deactivation pathways that they go through. Ruthenium complexes, for instance, form metal-to-ligand charge transfer (MLCT) states that are useful for electron transfer reactions. Photophysical and chemical properties can also be easily tuned by slight variations in the ligands while maintaining the metal complex structure and type of excited states involved.[19,31]

Ruthenium complexes are among the most studied of these systems because they absorb and emit light in the visible region due to MLCT transitions. This type of excited state occurs when the metal complex absorbs light and promotes an electron from its highest occupied molecular orbital (HOMO) that has primarily metal character (designated as a metal($d\pi$) orbital) to its lowest unoccupied molecular orbital (LUMO) that is mostly ligand in character (usually designated as a π^* orbital). For ruthenium complexes like $[Ru(bpy)_3]^{2+}$, absorption of light yields a ^{1}MLCT excited state which consequently undergoes intersystem crossing to form an emissive ^{3}MLCT state.[32,33] This excited state deactivates *via* electron or energy transfer quenching, and/or radiative or nonradiative decay to the ground state. The electron transfer pathway makes ruthenium complexes to be predominantly used in solar energy conversion schemes, *e.g.* in dye-sensitized solar cells (DSSCs).[32] In most of these systems, a ruthenium complex acts as a sensitizer which absorbs light and transfers electrons to a semiconductor nanoparticle such as TiO_2. The metal complex is usually covalently attached to the oxide surface *via* ligands that contain carboxylate groups, such as the deeb ligand (where deeb = 4,4'-$(COOCH_2CH_3)_2$-bpy).

Because most of the information on metal complexes attached on metal oxide surfaces are regarding DSSCs, deeb-containing ruthenium complexes $[Ru(deeb)_2Cl_2]$ and $[Ru(deeb)_2dpp](PF_6)_2$ used in this work serve as starting points and references to compare properties of metal complexes on Eu_2O_3 nanoparticles with those on other known metal oxide surfaces.

Rhodium complexes, on the other hand, form internal ligand (IL) and ligand field (LF) excited states upon absorption of light. An IL state forms by promoting an electron from a ligand π orbital to a ligand π^* orbital while a LF state forms by excitation from a metal $d\pi$ orbital to a metal $d\sigma^*$ orbital. Because excitation to LF states is symmetry-forbidden, their peaks are weak and have low extinction coefficients in the absorption spectrum. They also undergo fast nonradiative decay at room temperature but display broad emission bands at low temperatures. Rhodium compounds are ideal in energy transfer studies due to the absence of MLCT states that usually lead to electron transfer. Since upon excitation the electron is promoted to a $d\sigma^*$ LUMO in a LF state, which is lower in energy compared to the ligand π^* LUMO in an MLCT state, rhodium compounds are usually but not exclusively used as electron or energy acceptors and shuttles.[34-36] In this work, the rhodium complex $[Rh(deeb)_2Cl_2](PF_6)$, was prepared to determine if energy transfer from Eu_2O_3 to the metal complex could occur.

Iridium complexes are less studied than their ruthenium and rhodium counterparts due to synthetic difficulties.[37,38] They are similar in parts to both ruthenium and rhodium complexes in that absorption of a photon leads to formation of a MLCT or an IL excited state, depending on the electron density around the metal. If the ligands were anionic, in the case of halide or cyclometallating ligands, the emissive state tends to be a MLCT state because there is sufficient charge density on the metal; otherwise, emission is due to an IL excited state.[33] The

$[Ir(bpy)_2Cl_2](PF_6)$ complex for instance has an emissive ^{3}MLCT state at 510 nm.[33,39] Regardless, iridium complexes produce these long-lived excited states that exhibit strong blue and green emissions harnessed for LEDs,[40-44] light-emitting electrochemical cells (LECs),[33] bioimaging[33] and photocatalysis.[45] In spite of the possibility of forming MLCT states that are usually involved in electron transfer schemes, some Ir complexes have been reported to undergo energy transfer instead. Several supramolecular systems containing Ru(II) and Ir(III) moieties were reported to undergo energy transfer from the iridium to the ruthenium unit.[46] More importantly, a number of accounts of energy transfer from an Ir(III) to a Eu(III) unit were reported for systems used for white light emitting diode (LED) applications.[47-50] These systems will be discussed in more detail in section 1.5.

1.4 Metal Complexes on Metal Oxide Nanoparticles

An active area of research involving nanomaterials is the study of inorganic complexes bound to nanoparticles to form "heterosupramolecular" assemblies,[43] which have applications in solar energy conversion[11] and biological and chemical sensing.[11,12,51-54] These systems exploit the light absorbing properties of coordination complexes and the high surface-to-volume ratios of nanoparticles for efficient addition of surface functionality. Dye-sensitized solar cells use the large surface area of metal-oxide nanofilms for efficient electron transfer from photoexcited transition-metal polypyridyl complexes.[54-58] In DSSCs, ligands with carboxylic acid-,[11,36,51,52,59,60] carboxylate ester-,[13,14,51,61-63] and phosphonate-based[7,8] groups are known to covalently attach metal complexes onto the surface of metal oxide nanomaterials. Carboxylic acid-based ligands are the most common in anchoring ruthenium complexes to metal oxides such as TiO_2 because they are used in the DSSC pioneer studies, yield the best light energy-to-electrical energy conversion efficiencies to date, and have strong surface adsorption to the metal-

oxide surface.[62,64] A few of these ligands include 2,2'-bipyridine-4,4'-dicarboxylic acid (dcb)[16] and ina,[51,61-63] which use hydroxyl groups on the metal oxide surface in attaching themselves on the oxide, as in Figure 1.2. G. Meyer and co-workers have exploited the ester analog of dcb, *i.e.* deeb[13,14] (4,4'-$(COOCH_2CH_3)_2$-bpy), as well as other ester-based ligands such as deebq (4,4'-diethylester-2,2'-biquinoline)[10-16] and eina (4-ethyl ester pyridine),[65] for preparing complexes for surface attachment on TiO_2. The ester groups in these ligands are known to be hydrolyzed into its carboxylate form in solution and in the presence of surface hydroxyl groups on the metal oxide nanoparticle.[66] Using deeb instead of dcb affords less complications in synthesis as the pH of the reaction need not be considered in isolating the ligand and its complexes.[11,16] The ester group also serves as a spectroscopic probe for easier structure elucidation. In this work, metal complexes containing the deeb ligand were prepared and anchored on europium oxide nanoparticles.

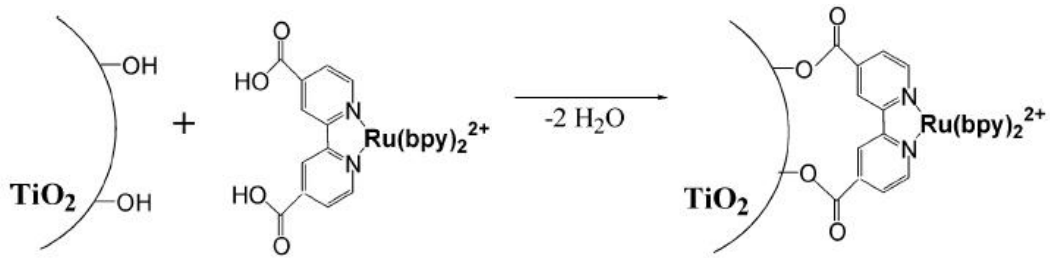

Figure 1.2. Attachment of a ruthenium complex to a TiO_2 surface. [16]

1.5 Energy Transfer

When a molecule absorbs light, it forms an excited state (eq. 1) which could be deactivated back to the ground state *via* several mechanisms. One pathway for excited-state decay is energy transfer, wherein the excited molecule transfers energy by acting as a donor (D) that excites an acceptor (A) molecule which quenches the excited state of D (eq. 2).

$$D + h\nu \longrightarrow D^* \qquad (1)$$

$$D^* + A \longrightarrow D + A^* \qquad (2)$$

The study of energy transfer is important because it can be used to quench the luminescence or reactivity of the donor excited state and induce luminescence of the acceptor species as its excited state deactivates to a lower energy state. ET is used in bioanalysis, sensing and imaging[16] and in optoelectronic devices such as light emitting diodes (LEDs) and phosphors,[67-71] most of which integrate lanthanide ions as key components in the ET process. ET can be detected by observing: (a) the absorption bands of the donor D in the excitation spectrum of the acceptor A's emission; (b) the emission of the A upon selective excitation of D; or (c) a decrease in the lifetime of the emission of D, among others.[72-74]

Energy transfer occurs through either the Förster[6,70] or the Dexter[75] mechanisms. The Förster mechanism occurs as a simultaneous electrostatic coupling of the transition dipoles of the donor and acceptor states, while the Dexter mechanism occurs as a simultaneous excited electron exchange from the donor and acceptor states (Figure 1.3).[76]

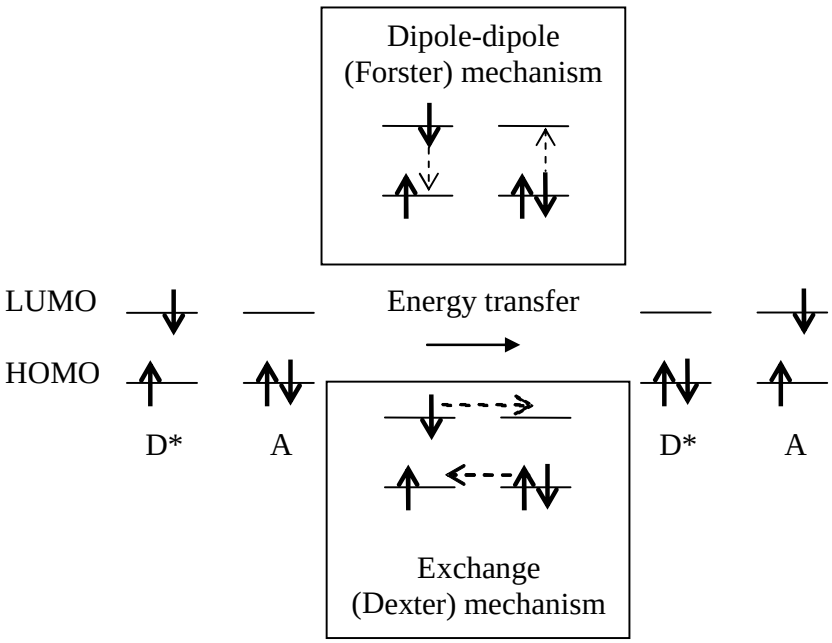

Figure 1.3. Schematic of formation and decay of charge-transfer excited states.[77]

The Förster mechanism of ET involves donor and acceptor excited-state dipole interactions that are quantified through the rate constant expression, $k_{Förster}$ (eq. 3):

$$k_{Forster} = \left(\frac{9000 \ln 10}{128 \pi^6 N}\right) \frac{\kappa^2}{n^4 \tau_D R^6} \int_0^\infty E_D(\bar{\nu})\, \varepsilon(\bar{\nu}) \frac{d\bar{\nu}}{\bar{\nu}^4} \qquad (3)$$

where N is Avogadro's number, κ is the dipole orientation factor, n is the refractive index of the solvent, τ_D is the intrinsic or radiative lifetime of the excited donor, R is the donor-acceptor distance, and the integral is an estimate of the donor-acceptor excited-state spectral overlap. In the integral expression, $\bar{\nu}$ is the wavenumber of the donor emission and acceptor absorption overlap, $E_D(\bar{\nu})$ is the normalized emission spectrum of the donor and $\varepsilon(\bar{\nu})$ is the normalized absorption spectrum of the acceptor.[77] The Dexter mechanism of electronic exchange, on the other hand, is quantified through the rate constant expression, k_{Dexter} (eq. 4):

$$k_{Dexter} = \frac{2\pi}{\hbar} J_0 e^{-R/L} \int_0^\infty E_D(\bar{\nu})\, \varepsilon(\bar{\nu}) d\bar{\nu} \qquad (4)$$

where the quantity $J_0 e^{-R/L}$ is the transfer matrix element and the integral is a similar overlap integral expression as in equation (3). J_0 is the diagonal exchange approximation between D and A in nearest-neighbor positions, R is the donor-acceptor distance, and L is a constant termed as the "effective average Bohr radius".[75,78] From these mechanisms, it can be seen that the extent of donor-acceptor spectral overlap, which is a measure of how the D and A energies match up, plays an important part in ET.

The easiest measure of ET is the quantum yield efficiency, E, which can be obtained from: a) the decrease in donor quantum yield, b) the donor intensity decay curve, c) the excitation spectrum monitoring acceptor emission, and d) the increase in intensity of acceptor emission.[76,79,80] The quantum yield represents the efficiency of a photochemical reaction based

on the number of molecules undergoing a change per photon absorbed.[77,78,81,82] In a) for instance, the efficiency *E* (eq. 5) can be defined from the ratio of the quantum yields of the donor with and without the presence of transfer, ϕ_{DA} (eq. 6) and ϕ_D (eq. 7), respectively:

$$E = 1 - \frac{\phi_{DA}}{\phi_D} \qquad (5)$$

$$\phi_{DA} = \frac{k_D}{k_D + k_{D_i} + k_T} \qquad (6) \qquad\qquad \phi_D = \frac{k_D}{k_D + k_{D_i}} \qquad (7)$$

where k_D is the radiative (fluorescence or phosphorescence) decay rate constant of the donor without the presence of the acceptor, k_{Di} is the sum of the non-radiative (internal conversion and/or intersystem crossing) rate constants of the donor without the presence of the acceptor, and k_T is the non-radiative ET rate constant:[77,82]

$$k_T = (k_D + k_{D_i})\left(\frac{R_0}{R}\right)^6 \qquad (8)$$

In equation (8), R_0 is the Förster distance, *i.e.* the distance at which the rate (or probability) of transfer equals the sum of all other rates (or probabilities) for deactivation of the donor excited-state or the distance at which $k_T = k_D + k_{D_i}$.[78] Experimentally, quantum yields are determined by comparison of the wavelength integrated intensity of the emitting species to that of a standard:[78]

$$\phi = \phi_r \frac{I}{I_r}\frac{A_r}{A}\frac{n^2}{n_r^2} \qquad (9)$$

where ϕ is the quantum yield, *I* is the integrated emission intensity, *A* is the absorbance at the excitation wavelength, *n* is the refractive index of the solvent and the subscript *r* refers to the reference fluorophore of known quantum yield.[77] This comparison technique, also known as chemical actinometry, allows the determination of photon flux absorbed by a system of specific geometry and in a well-defined spectral domain.[77]

ET efficiency can also be determined through the donor emission intensity decay in the time or frequency domains (option b) on p. 9),[77,83] which leads to determination of the excited-state lifetime, τ. The lifetime of a species is the time needed for its concentration to decay to 1/*e* of its original value:[78]

$$\ln\left(\frac{I_t}{I_i}\right) = -\frac{1}{\tau}t \qquad (10)$$

where the I_i is the emission intensity at time = 0 and I_t is the emission intensity at time *t*. It is related to the radiative and non-radiative decay rate constants as given in the lifetime expressions for the donor with (eqn. 11) and without (eqn. 12) the presence of an acceptor:

$$\tau_{DA} = \frac{1}{k_D + k_{D_i} + k_T} \qquad (11) \qquad\qquad \tau_D = \frac{1}{k_D + k_{D_i}} \qquad (12)$$

Thus, energy transfer corresponds to a shortening of the donor's lifetime and the efficiency may be expressed as:

$$E = 1 - \frac{\tau_{DA}}{\tau_D} \qquad (13)$$

Although both quantum yield and lifetime determinations give the best information, efficiencies obtained from lifetimes are usually preferred over those from quantum yields because they can be obtained with greater accuracy and there is no need to correct for trivial reabsorption or secondary fluorescence.[77] Trivial reabsorption occurs when the excited donor indirectly transfers energy to the acceptor by emitting another photon that excites the acceptor. Secondary fluorescence, on the other hand, is fluorescence emitted by another species that is not involved in the ET process, *e.g*. fluorescence from the solvent.[78]

Following the excitation instead of the emission spectrum of may also be used to measure ET, as stated in option c) (p. 9). This could be done because phosphorescence is much easier

observed than absorption, and it is easier to measure a very low light intensity than to measure a very small change in a high light intensity due to very weak light absorption.[78] The excitation spectrum provides information on which excited states lead to a particular emissive state, and if energy transfer occurs, donor excitation leading to acceptor emission could be observed in the excitation spectrum. If the emission is too weak on the other hand, transient absorption spectroscopy allows measurements of the absorption spectra of excited states by continually replenishing excited state populations using an intense laser pulse.[84]

An increase in acceptor emission intensity (option d), p. 9) and a decrease in donor emission intensity are the most common albeit inconclusive signs for energy transfer because the acceptor tends to be excited at the donor excitation wavelength and emits on its own, without energy transfer. ET efficiency calculations using emission intensities can be done with eq. 14:[77]

$$E = \frac{\varepsilon_A(\lambda_D^{ex})}{\varepsilon_D(\lambda_D^{ex})}\left\{\frac{F_{DA}(\lambda_A^{em})}{F_A(\lambda_A^{em})} - 1\right\}\left(\frac{1}{f_D}\right) \qquad (14)$$

where $\varepsilon_A(\lambda_D^{ex})$ and $\varepsilon_D(\lambda_D^{ex})$ are the extinction coefficients of the acceptor and donor at the donor excitation wavelength (λ_D^{ex}), $F_{DA}(\lambda_A^{em})$ and $F_A(\lambda_A^{em})$ are the acceptor emission intensity with and without the donor at the acceptor emission wavelength (λ_A^{em}), respectively, and f_D is the fractional labeling with the donor. Calculating efficiencies using this method relies on how emission intensities are obtained. Acceptor concentrations must be precisely the same for the samples with and without the donor; otherwise, the donor emission profile must be subtracted from the emission of the D-A pair.[85]

Lanthanides are used in energy transfer schemes because they have large Stokes shifts and narrow emission bands which prevent donor emission from leaking into the acceptor emission band. Energy transfer studies involving Eu^{3+} in non-molecular solids are usually

conducted to improve phosphor properties for fluorescent lighting, lasers and displays. Higher luminescence quantum efficiencies are achieved in ionic solids than in solutions because of lower vibrational frequencies and consequently lower nonradiative loss.[85] Luminescence from Eu^{3+} is rarely obtained by direct excitation due to the weak oscillator strength of 4f-4f transitions.[41-45,86]. Hence, sensitizers are usually employed for light absorption which consequently affords lanthanide luminescence by energy transfer. Other lanthanide ions such as Tb^{3+} are known to sensitize Eu^{3+} emission in glasses,[17] thin films,[87] polymer matrices,[88] and crystalline Y_2O_3.[89] In all cases, quenching of the Tb^{3+} emission and enhancement of Eu^{3+} emission were observed and attributed to energy transfer. In some works, the matrices themselves such as YVO_4,[90,91] ZnO,[92] and Ga_2O_3[93] transfer energy to Eu^{3+} and effect the Eu^{3+} emission.

In solution, a number of ligands, including polyaminocarboxylates, macrocyclic receptors, β-diketonates and acyclic Schiff base derivatives, have been used to form chelates of Eu^{3+} to yield emission for biochemical and sensing applications.[94] Other systems employ d-block metal chelates such as Cr^{3+}, Ru^{2+}, Os^{2+} and Ir^{3+} polypyridinecarboxylate complexes as sensitizers to take advantage of longer-lived excited states. One system, shown in Figure 1.4A, involves iridium fluorinated polypyridyl complexes connected to a Eu^{3+} chelate *via* carboxylate groups.[95] The iridium monometallic unit absorbs in the UV region to undergo π-π* transitions and emits blue light with maxima at 460 and 490 nm. Quantum yield of the iridium unit increases by 10% when the carboxylate moiety is present in the ligand. The terpyridine-capped europium unit emits red light centered at 615 nm, which is typical for such complex. When the system is excited at 400 nm, where only the iridium complexes have appreciable absorption, white light emission is observed that results from a combination of the blue and red emission from the

iridium and europium moieties, respectively, and thus the system can be used as a component of white LEDs. Reduction in the iridium unit lifetime from 1400 ns in solution to 480 ns in the trimetallic complex is attributed to energy transfer (E = 38%) from iridium to europium. Other similar systems that use phen,[41] non-fluorinated ppy and π-extended bridging ligands[42,44] on the Ir unit have also been. Another study reports an increase in Eu^{3+} emission intensity when an iridium complex is adsorbed on Eu^{3+}-containing Langmuir-Blodgett films.[43]

Some systems, on the other hand, take advantage of both molecules and ionic solid surfaces. An iridium complex whose structure is shown in Figure 1.4B was adsorbed on decatungstoeuropate $[Eu(W_5O_{18})_2]^{9-}$ Langmuir-Blodgett (LB) films.[43] A five-fold decrease in iridium emission intensity was observed. Europium emission was not observed for films with 1:1 ratio of Eu^{3+} and Ir^{3+}, but could be observed when the iridium complex concentration was diluted on the LB film surface with dimethyldioctadecylammonium bromide. Energy transfer, however, was not confirmed because excitation spectra monitoring at the europium and iridium emission only show contribution from the individual species.[40]

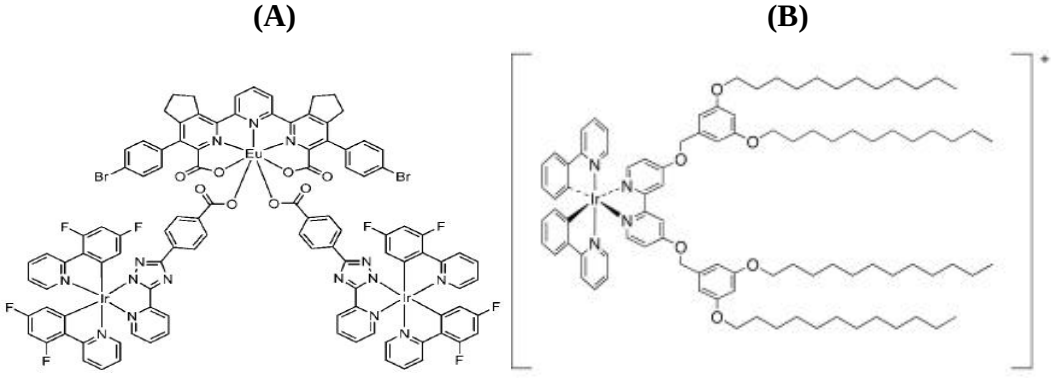

Figure 1.4. Structure of (A) an Ir-Eu-Ir system that demonstrates $Ir^{3+} \rightarrow Eu^{3+}$ energy transfer for emitting white light,[41] and (B) an iridium complex adsorbed on $[Eu(W_5O_{18})_2]^{9-}$ Langmuir-Blodgett films.[43]

One noteworthy study that employs Eu^{3+} in the donor nanoparticle and a single organic chromophore instead of a metal complex as acceptor is one that has Eu^{3+} doped in yttrium vanadate nanoparticles with cyanine 5 (Cy5) on the surface.[40] Cy5 is attached to the surface of the nanoparticle through carboxylate groups, as shown in Figure 1.5A, by equilibrating aqueous solutions of the nanoparticle with a solution of the dye for 45 minutes. The donor-acceptor spectral overlap is shown in Figure 1.5B. Fluorescence intensity and lifetime measurements yield ET efficiencies of 59% and 21% respectively, the discrepancy of which the authors account to the difference in the distances of the surface and core Eu^{3+} ions from Cy5. This factor can be circumvented if the nanoparticles have uniform particle sizes, and this can be well-achieved using methods that promote slow growth of the nanoparticles, such as gas phase condensation methods, instead of solution-based methods.[96-98]

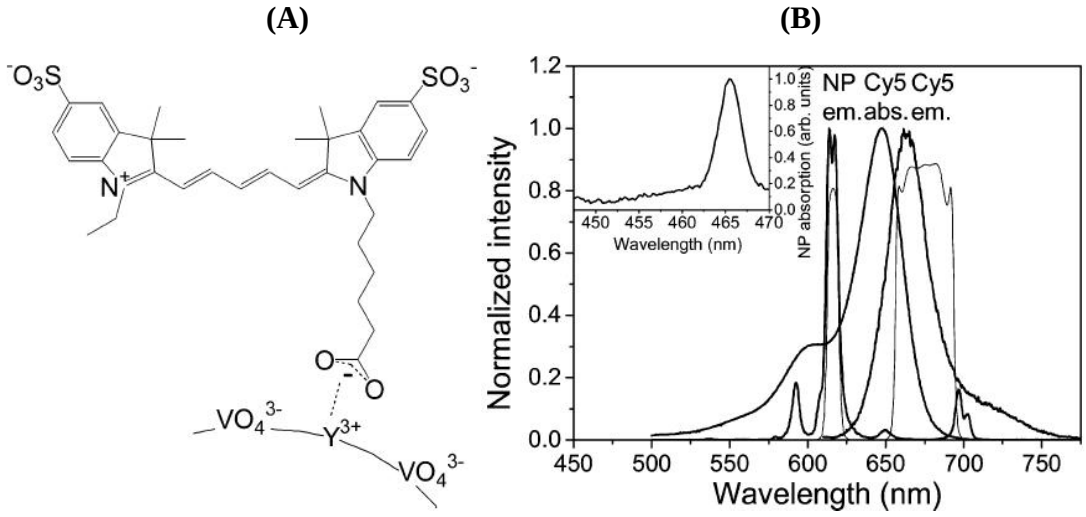

Figure 1.5. (A) Schematic of cyanine 5 attached to the Eu^{3+}:YVO_4 nanoparticle surface; (B) Emission spectrum of Eu^{3+}:YVO_4 nanoparticle (inset shows absorption spectrum), and absorption and emission spectra of cyanine 5.[22]

Energy transfer involving Eu^{3+} complexes on surfaces have also been reported. One system involves a europium complex with dibenzoylmethanate (DBM) and 4,4'-di-tert-2,2'-

bipyridine (DB-bpy) ligands (Figure 1.6A) combined with arachidic acid for forming and controlling the surface layers of TiO_2 Langmuir-Blodgett films. A decrease in the intensity ratio of the $^5D_0 \rightarrow {}^7F_2/{}^5D_0 \rightarrow {}^7F_1$ transitions of the Eu^{3+} complex in the LB films compared to the complex in solution was attributed to ET from TiO_2 to the Eu^{3+} complex.[96-98] The authors explained the emission intensity difference in terms of a change in chemical environment, $^5D_0 \rightarrow {}^7F_2$ being an electric dipole transition dependent of the chemical environment while $^5D_0 \rightarrow {}^7F_1$ being a magnetic dipole transition independent of the chemical environment.[99] Another system wherein the authors claim ET from fluorescence intensity changes is $[Eu(phen)_4](NO_3)_3$ on $(CH_3)_3$Si-MCM-41 nanostructured molecular sieve, wherein the europium complex is treated as a guest molecule encapsulated in the molecular sieve channels. For the Eu complex-molecular sieve system, an increase in the $^5L_0 \rightarrow {}^5D_0$ Eu^{3+} emission intensity at 349 nm relative to the unoccupied molecular sieve is observed which is attributed to ET from the molecular sieve to the complex.[99] No direct comparison, however, between the Eu complex emission intensities in solution and in the molecular sieve is shown to confirm that the increase in emission intensity was due to the ET from the molecular sieve.

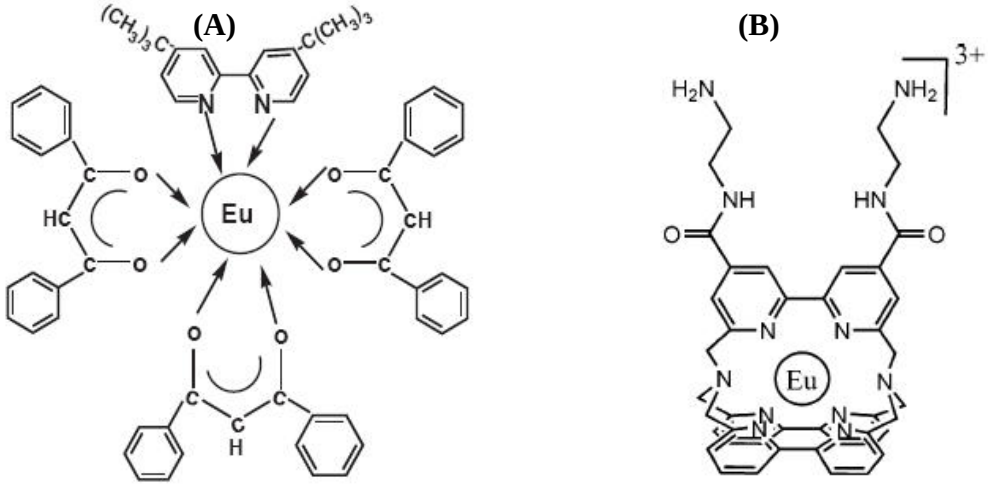

Figure 1.6. Structure of (A) $[Eu(DBM)_3(DB\text{-}bpy)]^{3+}$;[100] and (B) $[Eu(TBP)]^{3+}$ complex.[99]

Quantum dot (QD) semiconductor nanoparticles have been used as ET acceptors with europium complexes in biological studies. Hildebrandt and co-workers have studied $[Eu(TBP)]^{3+}$ and $[Ln(6\text{-}CO_2bpy)_2]^{3+}$ (Ln=Tb, Eu) complexes on CdSe quantum dots used in time-resolved fluoro-immmunoassays.[55,58] The $[Eu(TBP)]^{3+}$-QD system consists of a trisbipyridin (TBP) europium cryptate (Figure 1.6B) labeled by streptavidin for the donor and biotin-QD as acceptor. The QD is protected with a ZnS shell (for narrowing emission bands) and subsequently coated with a polymer-biotin complex (biotin-QD). Förster resonance ET experiments yield 62% ET efficiency and a Forster distance of 83 Å.[55-58] In the $[Ln(6\text{-}CO_2bpy)_2]^{3+}$-QD systems, the terbium or europium complex, which contains two 6-carboxybipyridyl ligands and a hydroxysulfosuccinimide-functionalized glutamate molecule as exemplified through the Tb complex in Figure 1.7A, are used as labels for streptavidin (LnL-Strep). The streptavidin-biotin binding process serves as a model for all biological recognition processes. Extensive overlap of the donor emission spectrum, as exemplified by $[Tb(6\text{-}CO_2bpy)_2]^{3+}$, with the QD acceptor absorbance spectrum is shown in Figure 1.7B. The use of lanthanide-containing systems takes advantage of the strong and narrow luminescence that prevents the Tb complex emission from leaking into the QD emission. A strong increase in the emission intensity ratio at the Biotin-QD and LnL-Strep maxima is observed when Biotin-QD concentration is increased resulting from ET to the quantum dots from the Ln complexes. Luminescence decay lifetime measurements of the donor-acceptor assembly yield an ET efficiency of at most 67% along a Förster distance of 87 Å for TbL-strep/biotin-QD, and 52% and 95 Å for EuL-strep/biotin-QD.[55,58] The relatively large effective Förster radii in these systems are indicative of the extensive overlap of the lanthanide donors and QD acceptors.[55-57]

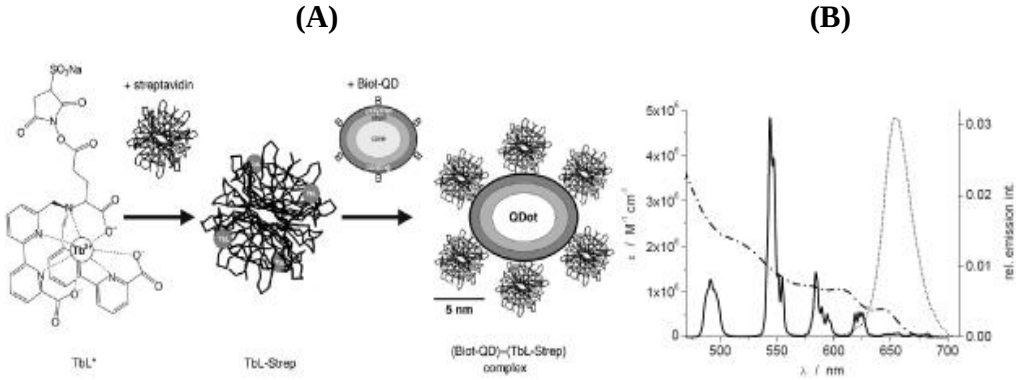

Figure 1.7. (A) Schematic of CdSe/ZnS quantum dot-biotin (Biotin-QD) combined with $[Tb(6\text{-}CO_2bpy)_2]^{3+}$-streptavidin (TbL-Strep) complex; (B) Normalized emission spectrum of TbL (---), and emission (····) and absorption spectra of Biotin-QD (-·--·).[55]

Ruthenium complexes have also been used with CdSe QDs to study emission quenching. Mattoussi and others demonstrated that comparable donor and acceptor radiative lifetimes aside from a substantial spectral overlap are needed for ET to take place.[55-58] No decrease in both donor emission intensity and lifetime, and therefore no ET, was observed in each of three different organic fluorophore-CdSe/ZnS QD pairs even if substantial spectral overlap is evident. The authors attribute this to the fast radiative decay rate of the dye donors compared to the slow ET decay rate in the presence of the acceptor. To prove this hypothesis, $[Ru(bpy)_2(ITC)](PF_6)_2$ (ITC = isothiocyanatophenanthroline), a donor that has a longer lifetime (~350 ns) than the organic dyes, is used with the QD. A significant decrease in the lifetime of the ruthenium complex from 419 ± 15 ns to 160 ± 12 ns was observed which indicates ET. However, steady-state fluorescence shows a strong emission due to direct excitation of the QD acceptor which renders the lifetime measurements inconclusive.[101,102] Quenching of CdSe quantum dot emission upon attachment of $[Ru(mcb)_2(bpy)]^{2+}$ is also observed from emission intensity and transient absorption electron dynamics experiments by Sykora *et al.*[102] In spite of this, there is a small

spectral overlap between the QD and the metal complex, and thus they account the emission intensity changes to electron transfer.[103]

1.6 Summary of Thesis

The goal of this work is to develop transition metal complexes that could be attached on the surface of Eu_2O_3 nanoparticles to study energy transfer between the metal complexes and the nanoparticles. Energy transfer is an important phenomenon observed on lanthanide-containing materials for various purposes, including phosphors, sensors and materials for solar energy conversion. Polypyridyl metal complexes containing ruthenium, iridium and rhodium are known as good light absorbers and emitters, which are essential properties for energy transfer studies. The ruthenium complexes containing the deeb ligand used in this work serve as standards for comparative studies of the metal complexes on Eu_2O_3 nanoparticles. The rhodium and iridium complexes were used to study energy transfer from and to the nanoparticles, respectively. Chapter 2 contains procedures on the synthesis and characterization of the materials used in this study. In Chapter 3, results on the synthesis, structure elucidation and photophysical characterization of the individual metal complexes and nanoparticles are presented. The metal centers and nature of the complexes were carefully chosen to achieve energies and properties that are optimal for energy transfer. Chapter 4 includes characterization of the metal complexes anchored on Eu_2O_3 nanoparticles. Qualitative and quantitative descriptions of how the metal complexes behave on Eu_2O_3 nanoparticles were made and compared with other metal oxides previously studied with similar complexes. More importantly, the nanoparticle-metal complex systems were characterized spectroscopically to determine if energy transfer occurs. Steady-state and time-resolved emission spectroscopy are primarily used to achieve that purpose.

Chapter 2 - Experimental Methods

2.1 Molecular Synthesis

Ruthenium(III) chloride hydrate (Alfa Aesar, Premion 99.99%), rhodium(III) chloride hydrate (Alfa Aesar, Premion 99.99%), iridium(III) chloride hydrate (Alfa Aesar, Premion 99.99%), 2,2'-bipyridine-4,4'-dicarboxylic acid (Strem), hydroquinone (Aldrich), lithium chloride (EM Science), potassium hexafluorophosphate (KPF_6, Fluka), spectral grade acetonitrile (Burdick and Jackson), ACS grade concentrated sulfuric acid (Fisher), HPLC grade solvents such as dichloromethane (Fisher), diethyl ether (Fisher), ethyl acetate (Fisher), methanol (Fisher) and ethanol (AAPER) were all used as received.

The ligand deeb[33] and the ruthenium complexes $[Ru(deeb)_2Cl_2]$[104] and $[Ru(deeb)_2dpp](PF_6)_2$[14] were prepared as previously reported.

cis-Dichlorobis(diethyl-2,2'-bipyridine-4,4'-dicarboxylate)rhodium(III) hexafluorophosphate, [Rh(deeb)$_2$Cl$_2$](PF$_6$). $[Rh(deeb)_2Cl_2](PF_6)$ synthesis was based on the synthesis of $[Rh(dpp)_2Br_2](PF_6)$.[105,106] The complex was prepared by heating to reflux 0.13 g (0.59 mmol) of $RhCl_3 \cdot xH_2O$ and 0.35 g (1.2 mmol) of deeb in 30 mL of 2:1 $EtOH/H_2O$ for 40 minutes. The solution was filtered hot and the filtrate was added to the KPF_6 solution prepared by diluting 20 mL of a saturated aqueous KPF_6 solution with 50 mL H_2O. The resulting pale yellow precipitate was separated from the solution by vacuum filtration, washed with several portions of diethyl ether, then redissolved in minimal dichloromethane and flash precipitated in diethyl ether with a yield of 78%.[107] δ (ppm), CD_2Cl_2: 10.06 (2H, d, J = 6 Hz), 9.05 (2H, s), 8.94 (2H, s), 8.48 (2H, d, J = 6 Hz), 8.02 (2H, d, J = 4 Hz), 7.84 (2H, d, J = 4 Hz), 4.61 (4H, q, $J_1 = J_2 = J_3 = 7$

Hz), 4.48 (4H, q, $J_1 = J_2 = J_3 = 7$ Hz), 1.53 (6H, t, $J_1 = J_2 = 7$ Hz), 1.41 (6H, t, $J_1 = J_2 = 7$ Hz). ESI mass spectrometry showed $[M - PF_6]^+ = 773$ (calculated 773).

cis-Dichlorobis(diethyl-2,2'-bipyridine-4,4'-dicarboxylate)iridium(III) hexafluorophosphate, [Ir(deeb)$_2$Cl$_2$](PF$_6$). The synthetic procedure for the iridium dichloride complex was patterned after its rhodium analog as discussed above. It was prepared by reacting 0.64 g (1.8 mmol) of $IrCl_3 \cdot xH_2O$ and 1.41 g (4.7 mmol) of deeb in 230 mL of 2:1 EtOH:H_2O, previously deoxygenated with argon for at least 15 minutes. The mixture was heated at reflux for 66 hours, filtered hot and the ethanol evaporated from the filtrate. The filtrate was then diluted with 10 mL H_2O and 30 mL of a saturated aqueous KPF_6 solution was added dropwise. The resulting precipitate was filtered, washed with cold water and diethyl ether and dried in vacuum. The solid was then dissolved in small amounts of acetone and flash precipitated in ether. Purification was done by recrystallizing twice in hot 4:1 methanol:ethyl acetate to isolate the bright yellow solid as product. Typical yield is ~33% (0.60 g, 0.59 mmol). ^{1}H NMR (400 MHz, $(CD_3)_2CO$): δ (ppm) 10.08 (d, 2H, $J = 6$ Hz), 9.45 (s, 2H), 9.34 (s, 2H), 8.62 (d, 2H, $J = 6$ Hz), 8.36 (d, 2H, $J = 6$ Hz), 7.90 (d, 2H, $J = 6$ Hz), 4.60 (q, 4H, $J_1 = J_2 = J_3 = 7$ Hz), 4.44 (q, 4H, $J_1 = J_2 = J_3 = 7$ Hz), 1.49 (t, 6H, $J_1 = J_2 = 7$ Hz), 1.35 (t, 6H, $J_1 = J_2 = 7$ Hz). ESI-MS (m/z): 863 found and calc. $[M\text{-}PF_6]^+$.

Bis(diethyl-2,2'-bipyridine-4,4'-dicarboxylate)-2,3-bis(2-pyridyl)pyrazineiridium(III) hexafluorophosphate, [Ir(deeb)$_2$dpp](PF$_6$)$_3$. The complex was prepared by reacting $[Ir(deeb)_2\text{-}Cl_2](PF_6)$ (0.11 g, 0.1 mmol) with 20 times excess of both dpp (0.49 g, 2 mmol) and $Tl(I)PF_6$ (0.76 g, 2 mmol) in 5 mL CH_3CN. The mixture was heated to reflux for 18 hours and cooled to room temperature. 50 mL of water was added, after which 10 mL of saturated aqueous KPF_6 was added dropwise. The off-white to light tan solids were recovered by vacuum filtration and

purified by elution through an LH-20 column with 3:1 CH_3CN:EtOH as solvent. The first fraction was collected, the solvent evaporated and the solids flash precipitated in diethyl ether using minimal amounts of acetonitrile. Yield was ~20% (0.29 g, 0.20 mmol). ^{1}H NMR (400 MHz, $(CD_3)_2CO$): δ (ppm) 9.57 (s, 1H), 9.54 (s, 3H), 8.90 (d, 1H, *J* = 3 Hz), 8.79 (d, 1H, *J* = 6 Hz), 8.71 (d, 1H, *J* = 4 Hz), 8.61 (d, 1H, *J* = 6 Hz), 8.55 (d, 1H, *J* = 6 Hz), 8.51 (d, 1H, *J* = 7 Hz), 8.48 (d, 1H, *J* = 6 Hz), 8.43 (d, 1H, *J* = 3 Hz), 8.33 (d, 1H, *J* = 5 Hz), 8.19 (m, 6H), 7.72 (m, 1H), 7.67 (d, 1H, *J* = 9 Hz), 4.49 (m, 8H), 1.37 (m, 12H). ESI-MS (m/z): 342 found and calc. $[M\text{-}3PF_6]^{3+}$.

2.2 Nanoparticle Synthesis

Nanoparticles were prepared by the inert gas-phase condensation method.[108] Approximately 1 g of metal oxide powder (Alfa Aesar, 99.99% REACTON) was sintered at 800°C for 4 hours and cold-pressed to produce ca. 13 mm diameter pellet which was then sintered overnight at 800-900°C. The pellet rested on a rotating platform in a stainless steel vacuum chamber maintained at 1-400 Torr N_2, with the pressure held constant depending on the size of nanoparticles desired. Vaporization was done with a cw-CO_2 laser beam (Synrad, Duo-Lase 30-40W) that was focused onto the target with a ZnSe lens (Figure 2.1). Nanoparticles were collected on a stainless steel sheet ~6 cm above the target. An average of 30 mg Eu_2O_3 and 15 mg Y_2O_3 nanoparticles can be obtained per hour of vaporization at 100 Torr N_2.

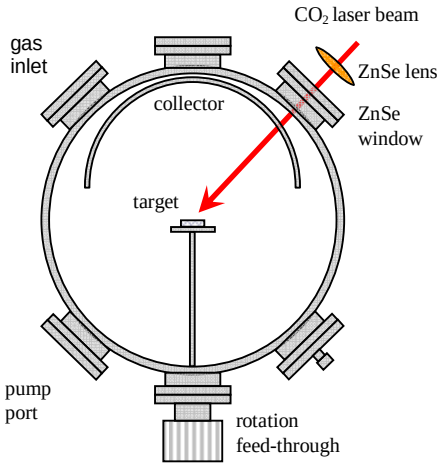

Figure 2.1. Schematic of the synthesis chamber for inert-gas condensation of nanoparticles.

2.3 ^{1}H NMR Spectroscopy

^{1}H NMR spectra were recorded at room temperature using a 400 MHz Spectrometer (Varian Inova). Sample solutions of the ligand and metal complexes were prepared by dissolving ~20 mg of compound in 0.5 mL of deuterated solvent that is sonicated and syringe-filtered prior to analysis.

2.4 Mass Spectrometry

Positive ion electrospray and fast-atom bombardment high-resolution mass spectral analysis of the ruthenium and rhodium complexes were performed by M-Scan Incorporated, West Chester, Pennsylvania, on a quadropole/time of flight mass spectrometer (Micromass Q-TOF API US hybrid) using acetonitrile/water/formic acid (50:50:1) as a matrix. ESI mass spectra of the iridium complexes were obtained using an LC-ESI-TOF spectrometer (Agilent) at the Analytical Services Laboratory, Department of Chemistry at Virginia Tech.

Electro-Spray Ionization mass spectra were obtained using an LC-ESI-TOF spectrometer (Agilent) at room temperature. Calculated mass spectra were obtained from the Scientific Instrument Services website (Sisweb.com).

2.5 Electronic Absorption Spectroscopy

Electronic absorption spectra in solution were recorded at room temperature using a diode-array spectrophotometer (Hewlett-Packard 8452A) with a 2-nm resolution. All measurements used Burdick and Jackson UV-grade acetonitrile or CH_2Cl_2 solvent in 1-cm quartz cuvettes.

2.6 Electron Microscopy

Nanoparticle diameters were estimated from SEM images at 200k magnification obtained from a Field Emission SEM (LEO 1550). Particle size distributions were constructed using Scion Image (Scion Corporation).

2.7 X-ray Powder Diffraction

Nanoparticle phase and size were determined using X-ray powder diffraction patterns obtained using a high resolution x-ray diffractometer (Rigaku RAPID Curved IP) with an image plate detector and Cu K_α radiation (1.54 nm) as source. Phase analysis was done using the Match! Software (Crystal Impact).

2.8 Preparation of Metal Complexes Anchored on Metal Oxides

Metal complexes were attached to metal oxide nanoparticles by literature methods for attachment of deeb complexes to TiO_2.[109] Metal oxide samples were vacuum-dried and shaken with 1-5 mM solutions of metal complex in acetonitrile or dichloromethane for ca. 24 hours. The stained oxides were collected by centrifugation (13000 rpm, 10 min), washed several times with solvent to remove unbound metal complex and vacuum-dried.

2.9 Reflection Spectroscopy

Reflection spectra were recorded from solid samples at room temperature using a deuterium tungsten halogen light source (Ocean Optics DH-2000), optical fiber bundle reflection probe (Ocean Optics R600-7-SR-125F), and a CCD array spectrophotometer (Ocean Optics USB2000). The probe was positioned at 90° and 3-5 mm from the powdered samples for all measurements. To obtain the spectra of as-prepared and complex-modified europium oxide and yttrium oxide nanoparticles, the samples were diluted by mixing with $BaSO_4$ (Alfa-Aesar) in ~1:4 ratio. The samples were then moistened with spectroscopic grade acetonitrile (Burdick and Jackson) prior to recording the spectra using moist $BaSO_4$ as reference.

2.10 ATR FT-IR Spectroscopy

Infrared spectra of solid samples at ambient conditions were recorded on an ATR FT-IR spectrometer (Midac M2004) with a diamond prism with air as reference. Infrared spectroscopy of plain Eu_2O_3 nanoparticles and Eu_2O_3 nanoparticles modified with $[Ir(deeb)_2Cl_2]^+$ under vacuum was performed as described in previous work.[11,16] Samples were mounted as 0.7-cm diameter spots on a tungsten mesh using a hydraulic press. The mesh was placed in a high vacuum stainless steel chamber with a base pressure of 10^{-6} Torr connected to a stainless steel back-chamber with a pressure of 5.4×10^{-8} mBar. Spectra were recorded using a Mattson Research Series I FTIR spectrometer contained in a vacuum cell with the samples positioned at 45° with respect to the spectrometer. Temperature control was done by ohmic heating using a K type thermocouple welded to the top of the mesh. Each spectrum is an average of 256 scans at 4 cm^{-1} resolution with the tungsten mesh as reference.

2.11 Quantitative Adsorption Studies

Solutions of $[Ru(deeb)_2dpp](PF_6)_2$ in acetonitrile (1 mL) at different concentrations were prepared and shaken with as-prepared and vacuum-dried europium oxide nanoparticles (15 mg) synthesized at 100 Torr for 24 hours. After reaction, the mixtures were centrifuged ($1x10^4$ rpm, 10 min) to separate the supernatant used for determining equilibrium concentrations c_{eq}, and the complex-modified particles. The solids were washed with several portions of acetonitrile, vacuum-dried and then reacted with 1×10^{-3} M NaOH in 1:1 $CH_3CN:H_2O$ to desorb the metal complexes from the nanoparticles. After centrifugation of this mixture the supernatant is used to determine to the concentration of adsorbed metal complexes, Γ. Actual concentrations of all metal complex solutions were determined from absorbance measurements and using the molar absorptivity of the complex at 464 nm.

2.12 Energy Dispersive X-ray (EDX) Analysis

Energy Dispersive X-ray (EDX) analysis was performed using a scanning electron microscope (ISI-SX-40) set at 20.0 keV with an X-ray detector (Thermo Electron Corp. 5515E-ISUS-SN) and an interface controller (IXRF Systems Inc. Model 500). Eu_2O_3 nanoparticles modified with $[Ir(deeb)_2Cl_2](PF_6)$ and $[Ir(deeb)_2(dpp)](PF_6)_3$ were dispersed with hexanes on aluminum mounts and allowed to dry. Samples of Y_2O_3 nanoparticles modified with $[Ir(deeb)_2Cl_2](PF_6)$ and $[Ir(deeb)_2(dpp)](PF_6)_3$ were thickly pressed on carbon tape to ensure full coverage.

2.13 Emission Spectroscopy

Emission spectra were recorded from solid and solution samples at room temperature and 77 K using a Quantamaster spectrofluorometer (Photon Technologies International QM-40). The

system contains a high intensity continuous xenon excitation source and a red-sensitive photomultiplier tube collecting at a right angle and operating in photon counting mode with 4-nm resolution. For solid room temperature measurements, samples were packed on a black fiberglass block with a 3 mm diameter and 2 mm deep depression. Measurements of solutions at room temperature were carried out in 1-cm path length cuvettes. At 77 K, solid samples were packed to a 3 mm height at the bottom of quartz NMR tubes and cooled in a finger dewar with liquid nitrogen. Glass samples were prepared in NMR tubes by dissolving compounds in a 4:1 ethanol:methanol matrix, sonicating the solutions and placing the tubes in a finger dewar cooled with liquid nitrogen. Emission spectra were shifted to a common baseline. Emission spectra were corrected for PMT response and normalized. Excitation spectra of solids were corrected for PMT response after subtraction of background scattering using solid Y_2O_3 nanoparticles.

2.14 Lifetime Measurements

Lifetimes were measured using a pulsed nitrogen-pumped dye laser (Photon Technologies International) as excitation source. Direct excitation from the laser was done for 337 nm excitation while dyes PBBO and Coumarin-460 (Exciton) were used to excite at 395 nm and 460 nm, respectively. The laser beam was focused at a 45° angle to the sample using a 60-mm focal length lens. Sample preparation is the same as used for emission measurements. Emission was collected through a 75-mm lens focused through a cut-off or bandpass filter onto a photomultiplier tube (Photon Technologies International R928) and recorded by averaging 300 or more laser pulses using a 300 MHz oscilloscope (LeCroy 9361). Lifetime values were approximated by exponential curve fitting using Origin (OriginLab Corp.) after subtracting a reference signal due to laser scatter from the sample holder.

2.15 Electrochemistry

Cyclic voltammograms were recorded using a potentiostat (Bioanalytical Systems) with a platinum wire auxiliary electrode, a 1.9 mm diameter glassy carbon disk working electrode and a Ag/AgCl reference electrode (0.29 V vs. NHE). Metal complex solutions were prepared using 0.1 M tetrabutylammonium hydroxide in Burdick and Jackson UV grade acetonitrile as supporting electrolyte.

Chapter 3 - Characterization of Ruthenium, Rhodium and Iridium Complexes and Europium Oxide Nanoparticles

3.1 Characterization of Metal Complexes

3.1.1 Ruthenium Complexes

The ruthenium complexes used in this work were synthesized to compare properties of these complexes on Eu_2O_3 nanoparticles with those on other known metal oxide surfaces. Characterization of $[Ru(deeb)_2Cl_2]$ was done using ^1H NMR spectroscopy. The structures and 1D NMR spectra of the ruthenium complex and the deeb ligand are shown in Figure 3.1 A-C. Chemical shift assignments for solvent and residual water were based on a published collection of values.[110] The presence of methyl (t, 12H) and methylene (q, 8H) protons in $[Ru(deeb)_2Cl_2]$ at 1.40 and 4.47 ppm, respectively, indicate retention of the ester moieties of the deeb ligand upon formation of the complex. COSY and NOESY 2D NMR spectra of the complex in $CDCl_3$ at the aromatic region are shown in Figure 3.1 D-E. The chemical shift at 8.18 ppm is assigned to be due to the proton in the 5 position of the bipyridine unit because of its correlation with the most downfield proton in the 6 position while those at 7.71 and 7.50 ppm are assigned to be due to the 5′ and 6′ protons because of their correlation with each other as seen in the COSY spectra.

$[Ru(deeb)_2Cl_2]$ was used as starting material for synthesizing $[Ru(deeb)_2dpp](PF_6)_2$ according to literature procedures.[111] The dpp complex was characterized using mass spectrometry, electronic absorption spectroscopy and electrochemistry. The mass spectrum (FAB-MS) of $[Ru(deeb)_2dpp](PF_6)_2$ show peaks at 1081 and 936 m/z consistent with the $(M-PF_6)^+$ and $(M-2PF_6)^{2+}$ ions, respectively. The electronic absorption spectrum of the complex in acetonitrile as shown in Figure 3.2A displays $^1\pi\rightarrow\pi^*$ ligand transitions in the UV region and

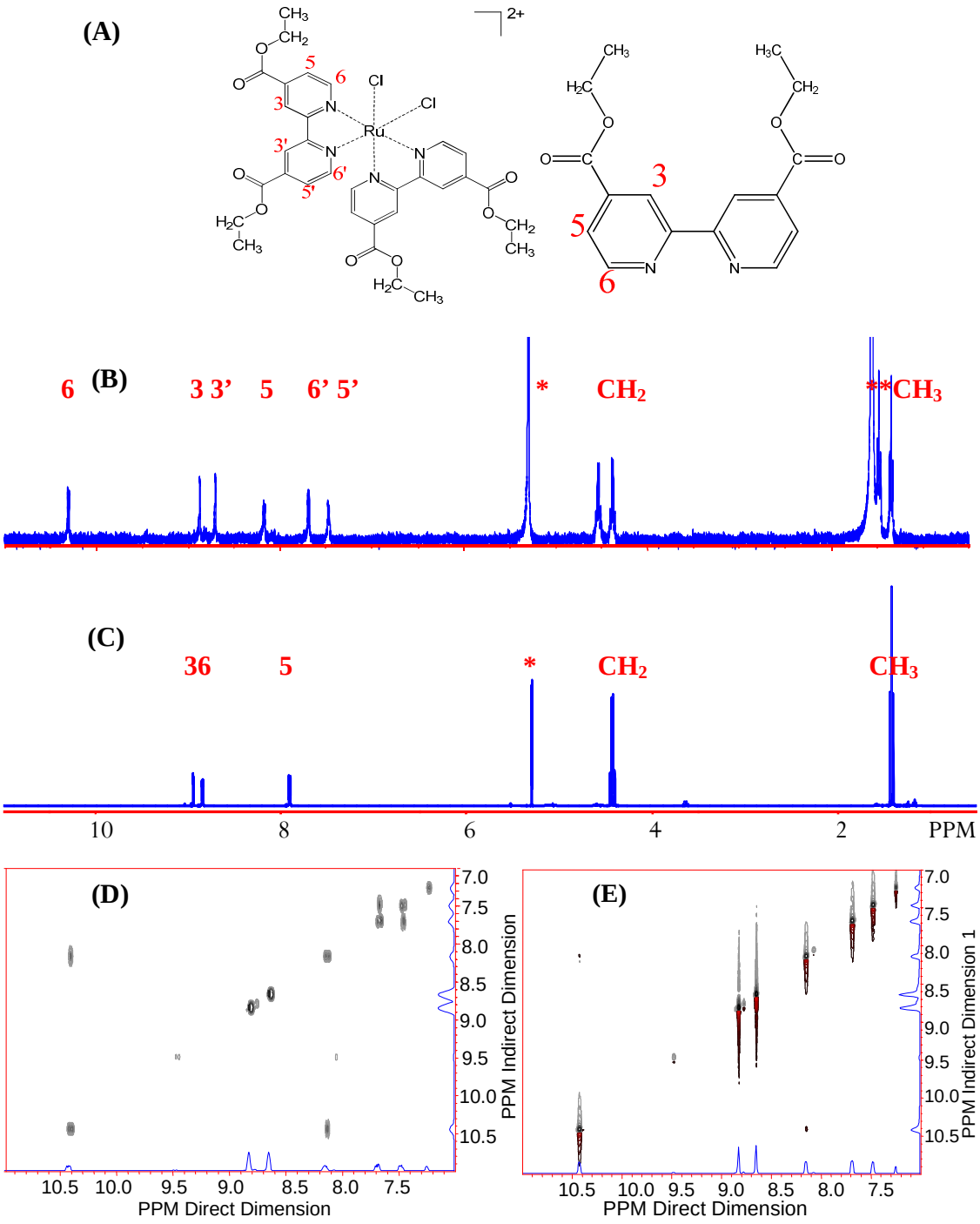

Figure 3.1. (A) Structures and chemical shift assignments of $[Ru(deeb)_2Cl_2]$ and deeb, where deeb = diethyl-2,2'-bipyridine-4,4'-dicarboxylate; 1D ^1H NMR of (B) $[Ru(deeb)_2Cl_2]$ and (C) deeb in CD_2Cl_2 (* and ** indicate solvent peak and water, respectively); aromatic region of (D) COSY and (E) NOESY ^1H NMR spectra of $[Ru(deeb)_2Cl_2]$ in $CDCl_3$.

^{1}MLCT transitions (Ru(dπ)→dpp(π*) at 464 nm and Ru(dπ)→deeb(π*) at 432 nm) in the visible region. The molar absorptivity of the complex at 464 nm (2.12 x 10^4 M^{-1} cm^{-1}) is consistent with that reported by Meyer *et al.*[105] The cyclic voltammogram of $[Ru(deeb)_2dpp](PF_6)_2$ in 0.1 M TBAH in acetonitrile as shown in Figure 3.2B displays a $Ru^{2+/3+}$ oxidative couple at 1.63 V and 3 ligand reductive couples at -0.87 V, -1.17 V and -1.30 V, which is also consistent with the formation of the complex.

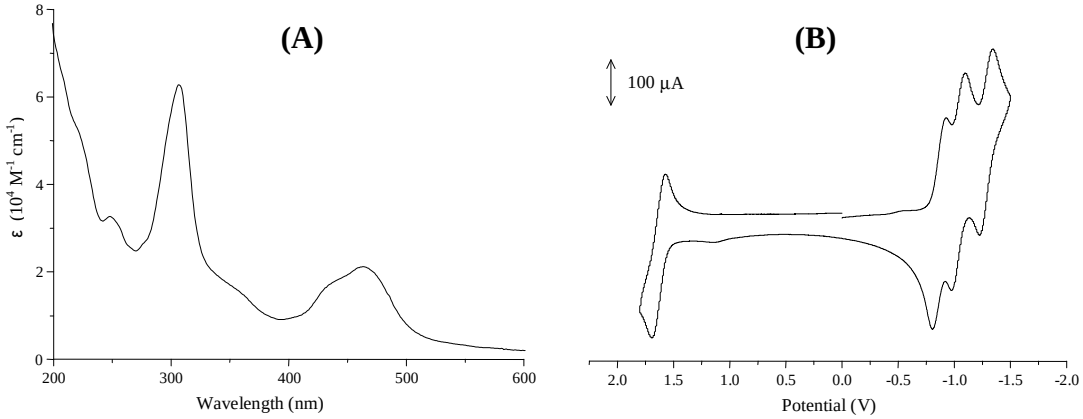

Figure 3.2. (A) Electronic absorption spectrum and (B) cyclic voltammogram of $[Ru(deeb)_2dpp](PF_6)_2$ at room temperature in CH_3CN (deeb = diethyl-2,2'-bipyridine-4,4'-dicarboxylate, dpp = 2,3-bis(2-pyridyl)pyrazine).

3.1.2 Rhodium Complex

The rhodium complex $[Rh(deeb)_2Cl_2](PF_6)$ was characterized by ^{1}H NMR spectroscopy (Figure 3.3). The chemical shifts in the 1D spectrum of this new complex shown in Figure 3.3B are the following: δ (ppm), CD_2Cl_2: 10.06 (2H, d, J = 6 Hz), 9.05 (2H, s), 8.94 (2H, s), 8.48 (2H, d, J = 6 Hz), 8.02 (2H, d, J = 4 Hz), 7.84 (2H, d, J = 4 Hz), 4.61 (4H, q, $J_1 = J_2 = J_3$ = 7 Hz), 4.48 (4H, q, $J_1 = J_2 = J_3$ = 7 Hz), 1.53 (6H, t, $J_1 = J_2$ = 7 Hz), 1.41 (6H, t, $J_1 = J_2$ = 7 Hz). The distribution of protons in the 1D and 2D COSY and NOESY (Figure 3.3C-D) ^{1}H NMR spectra of the rhodium complex is similar to that in the ruthenium analog, which suggests a similar assignment of protons and the formation of the complex. The rhodium compound was also

analyzed with ESI mass spectrometry and gave a fragmentation pattern consistent with the proposed molecular structure: ESI-MS m/z: 773 $(M\text{-}PF_6)^+$, calculated 773 (Figure 3.4).

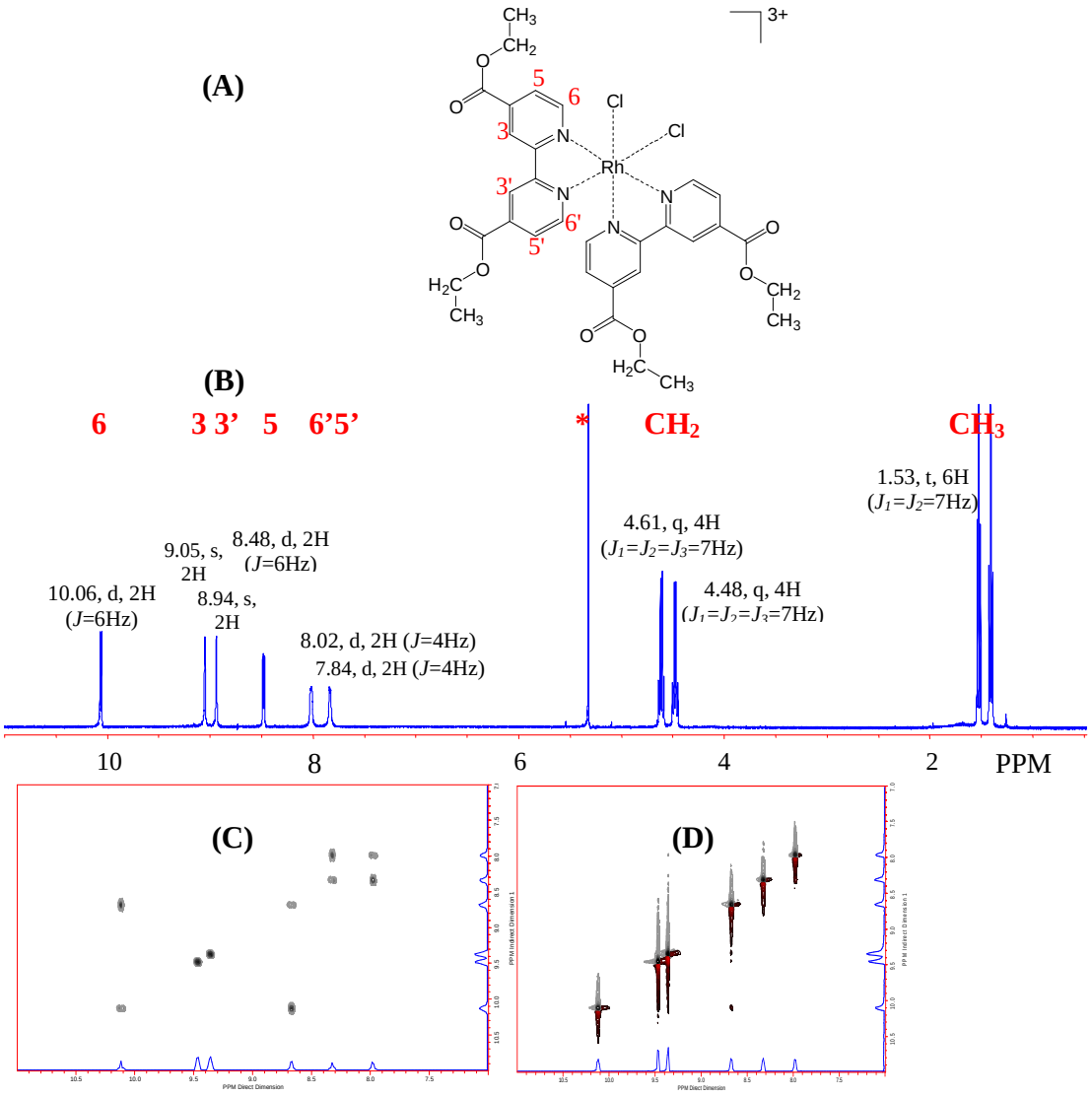

Figure 3.3. (A) Structure and chemical shift assignment of $[Rh(deeb)_2Cl_2](PF_6)$, where deeb = diethyl-2,2'-bipyridine-4,4'-dicarboxylate; (B) 1D ^1H NMR of $[Rh(deeb)_2Cl_2](PF_6)$ in CD_2Cl_2 (* indicates solvent peak); aromatic region of (D) COSY and (E) NOESY ^1H NMR spectra of $[Rh(deeb)_2Cl_2](PF_6)$ in CD_2Cl_2.

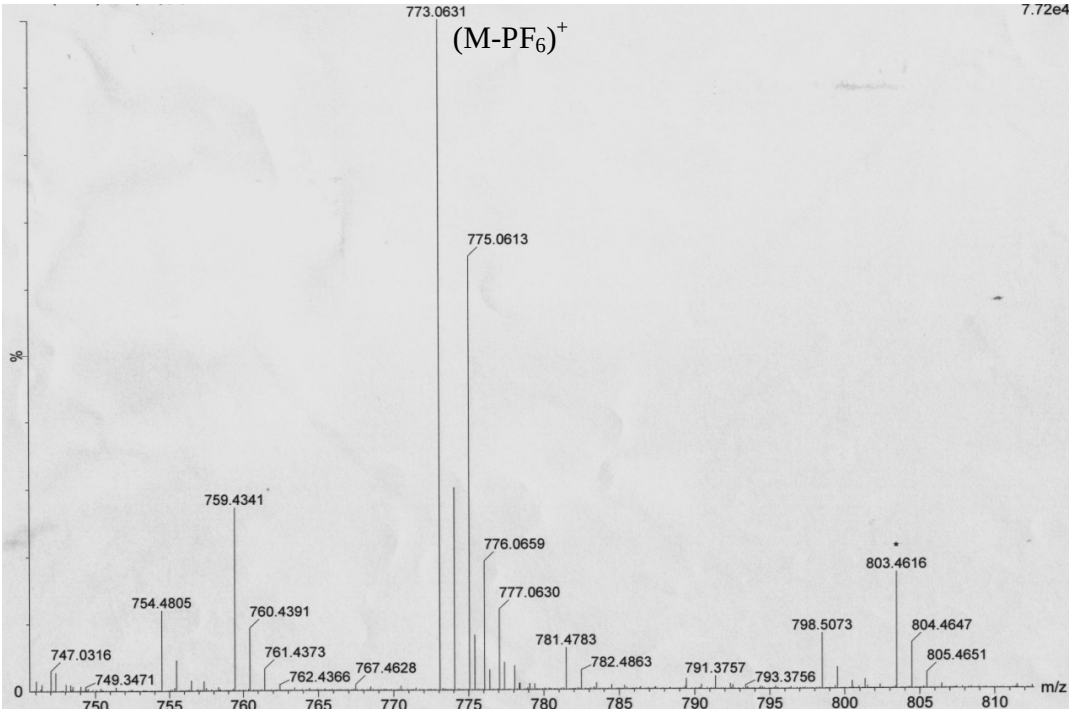

Figure 3.4. Mass Spectrum of $[Rh(deeb)_2Cl_2](PF_6)$.

Electronic absorption spectra of $[Rh(deeb)_2Cl_2](PF_6)$, deeb and their bpy analogs (Figure 3.5A) show a maximum at 328 nm ($\varepsilon = 2.60 \times 10^4\ M^{-1}\ cm^{-1}$) which is assigned to be deeb $^1\pi\rightarrow\pi^*$ transition. Compared to that of the bpy complex, this peak is slightly red-shifted due to the electron-withdrawing effect of the ester group that lowers the energy of the π^* orbital of deeb.[105] No emission was observed at RT due to fast nonradiative decay. Emission from the ^{3}LF state of $[Rh(deeb)_2Cl_2](PF_6)$ is evident at 680 nm and 704 nm for the solid and glassy solutions at 77 K, respectively (Figure 3.4B). The presence of this emissive state was crucial in choosing the rhodium dichloride complex for attaching on Eu_2O_3 because it lies close and slightly lower in energy relative to the $^5D_0$ state of Eu_2O_3 as shown in Figure 3.6. This state along with the ^{1}IL state at 328 nm, which lies close and slightly lower in energy relative to the Eu-O charge transfer state, make $[Rh(deeb)_2Cl_2](PF_6)$ ideal for investigating energy transfer from the nanoparticles to the complex.

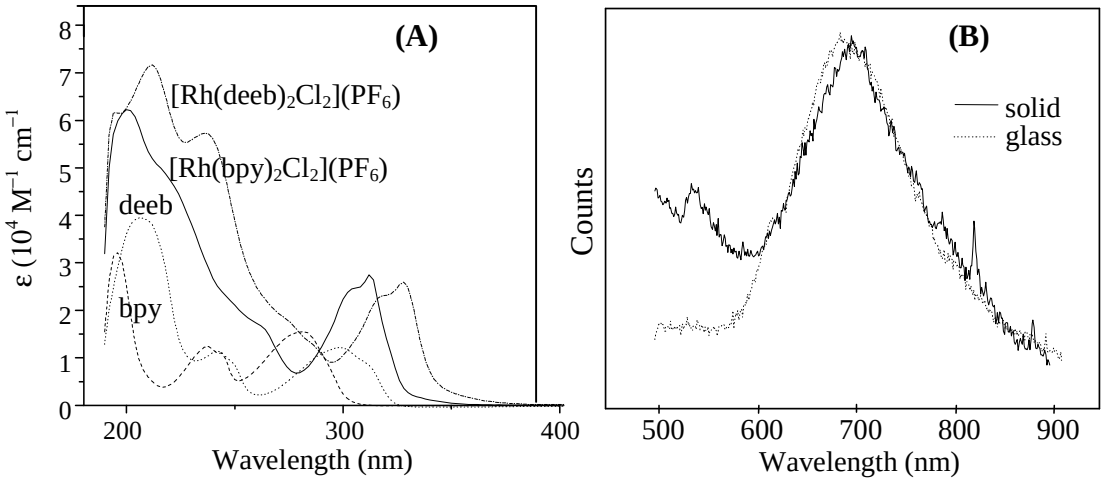

Figure 3.5. (A) Electronic absorption spectra of bpy (------), deeb (·····), $[Rh(bpy)_2Cl_2](PF_6)$ (——) and $[Rh(deeb)_2Cl_2](PF_6)$ (-·-·-·-) at room temperature in CH_3CN (deeb = diethyl-2,2'-bipyridine-4,4'-dicarboxylate; bpy = 2,2'-bipyridine); (B) Emission spectra at 77 K of $[Rh(deeb)_2Cl_2](PF_6)$ solid (solid line) and in 4:1 MeOH:EtOH glass (dotted line).

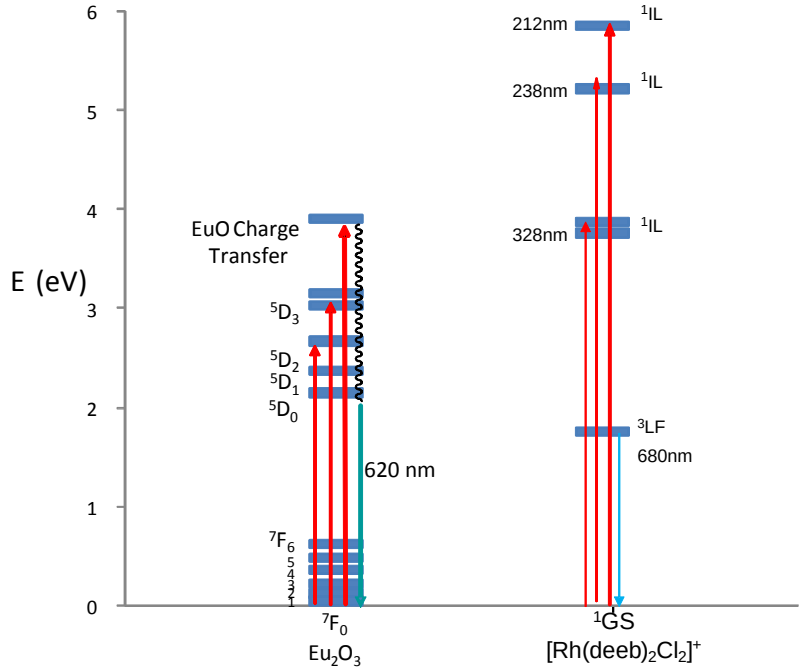

Figure 3.6. Energy diagram for Eu_2O_3 and $[Rh(deeb)_2Cl_2](PF_6)$, where deeb = diethyl-2,2'-bipyridine-4,4'-dicarboxylate.

3.1.3 Iridium complexes

The iridium complexes were prepared to investigate the possibility of energy transfer from the complexes to Eu_2O_3. $[Ir(deeb)_2Cl_2](PF_6)$ serves as a starting point for synthetic and photophysical experiments. $[Ir(deeb)_2(dpp)](PF_6)_3$ was synthesized because the chloride ligands in the first complex are expected to be labile enough to allow the iridium center to coordinate with oxygen atoms on the metal oxide surface. Replacing the chloride ligands with the dpp ligand will allow a more uniform mode of attachment of the complexes on the oxide surface as well as a bridging ligand for adding more metal complex structures on the nanoparticles.

$[Ir(deeb)_2Cl_2](PF_6)$ was synthesized using a similar procedure for its rhodium analog and Figure 3.7 shows the ^1H NMR spectral data for the newly prepared $[Ir(deeb)_2Cl_2](PF_6)$. Chemical shift assignments for solvent and residual water were based on a published collection of values.[112] The presence of methyl protons at 1.49 ppm (t, 6H) and 1.35 ppm (t, 6H), and methylene protons at 4.60 ppm (q, 4H) and 4.44 ppm (q, 4H) in $[Ir(deeb)_2Cl_2](PF_6)$ indicate retention of the ester moieties of the deeb ligand upon formation of the complex. ^1H-^1H COSY NMR spectrum of the complex at the aromatic region is shown in Figure 1C. The chemical shift at 8.62 ppm is assigned to the proton in the 5 position of the bipyridine unit because of its correlation with the most downfield proton in the 6 position. The peaks at 7.90 and 8.36 ppm are assigned to the 5′ and 6′ protons because of their correlation with each other as seen in the ^1H-^1H COSY spectra. These assignments are made to correct previous assignments for the ruthenium and rhodium analogs.[111] The 1-D and 2-D spectra show multiplets and integration that are consistent with those reported for $[Ir(bpy)_2Cl_2](PF_6)$ sans the 4 and 4′ protons.[112,113] The ESI-MS spectrum in Figure 2A is consistent with the $(M\text{-}PF_6)^+$ ion (863, found and calc.).

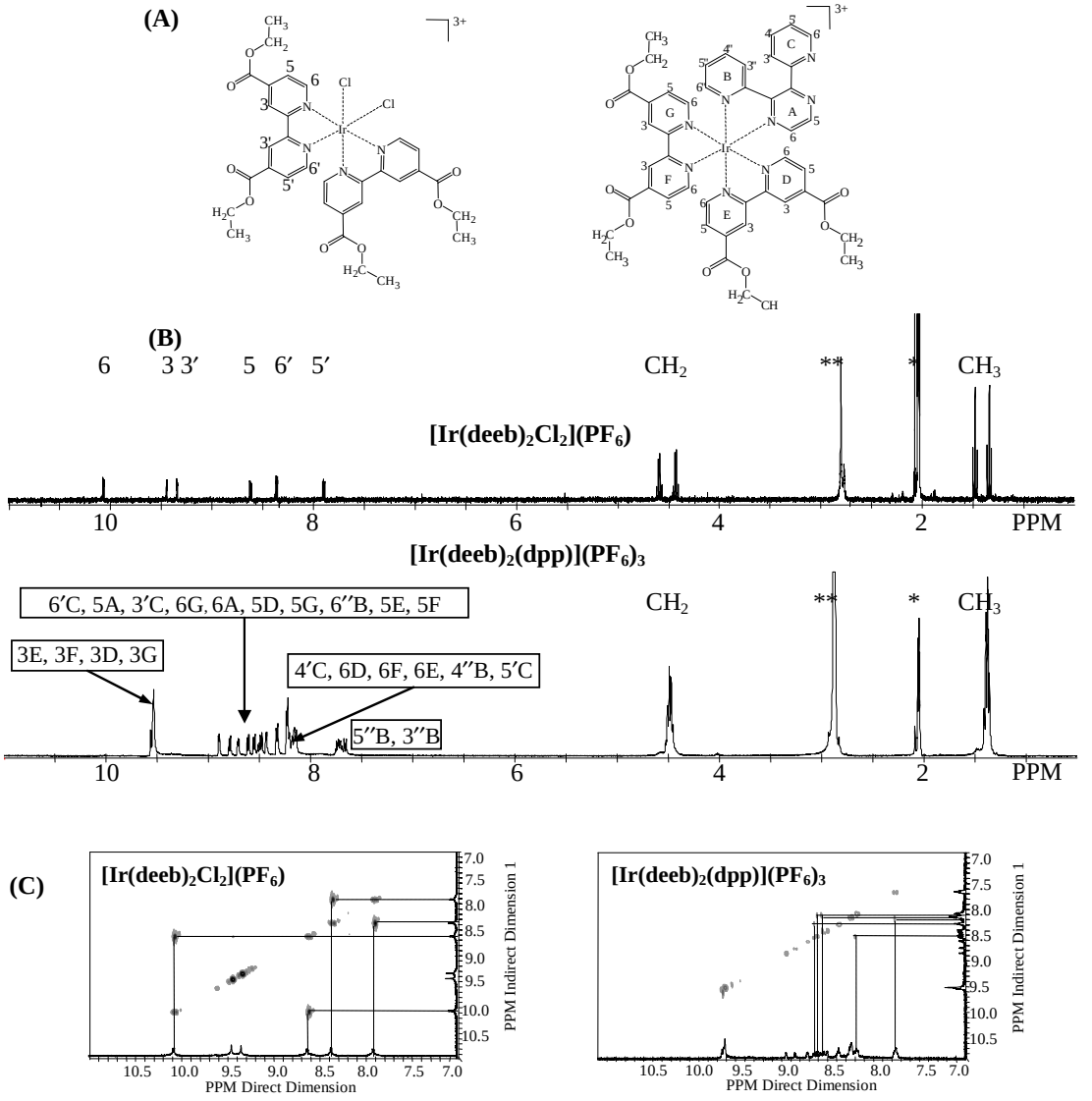

Figure 3.7. (A) Structures and chemical shift assignments, (B) 1D ^{1}H NMR spectra and (C) ^{1}H-^{1}H COSY NMR spectra of aromatic regions of $[Ir(deeb)_2Cl_2](PF_6)$ and $[Ir(deeb)_2(dpp)](PF_6)_3$ in $(CD_3)_2CO$, where deeb = diethyl-2,2'-bipyridine-4,4'-dicarboxylate, dpp = 2,3-bis(2-pyridyl)pyrazine (* and ** indicate solvent and water, respectively).

The ^{1}H NMR spectrum and assignments of $[Ir(deeb)_2(dpp)](PF_6)_3$, which are consistent with those of $[Ru(deeb)_2(dpp)](PF_6)_3$,[114] are also shown in Figure 3.7. The ESI-MS spectrum in Figure 3.8 displays a fragmentation pattern for $(M\text{-}3PF_6)^{3+}$ (342, found and calc.).

$[Ir(deeb)_2Cl_2](PF_6)$ **$[Ir(deeb)_2(dpp)](PF_6)_3$**

Experimental

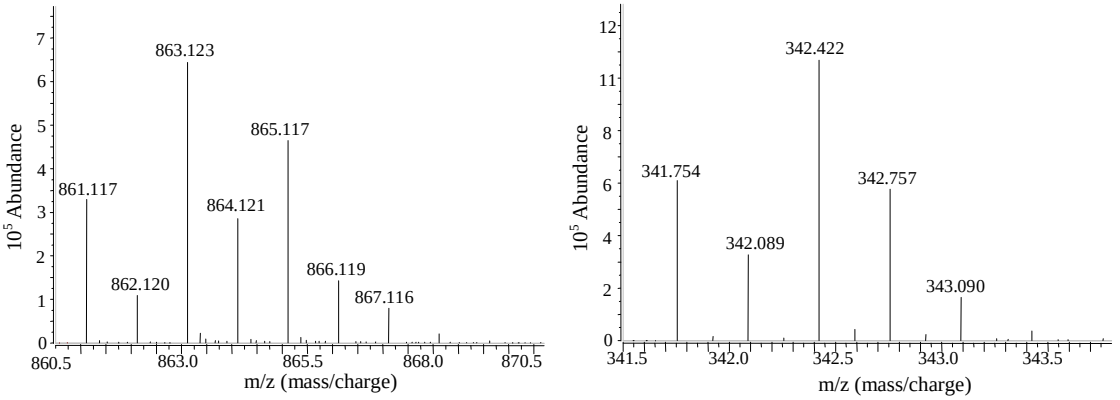

Theoretical

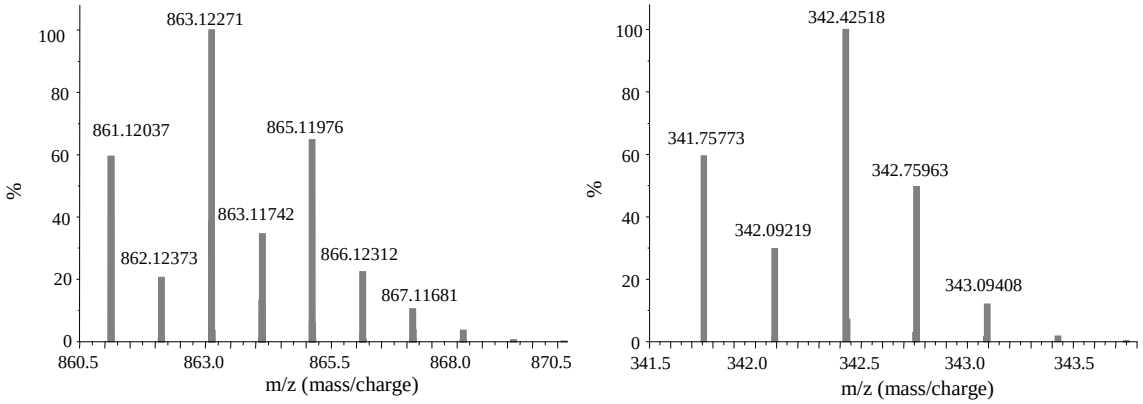

Figure 3.8. Experimental and theoretical mass spectral data for $[Ir(deeb)_2Cl_2](PF_6)$ and $[Ir(deeb)_2(dpp)](PF_6)_3$, where deeb = diethyl-2,2'-bipyridine-4,4'-dicarboxylate, dpp = 2,3-bis(2-pyridyl)pyrazine.

Table 3.1 and Figure 3.9 give electrochemical data for $[Ir(deeb)_2Cl_2](PF_6)$ with those for analogous compounds $[Ir(bpy)_2Cl_2](PF_6)$ and $[Ir(dpp)_2Cl_2](PF_6)$ previously reported by our group.[115] Two reversible reductive couples at -0.72 V and -0.87 V, which are assigned to be deeb ligand reductions, followed by a two-electron, quasi-reversible iridium reduction at -1.48 V were observed for $[Ir(deeb)_2Cl_2](PF_6)$, consistent with previous reports on the bpy and dpp analogs. The shoulder at -1.07 V may be attributed to reduction of a $[Ir(deeb)_2Cl]^+$ species,

which could have formed from reducing the starting material and could clearly be defined at lower scan rates.[46]

Table 3.1. Electrochemical data for $[Ir(deeb)_2Cl_2](PF_6)$, $[Ir(bpy)_2Cl_2](PF_6)$,[46,116,117] $[Ir(dpp)_2Cl_2](PF_6)$[46] and $[Ir(deeb)_2(dpp)](PF_6)_3$ using 0.1 M TBAH in CH_3CN as supporting electrolyte at room temperature.

Complex	E_p^a (V)	E_p^c (V)	$E_{1/2}$ (V)	Assignment
$[Ir(deeb)_2Cl_2](PF_6)$	-0.67	-0.78	-0.72	$deeb^{0/-}$
	-0.87	-0.93	-0.87	$deeb^{0/-}$
		-1.48		$Ir^{3+/+}$
$[Ir(bpy)_2Cl_2](PF_6)$	-1.10	-1.25	-1.18	$bpy^{0/-}$
	-1.30	-1.47	-1.39	$bpy^{0/-}$
		-2.12		$Ir^{3+/+}$
$[Ir(dpp)_2Cl_2](PF_6)$	-0.80	-0.86	-0.83	$dpp^{0/-}$
	-1.03	-1.09	-1.06	$dpp^{0/-}$
		-1.79		$Ir^{3+/+}$
$[Ir(deeb)_2(dpp)](PF_6)_3$	-0.34	-0.42	-0.38	$deeb^{0/-}$
	-0.49	-0.58	-0.54	$deeb^{0/-}$
	-0.67	-0.76	-0.71	$dpp^{0/-}$
		-1.33		$Ir^{3+/+}$

Less negative reduction values for deeb compared to bpy and dpp as seen in the electrochemical data for the dichloride complexes imply that the deeb ligand is easier to reduce than the other two ligands. Hence, the first three reductions for $[Ir(deeb)_2(dpp)](PF_6)_3$ at -0.38 V, -0.54 V and -0.71 V are assigned to be $deeb^{0/-}$, $deeb^{0/-}$ and $dpp^{0/-}$ reductions, respectively. Differences in the deeb reduction potentials for $[Ir(deeb)_2Cl_2](PF_6)$ and $[Ir(deeb)_2(dpp)](PF_6)_3$ could be due to the differences in the nature of their excited states which modulate their abilities for electron transfer. In addition, the chloride ligands in $[Ir(deeb)_2Cl_2](PF_6)$ are strongly electron-donating

ligands which destabilize the iridium metal orbitals making it easier to be reduced in $[Ir(deeb)_2Cl_2](PF_6)$. A shoulder similar to that in $[Ir(deeb)_2Cl_2](PF_6)$ occurs at -0.78 V, which could be attributed to one part of the deeb ligand detaching from the metal ion to form a $[Ir(deeb)_2(dpp)]^{2+}$ species. Another shoulder at -1.49 V appears for $[Ir(deeb)_2(dpp)](PF_6)_3$, a reductive couple similarly observed for trischelated iridium complexes like $[Ir(bpy)_3]^{3+}$ and could be assigned as reduction of a $[Ir(deeb)_2(dpp)]^{1-}$ species.[46]

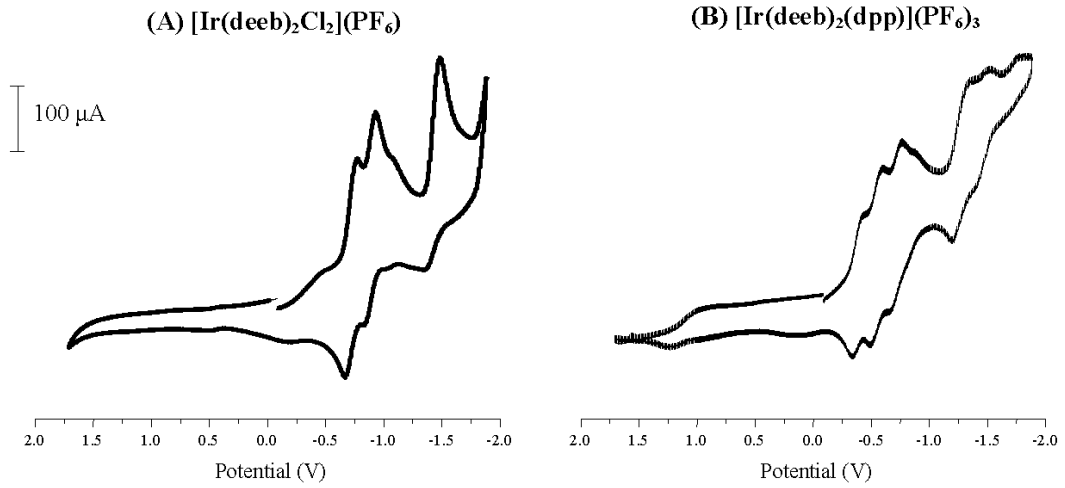

Figure 3.9. Cyclic voltammograms of (A) $[Ir(deeb)_2Cl_2](PF_6)$ and (B) $[Ir(deeb)_2(dpp)](PF_6)_3$ using 0.1 M TBAH in CH_3CN as supporting electrolyte at room temperature (deeb = diethyl-2,2'-bipyridine-4,4'-dicarboxylate, dpp = 2,3-bis(2-pyridyl)pyrazine).

The electronic absorption spectrum of $[Ir(deeb)_2Cl_2](PF_6)$ (Figure 3.10A) displays a deeb transition at 308 nm and a small peak at 402 nm assigned to be a ^{1}MLCT, Ir(dπ)→deeb(π*), transition. Table 3.2 compares the spectral properties of $[Ir(deeb)_2Cl_2](PF_6)$ with its bpy analog.[105] The absorption maxima are slightly red-shifted due to the electron-withdrawing effect of the ester group, which lowers the deeb π* orbital. Excited iridium complexes form metal-to-ligand charge transfer (MLCT) or internal ligand (IL) emissive excited states, depending on the electron density around the metal. If the ligands are anionic, in the case of halide or cyclometallating ligands, the emissive state tends to be a MLCT state because there is sufficient

charge density on the metal; otherwise, emission is due to an IL excited state.[46] The $[Ir(bpy)_2Cl_2](PF_6)$ complex for instance has an emissive ^{3}MLCT state at 510 nm.[33,39] Emission spectra of $[Ir(deeb)_2Cl_2](PF_6)$ in Figure 3.11A reveal a broad peak with a maximum at 538 nm and a tail that extends beyond 700 nm. The complex in powder form shows a similar spectrum that is red-shifted with a peak at 567 nm. Other iridium complexes used for organic light-emitting diodes (OLEDs) and light-emitting electrochemical cells (LECs) show similar shifts.[46] As shown in Figure 3.12A, the room-temperature excited-state lifetime of $[Ir(deeb)_2Cl_2](PF_6)$ in acetonitrile is 1.71 ± 0.17 μs, which is longer compared to those of similar compounds in DMF at room temperature: $[Ir(bpy)_2Cl_2]^+$, 0.333 μs; $[Ir(phen)_2Cl_2]^+$, 0.324 μs; and $[Ir(5,6\text{-}Mephen)_2Cl_2]^+$, 0.840 μs.[118,119] A high quantum yield of emission for $[Ir(deeb)_2Cl_2](PF_6)$ (Φ = 0.33) was also observed. For $[Ir(bpy)_2Cl_2]^+$, the quantum yield is 0.0066 in acetonitrile at room temperature.[116,120] Both a lower nonradiative rate and a higher radiative rate for $[Ir(deeb)_2Cl_2](PF_6)$ compared to the other compounds lead to a higher quantum yield. The lifetime for the solid at room temperature displays a single exponential decay profile giving τ = 0.35 ± 0.02 μs. Reduction of the lifetime in the solid state may be attributed to concentration quenching or energy transfer to quenching defects.

Figure 3.10B shows the electronic absorption and emission spectra of $[Ir(deeb)_2(dpp)](PF_6)_3$. The absorption spectrum contains peaks in the UV region that are similar to those in the spectrum of $[Ir(bpy)_3]^{3+}$ which were assigned as $^1\pi\rightarrow\pi^*$ transitions from the ligands.[117] The emission spectrum at room temperature contains a broad band centered at 540 nm, which is red shifted to 599 nm in the solid state. Luminescence is assigned to be relaxation of the $^3\pi\rightarrow\pi^*$ excited state, as in $[Ir(bpy)_3]^{3+}$ which provides for a lower energy excited state that is closer to the Eu^{3+} $^5D_0$ state.[121] The assignment of the emissive state of $[Ir(deeb)_2(dpp)](PF_6)_3$

was patterned after $[Ir(bpy)_3]^{3+}$ and other tris-chelated iridium compounds which were found to be primarily $^3\pi\rightarrow\pi^*$ in nature with some ^{3}MLCT character according to the work of Demas *et. al*[121] and those included in the review of Flamigni *et. al*[115,121]. The electron-donating chloride ligands destabilize the Ir orbitals providing for the MLCT nature of the lowest lying state. The decay curve of $[Ir(deeb)_2(dpp)](PF_6)_3$ is shown in Figure 4B and the lifetime was found to be 1.23 ± 0.03 μs and 0.14 ± 0.02 μs in acetonitrile solution and in the solid state, respectively, which is comparable to that of $[Ir(bpy)_3]^{3+}$ (2.4 μs in methanol [33]) at room temperature.

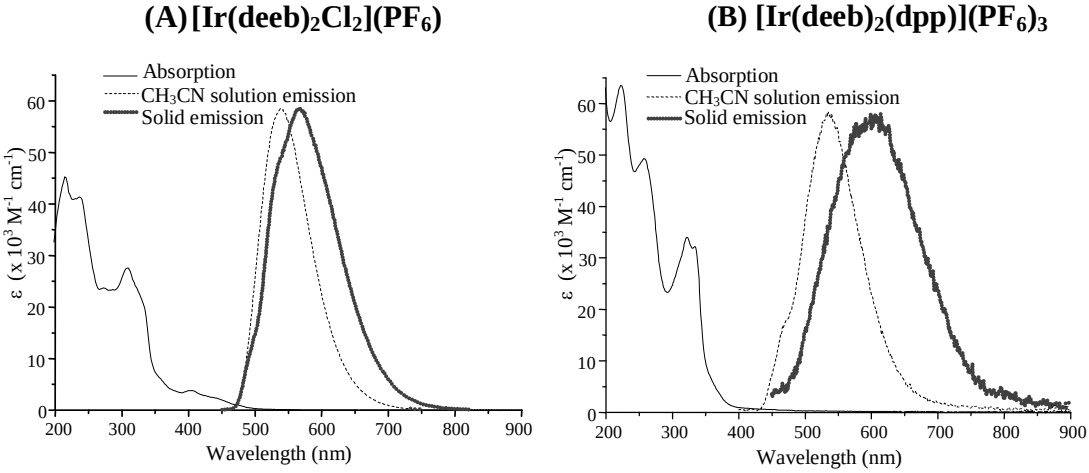

Figure 3.10. Electronic absorption and normalized emission spectra at room temperature of (A) $[Ir(deeb)_2Cl_2](PF_6)$ and (B) $[Ir(deeb)_2(dpp)](PF_6)_3$ in CH_3CN and as solid (deeb = diethyl-2,2'-bipyridine-4,4'-dicarboxylate, dpp = 2,3-bis(2-pyridyl)pyrazine). For the emission spectra, a 340-nm bandpass filter and a 500 nm cut-off filter are used in the excitation and emission monochromators, respectively.

$[Ir(deeb)_2Cl_2](PF_6)$ was used in this work because it has the ^{3}MLCT state that lies slightly higher in energy compared to the $^5D_0$ state of Eu_2O_3, as shown in the energy diagram below (Figure 3.12). Interestingly, one of the ^{1}IL states of the iridium complex is also slightly higher in energy compared to the Eu-O charge transfer band. It is noted that the $[Ir(deeb)_2(dpp)](PF_6)_3$ ^{1}IL excited state lies also at a slightly higher energy compared to the $^5D_0$ state of Eu_2O_3 (Figure 3.11)

as in $[Ir(deeb)_2Cl_2](PF_6)$, which makes studies in comparing energy transfer using these two iridium complexes interesting.

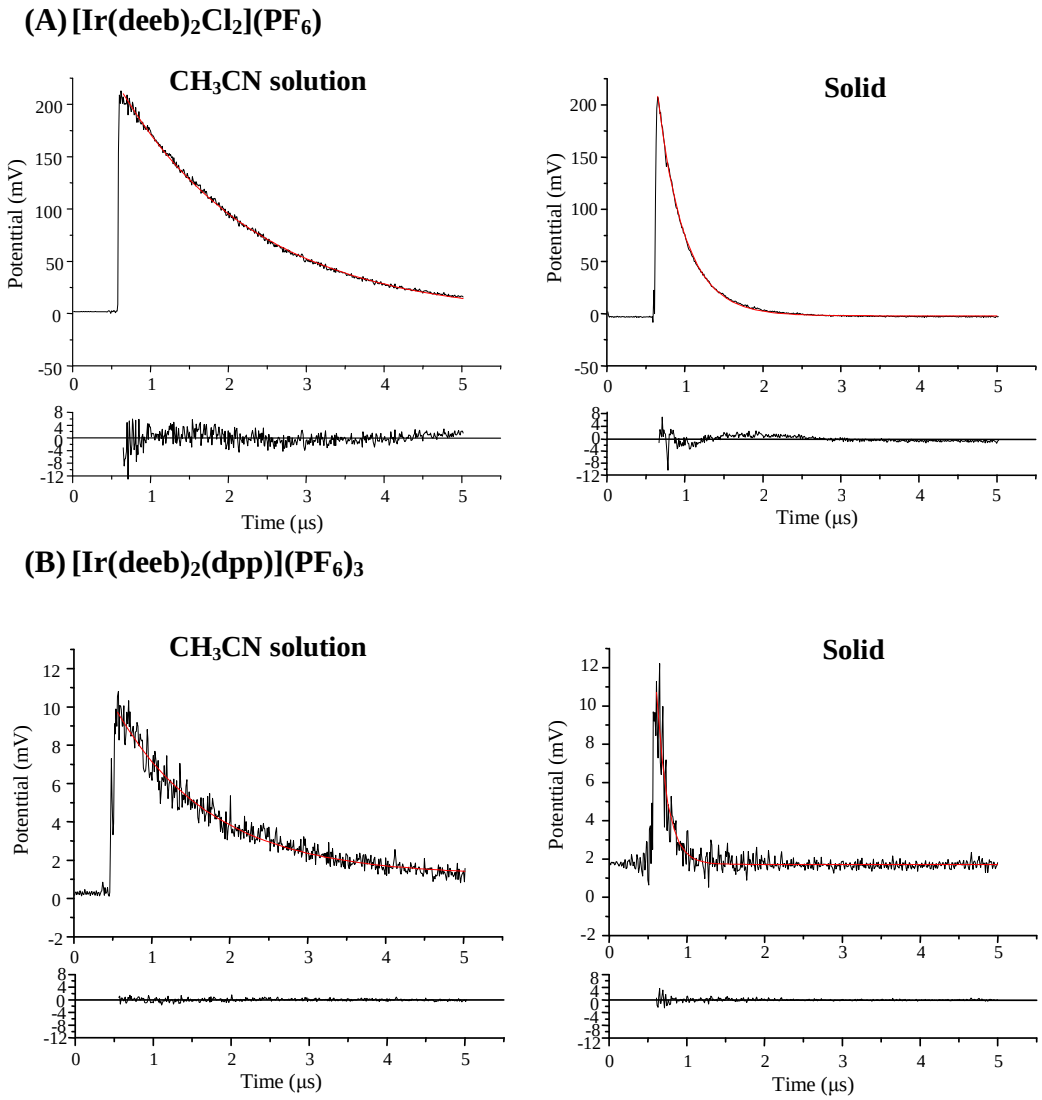

Figure 3.11. Lifetime decay curves and residual plots of (A) $[Ir(deeb)_2Cl_2](PF_6)$ and (B) $[Ir(deeb)_2(dpp)](PF_6)_3$ in CH_3CN and as solid at room temperature (deeb = diethyl-2,2'-bipyridine-4,4'-dicarboxylate, dpp = 2,3-bis(2-pyridyl)pyrazine). 560-nm and 600-nm bandpass filters in the emission monochromator are used for $[Ir(deeb)_2Cl_2](PF_6)$ and $[Ir(deeb)_2(dpp)](PF_6)_3$, respectively.

Table 3.2. Electronic spectral data for $[Ir(deeb)_2Cl_2](PF_6)$, $[Ir(bpy)_2Cl_2]^+$ [122] and $[Ir(deeb)_2(dpp)](PF_6)_3$ at room temperature.

Complex	Absorption		Emission			
	λ_{max} (nm)	ε (x 10^{-3} M^{-1} cm^{-1})		λ_{max} (nm)	τ (μs)	Φ
$[Ir(deeb)_2Cl_2](PF_6)$	308	28	CH_3CN	538	1.71 ± 0.17	0.33
	402	3.7	Solid	567	0.35 ± 0.02	-
	442 (sh)	2.2				
$[Ir(bpy)_2Cl_2]^+$	290	27	CH_3CN	510	0.344 ± 0.010	0.0066
	385	2.8	DMF	547	0.335 ± 0.015	0.0098
	430 (sh)	1.1				
$[Ir(deeb)_2(dpp)](PF_6)_3$	322	34	CH_3CN	540	1.23 ± 0.03	0.013
	334	32	Solid	599	0.14 ± 0.02	-

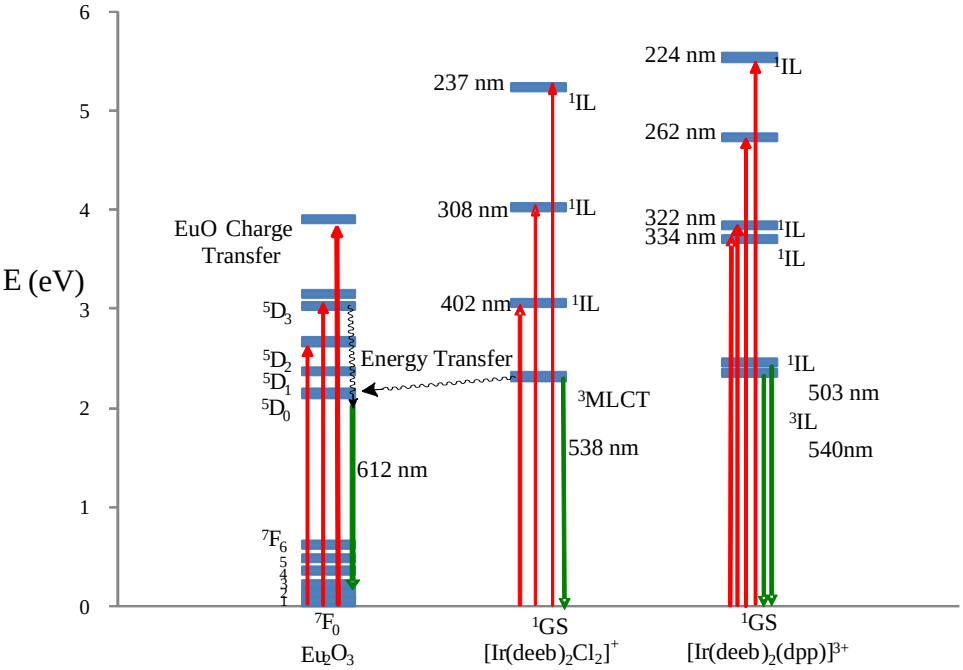

Figure 3.12. Energy diagram for Eu_2O_3, $[Ir(deeb)_2Cl_2](PF_6)$, and $[Ir(deeb)_2(dpp)](PF_6)_3$, where deeb = diethyl-2,2′-bipyridine-4,4′-dicarboxylate and dpp = 2,3-bis(2-pyridyl)pyrazine.

3.2 Characterization of Europium Oxide Nanoparticles

Scanning electron micrographs were obtained to determine the average particle diameter and size distribution of the synthesized nanoparticles. Typical SEM image and particle size distribution of as-prepared Eu_2O_3 nanoparticles synthesized at 100 Torr N_2 are shown in Figure 3.13. The average particle diameter is 11.0 ± 2.3 nm, consistent with that reported previously for synthesis of Eu_2O_3 nanoparticles at 100 Torr.[121] The size distribution obtained is relatively small, which is a known advantage of gas-condensation synthesis. X-ray diffraction patterns (Figure 3.14) were also obtained for phase and particle size analyses. A composition of 84.7% monoclinic and 15.3% cubic phases were obtained, which is typical for Eu_2O_3 nanoparticles synthesized in the same conditions.[109,123] Using the Scherrer equation (Figure 3.13B),[109] an average particle diameter of 12.0 ± 2.3 nm was obtained, which is consistent with the SEM measurements and previous reports.[109]

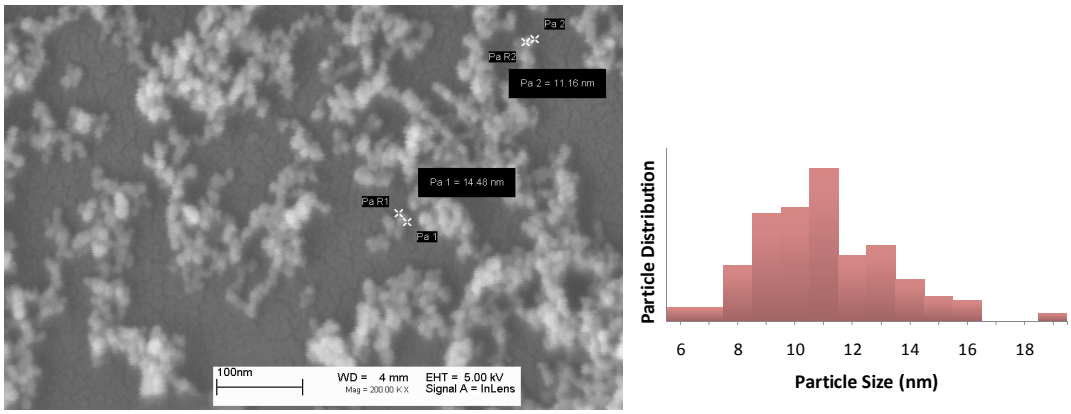

Figure 3.13. SEM image and particle size distribution of as-prepared Eu_2O_3 nanoparticles synthesized at 100 Torr N_2.

(A)

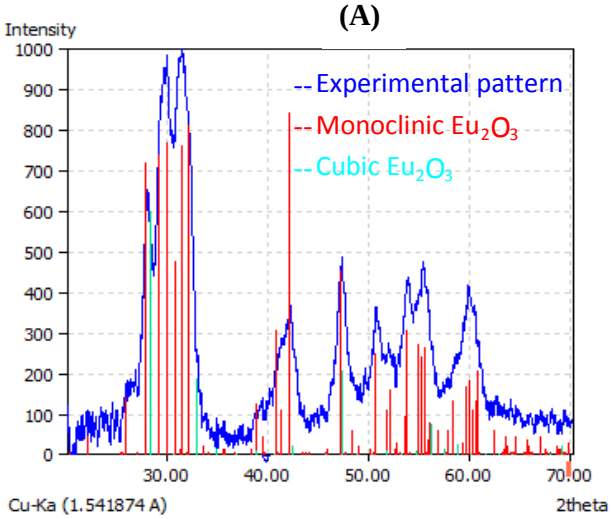

(B)

Scherrer equation

$$B(2\theta) = \frac{0.94\,\lambda}{L\cos(\theta)}$$

where B(2θ) = linewidth
λ = wavelength of radiation
θ = peak position
L = average particle diameter

Figure 3.14. (A) X-ray diffraction pattern of as-prepared Eu_2O_3 nanoparticles synthesized at 100 Torr N_2, and standard patterns for monoclinic and cubic Eu_2O_3; (B) the Scherrer equation.[124]

The Y_2O_3 nanoparticles were predominantly monoclinic and have an average of 10 ± 1 nm in diameter, consistent previous reports on Y_2O_3 nanoparticles synthesized *via* gas phase condensation.[124]

Table 3.3 and Figure 3.15 show results from the ATR-FTIR spectroscopy of europium oxide nanoparticles obtained under vacuum. A broad peak centered at ~3500 cm^{-1} due to hydrogen-bonded hydroxyl groups[110,125] and a very weak absorption peak at 3685 cm^{-1} due to free surface hydroxyl groups[110,126] were observed for Eu_2O_3 nanoparticles at room temperature. Gradual heating of the Eu_2O_3 nanoparticles from 25°C to 200°C and back to 25°C was performed to destroy the surface hydrogen bonds which caused a decrease in the intensity of the broad peak at 3500 cm^{-1} and revealed the free -OH more clearly (Figure 3.15). The surface -OH groups in the unmodified Eu_2O_3 nanoparticles could be responsible for hydrolyzing one or more of the ester groups on the deeb ligand to attach the iridium complex on the oxide. The infrared spectra of Eu_2O_3 also feature strong and broad peaks from 1550-850 cm^{-1} due to adsorbed CO_2 or carbonate species on europium oxide due to exposure to air.[127-133]

Spectral characterization of Eu_2O_3 nanoparticles was performed using solid state reflection, emission and excitation spectroscopy. In Figure 3.16, the resulting spectrum after the reflection spectrum of Eu_2O_3 nanoparticles is transformed to the Kubelka-Munk function can be seen, which partly shows a trace of the intense Eu^{3+}-O^{2-} charge transfer band at 250 nm and weak *4f* transition bands at 394 and 460 nm consistent with previous reflection spectrum of Eu_2O_3.[134] When excited at 395 nm, the emission spectrum at 77K (Figure 3.17A) shows sharp relaxation bands from the $^5D_0$ to several ^7F_J states, the most intense of which is the $^5D_0 \rightarrow {}^7F_2$ transition at 610-630 nm that is characteristic of Eu^{3+} luminescence. Only two of the possible five J sublevels, centered at 615 nm and 625 nm, were visible in the emission spectrum due to limited resolution. Monitoring the most intense band at 615 nm yields the $^7F_0 \rightarrow {}^5D_3$ band at 395 nm as the most intense f-f transition in the excitation spectrum, along with the Eu^{3+}-O^{2-} charge transfer band. The CT band is broad because it is an electronic transition between two species and hence between

two potential energy curves with a larger internuclear distance compared to that for f-f transitions. It is also relatively more intense because there is no selection rule that forbids the transition.[135] Luminescence lifetime decay curves obtained after excitation of the $^7F_0 \rightarrow {}^5D_3$ band at 395 nm and monitoring the $^5D_0 \rightarrow {}^7F_2$ transition at 615 nm at room temperature are shown in Figure 3.17C-D. A biexponential fit of the decay at gate width = 1 ms (Figure 3.17C) show lifetimes at around 30 μs and 120 μs. Figure 3.17D is a monoexponential fit to more accurately determine the shorter decay time. The lifetime component at 30 μs corresponds to luminescence from site C (label in accordance with that used in refs.[6]) in monoclinic Eu_2O_3 nanoparticles, which was reported to be 36 μs for 14 nm particles at low temperature.[136,137] The longer lived component, on the other hand, could be attributed to emission from site C of the cubic phase present in as-prepared nanocrystalline Eu_2O_3, which was reported 183 μs at 12 K.[138]

Table 3.3. Infrared peaks of Eu_2O_3 nanoparticles under vacuum.

Absorption Peaks	Assignment
3685	Free surface O–H stretch[110,126,139]
~3500	Hydrogen-bonded O–H stretch[110,125]
1543, 1431	asymmetric and symmetric O−C−O stretch of carbonate[127-133]
1076	symmetric C−O stretch of CO_2[132]
849	out of plane bending of CO_2[128,133]

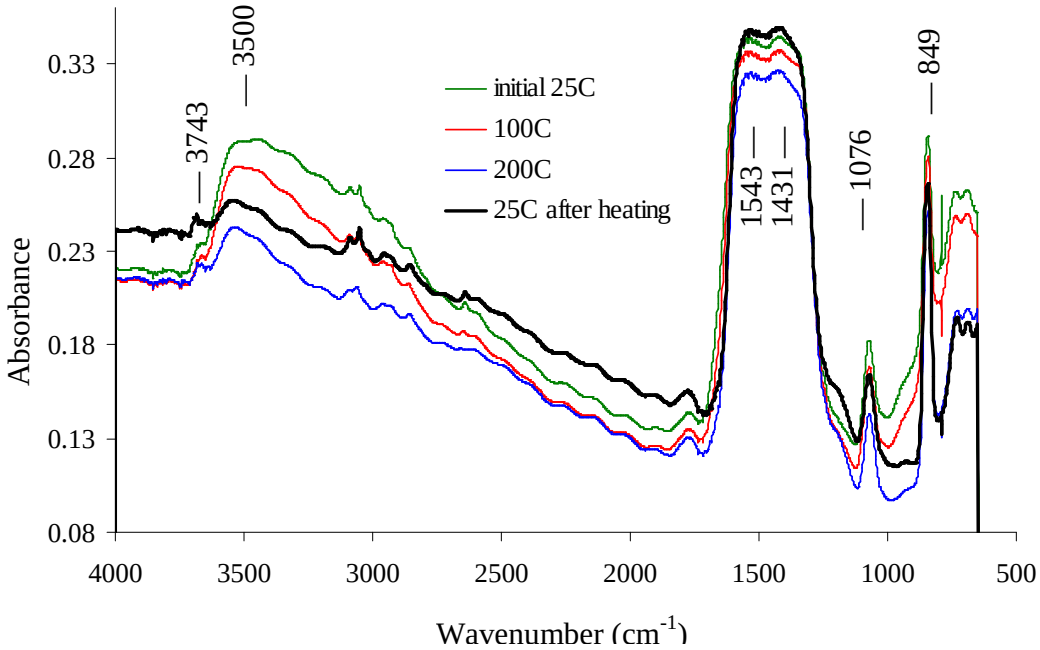

Figure 3.15. ATR-FTIR spectra of Eu_2O_3 nanoparticles under vacuum with gradual heating.

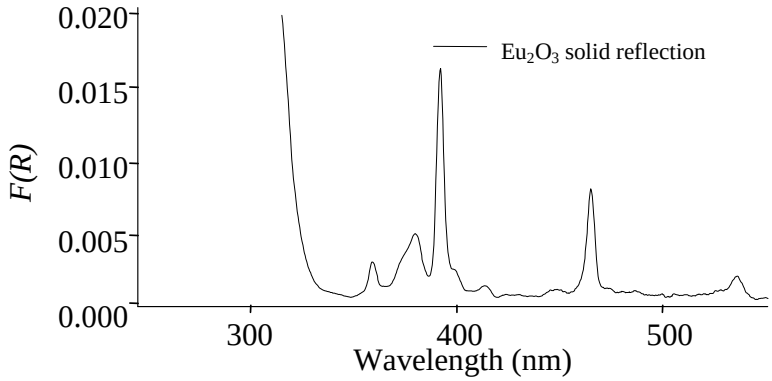

Figure 3.16. Solid reflection spectra of modified Eu_2O_3 nanoparticles, where *F(R)* is the Kubelka–Munk coefficient, $F(R) = (1-R)^2/2R$, where $R = J/J_{ref}$ and J is the reflected intensity of the sample.[140]

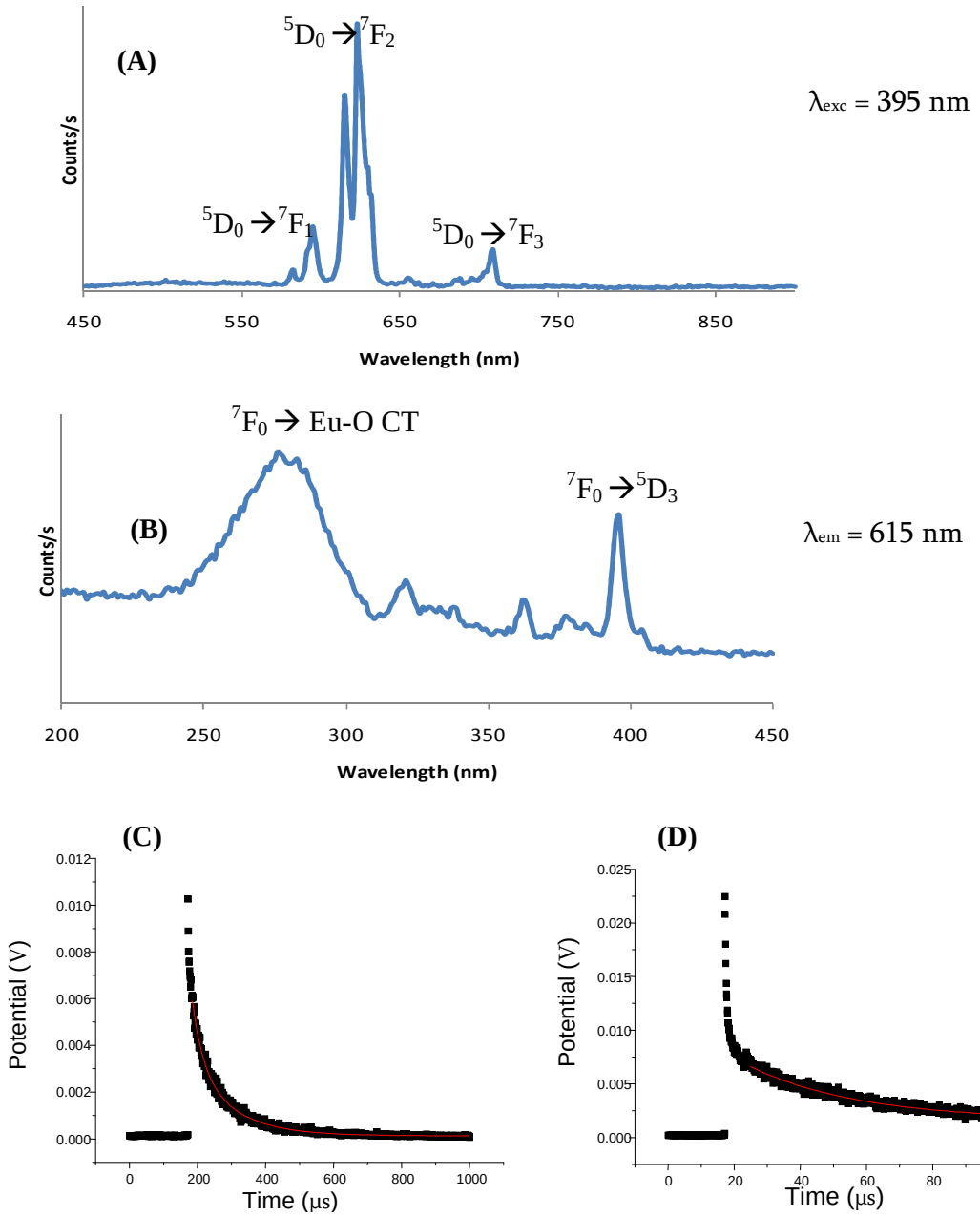

Figure 3.17. Spectroscopic data for as-prepared Eu_2O_3 nanoparticles synthesized at 100 Torr N_2. (A) Emission spectrum at 77K (λ_{exc} = 395 nm); (B) excitation spectrum at 77 K (λ_{em} = 615 nm); lifetime decay at RT (λ_{exc} = 395 nm, λ_{em} = 615 nm) with gate widths of (C) 1 ms and (D) 100 μs.

Chapter 4 - Ruthenium, Rhodium and Iridium Monometallic Complexes on Europium Oxide Nanoparticles

4.1 Attachment of Metal Complexes on Nanoparticles

4.1.1 Mode of Binding of Complexes on Nanoparticles

ATR-FTIR spectroscopy was used to determine the modes of binding of the metal complexes because of characteristic IR vibrations found in carboxyl-containing compounds. The spectra of Eu_2O_3 nanoparticles and the complexes in pure solid form and on the nanoparticles at ambient conditions are shown in Figure 4.1. Spectra of the stained particles contain characteristic stretching vibrations of both the Eu_2O_3 nanoparticles and the metal complexes. The ν(C-O) asymmetric and symmetric stretch in Eu_2O_3 (1385 cm^{-1} and 1500 cm^{-1}, respectively) due to carbonate species on the metal-oxide surface were unshifted in the modified particles. The ν(C=O) stretch in $[Ru(deeb)_2Cl_2]$ (1712 cm^{-1}) was also present, although shifted to 1724 cm^{-1} for the Eu_2O_3 nanoparticles modified with $[Ru(deeb)_2Cl_2]$. The same trend was observed for Eu_2O_3 with $[Rh(deeb)_2Cl_2](PF_6)$ with the ν(C=O) stretch shifting from 1722 to 1732 cm^{-1} when anchored on the metal oxide. The persistence of the carbonyl stretch in the complexes upon attachment indicates a monocovalent, ester-type linkage of the complexes to Eu_2O_3, as shown in structure A in Figure 4.1, similar to those observed on TiO_2 and SnO_2 for dicarboxylic acid bpy analogs, or incomplete hydrolysis.[138] A carboxylate, chelating mode of binding (structure B, C or D) determined from a strong band at ~1600 cm^{-1} was previously reported for deeb-containing complexes on TiO_2 upon complete ester hydrolysis,[63] which is absent or only weakly observed for the complexes on Eu_2O_3. Peaks at ~1730 cm^{-1} have been interpreted previously as monoester linkage or incomplete hydrolysis of the deeb ester moieties.[11,13,14,65] Other characteristic ester stretching vibrations such as ν(C-(C=O)-O) at ~1260 cm^{-1} and ν(O-C-C) at ~1120 cm^{-1} of the

complexes in this study seem to be unshifted when attached to the oxide. This may also suggest that there is a significant percentage of ester moieties that remain unhydrolyzed when anchored to the oxide surface. Hydrolysis of all four ester groups in the metal complexes is not necessary to achieve metal oxide surface saturation with the deeb complexes.

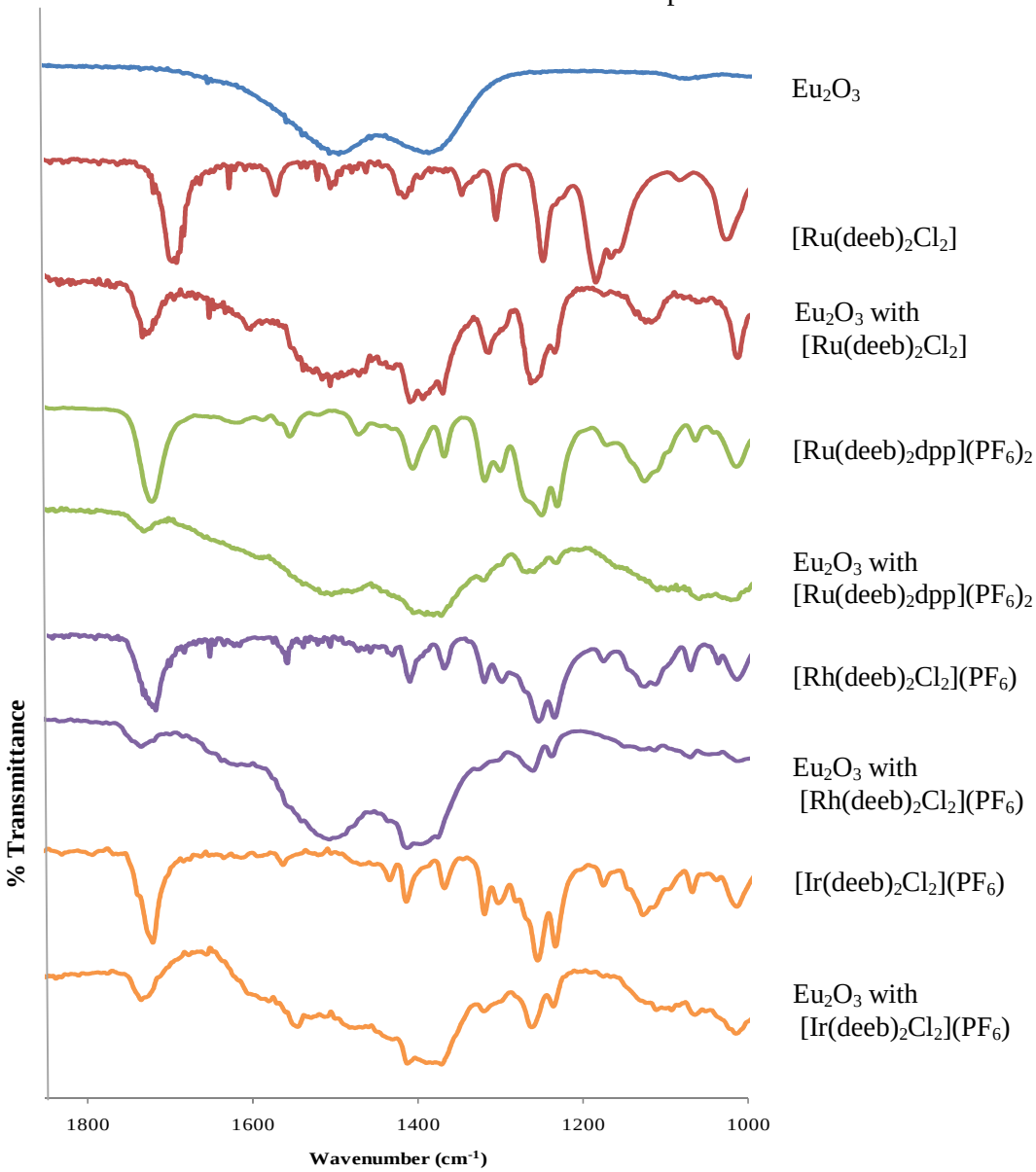

Figure 4.1. ATR-FTIR spectra of Eu_2O_3, $[Ru(deeb)_2Cl_2]$, Eu_2O_3 modified with $[Ru(deeb)_2Cl_2]$, $[Rh(deeb)_2Cl_2](PF_6)$, and Eu_2O_3 modified with $[Rh(deeb)_2Cl_2](PF_6)$ at ambient conditions, where deeb = diethyl-2,2'-bipyridine-4,4'-dicarboxylate. Spectra do not have the same transmittance range.

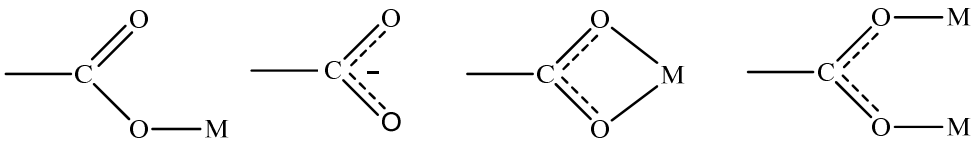

Figure 4.2. Various modes of attachment of carboxylate-containing ligands on metal oxides.

To determine if hydroxyl groups on the surface of Eu_2O_3 reacted with the ester group of the deeb ligand and attach$[Ir(deeb)_2Cl_2]^+$ to Eu_2O_3, the ATR-FTIR spectrum of the modified nanoparticles were obtained under vacuum to remove surface water. Table 4.1 and Figure 4.3 show ATR-FTIR spectra of europium oxide nanoparticles, the nanoparticles modified with $[Ir(deeb)_2Cl_2]^+$, and solid $[Ir(deeb)_2Cl_2](PF_6)$ under vacuum. The IR spectrum of the Eu_2O_3 nanoparticles modified with $[Ir(deeb)_2Cl_2]^+$ (Figure 4.3b), shows a decrease in intensity of the free -OH signal which could be due to reaction with deeb. A very faint trace of the hydroxyl groups may suggest that the modified oxide surface is not completely covered by the iridium complex or that deeb reacting with the hydroxyl groups was not the absolute mode of attachment of the iridium complex to Eu_2O_3. Direct coordination or electrostatic interaction between the metal ion in the oxide and the carboxyl group of the metal complex are other mechanisms for attachment.[110,126] It is, however, difficult to draw conclusions based on the spectrum. The infrared spectra of the modified and unmodified Eu_2O_3 also feature strong and broad peaks from 1550-850 cm^{-1} due to adsorbed CO_2 or carbonate species on europium oxide due to exposure to air.[141]

From Figures 4.3b and c (the resultant spectrum after subtracting the Eu_2O_3 spectrum from the modified Eu_2O_3 spectrum), two peaks at 1754 and 1649 cm^{-1} can be seen at the carbonyl region for the iridium complex species on Eu_2O_3, consistent with carboxylato ligands on metal

oxides.[127-133] The higher energy ν(C=O) stretch at 1754 cm^{-1} suggests that the complex is attached *via* a monoester-type linkage (A) due to the significant shift from 1718 cm^{-1} in the pure complex (Figure 4.3d). However, the signal at 1649 cm^{-1} indicates that carboxylate modes B, C and D among others mentioned by Meyer *et al.* may also occur alongside on Eu_2O_3.[14,142,143]

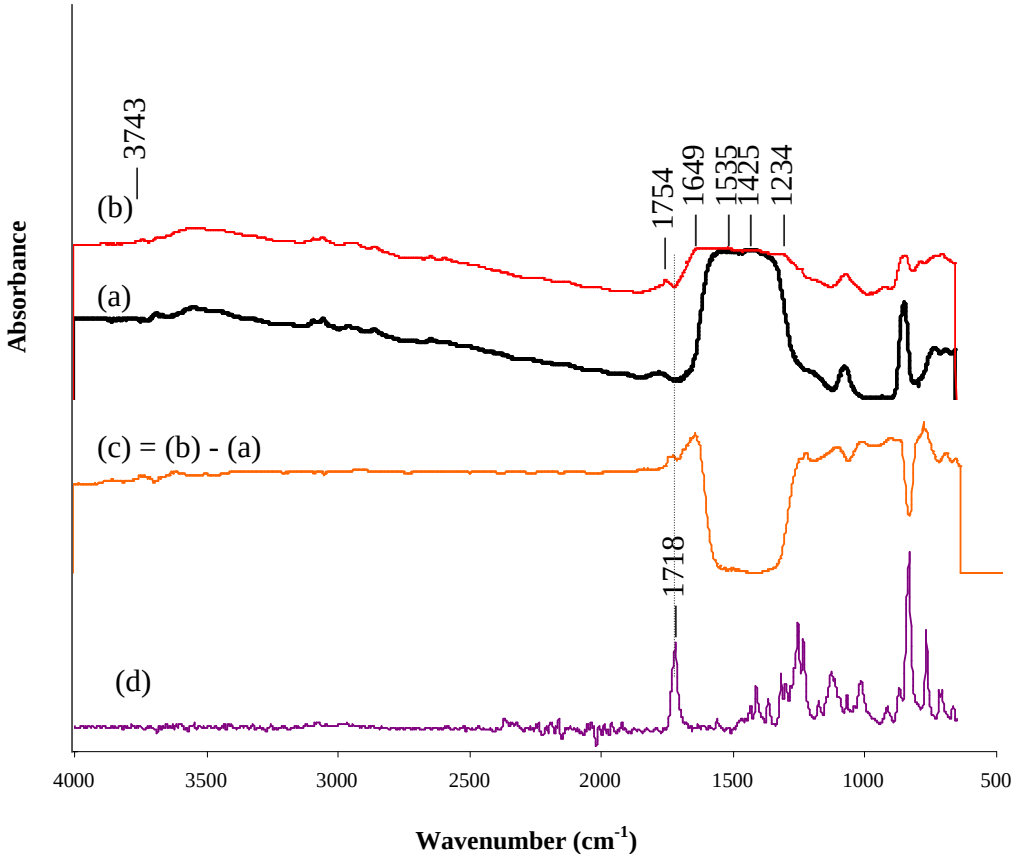

Figure 4.3. ATR-FTIR spectra of (a) Eu_2O_3, (b) Eu_2O_3 modified with $[Ir(deeb)_2Cl_2]^+$, (c) Eu_2O_3 modified with $[Ir(deeb)_2Cl_2]^+$ minus Eu_2O_3, and d) solid $[Ir(deeb)_2Cl_2](PF_6)$, where deeb = diethyl-2,2'-bipyridine-4,4'-dicarboxylate.

Table 4.1. Infrared peaks of Eu_2O_3 nanoparticles, Eu_2O_3 modified with $[Ir(deeb)_2Cl_2]^+$ and $[Ir(deeb)_2Cl_2](PF_6)$.

Eu_2O_3	Eu_2O_3 modified with $[Ir(deeb)_2Cl_2]^+$	$[Ir(deeb)_2Cl_2](PF_6)$	Assignment
3685	3743		Free surface O–H stretch on Eu_2O_3[143]
~3500	~3500		Hydrogen-bonded O–H stretch on Eu_2O_3[110,126,139]
	1754	1718	asymmetric C=O stretch of deeb[41,50,51]
	1649		asymmetric O−C−O stretch of hydrolyzed deeb[110,125]
1543, 1431	1535, 1425		asymmetric and symmetric O−C−O stretch of carbonate on Eu_2O_3[14,142,143]
	1234	1255, 1232	asymmetric and symmetric C−O stretch of deeb[127-133]
1076	1078		symmetric C−O stretch of CO_2 on Eu_2O_3[139,144,145]
849	850		out of plane bending of CO_2 on Eu_2O_3[128,132,133]

4.1.2 Quantitative Surface Binding Studies

Ruthenium complexes are known to form monolayers on metal oxides and surface coverage can be determined by equilibrating various concentrations of the complexes in solution and measuring the adsorbed complex spectroscopically. Figures 4.4a shows the Langmuir isotherm of $[Ru(deeb)_2(dpp)]^{2+}$ on 12-nm Eu_2O_3 nanoparticles which follows equation 15, where Γ = amount of complex adsorbed, Ceq = solution concentration at equilibrium, Γ_0 = maximum coverage amount and θ = coverage. Saturation surface coverage, Γ_0, and surface adduct formation constant, K_{ad} , values of 3.0 x 10^{-8} mol/cm^2 and 1.5 x 10^5 M^{-1} were determined from the slopes and intercepts of Figure 4.4b.

$$\frac{\Gamma}{\Gamma_0} = \theta = \frac{c_{eq} K_{ad}}{1 + c_{eq} K_{ad}} \qquad (15)$$

The surface coverage of $[Ru(deeb)_2dpp]^{2+}$ is comparable to similar compounds on TiO_2 and SnO_2.[146]

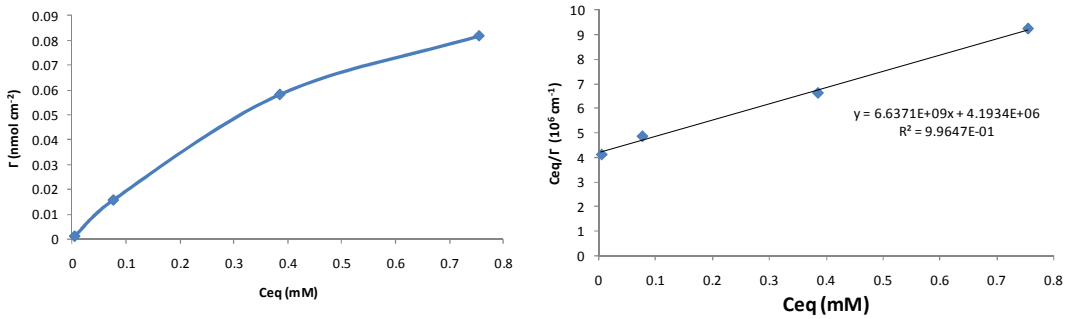

Figure 4.4. Langmuir isotherm plots of $[Ru(deeb)_2(dpp)]^{2+}$ on 12-nm Eu_2O_3 nanoparticles, where Γ = amount of complex adsorbed, Ceq = solution concentration at equilibrium.

4.1.3 Energy Dispersive X-ray (EDX) Analysis

Energy Dispersive X-ray (EDX) analysis was performed to quantitatively evaluate the amount of iridium complex adsorbed on Eu_2O_3 and Y_2O_3 nanoparticles. Table 4.3 shows the elemental composition of metal oxide nanoparticles modified with $[Ir(deeb)_2Cl_2]^+$ and $[Ir(deeb)_2(dpp)]^{3+}$. The relative amount of complex species attached on the metal oxide can be determined from the atomic ratio of the metal M (M= Eu or Y) to Ir. A comparable M/Ir ratio was observed for the $[Ir(deeb)_2Cl_2]^+$ species on Eu_2O_3 and Y_2O_3 (a difference of 3%), which suggests that $[Ir(deeb)_2Cl_2]^+$ on Y_2O_3 is a suitable model for the $[Ir(deeb)_2Cl_2]^+$ complex species after ester hydrolysis and attachment to the metal oxide surface. For $[Ir(deeb)_2(dpp)]^{3+}$, on the other hand, there is a larger discrepancy (11%) between the amount of bound material on Eu_2O_3 and Y_2O_3. There are no percent nitrogen reported because of the low weight percent of N atoms in the samples and the overlap of the N atom with the O atom signal in the EDX spectra. A considerably higher percentage of carbon was observed for all modified metal oxides which could be due to adsorbed carbonate species from exposure to air. In addition, a low percentage of oxygen on the modified oxides was seen most likely due to oxygen vacancies known to occur in

nanocrystalline Eu_2O_3.[146,147] There is also a noticeable loss of Cl ions from $[Ir(deeb)_2Cl_2]^+$ upon binding to Eu_2O_3 and Y_2O_3, which could mean that the Ir^{3+} ions are capable of binding themselves directly to the oxide and possibly carbonate species on the nanoparticles and that the metal complex species could have different orientations on the metal oxide surface upon binding. Surface adsorption, Γ, of both iridium complexes on Eu_2O_3 and Y_2O_3 were also calculated using the M/Ir ratio and nanoparticle diameters. Γ values obtained for both iridium complexes on Eu_2O_3 and Y_2O_3 nanoparticles correspond to limiting surface coverages calculated for ruthenium analogs on 16-24-nm TiO_2 nanofilms,[148] but are one to two orders of magnitude lower than experimental coverages. They are however consistent with adsorption values on In_2O_3.[149,150] Higher surface coverage of $[Ir(deeb)_2Cl_2]^+$ compared to $[Ir(deeb)_2(dpp)]^{3+}$ on Eu_2O_3 and Y_2O_3 is consistent with the larger size of the dpp ligand that prevents more $[Ir(deeb)_2(dpp)]^{3+}$ from anchoring on the nanoparticle surface. The lability of Cl^- and consequently direct binding of Ir^{3+} in $[Ir(deeb)_2Cl_2]^+$ also provide additional mode of attachment of this complex to the oxides. Another comparison noted is the lower surface coverages on Y_2O_3 compared to Eu_2O_3, which is unexpected with the smaller particle size and surface area of the former. In previous ester hydrolysis studies, the nature of the metal ion in the oxide affects the mode of binding and surface coverage of the metal complex to the oxide surface.[143] One factor to consider is the higher ionic polarizability of Eu^{3+} compared to Y^{3+} (4.53 *vs.* 3.81 $Å^3$)[13,141] which provides for greater electrostatic interaction and potential to coordination between Eu^{3+} and the carboxylate moeties in the hydrolyzed form of deeb.

Table 4.2. EDX analysis of $[Ir(deeb)_2Cl_2]^+$, $[Ir(deeb)_2(dpp)]^{3+}$ and $[Ru(deeb)_2(dpp)]^{2+}$ on Eu_2O_3 nanoparticles.

Mol %	Eu_2O_3 modified with $[Ir(deeb)_2Cl_2]^+$	Eu_2O_3 modified with $[Ir(deeb)_2(dpp)]^{3+}$	Eu_2O_3 modified with $[Ru(deeb)_2(dpp)]^{2+}$
C	50.396	49.917	48.638
N	0	0	3.995
O	24.679	14.159	19.194
Cl	0.169	-	-
Eu	23.991	35.153	27.941
Ir or Ru	0.765	0.771	0.232
Eu/M ratio (M = Ir, Ru)	31.4	45.6	120.4
Γ (mol/cm^2)	2.88×10^{-10}	1.98×10^{-10}	7.50×10^{-11}

Table 4.3. EDX analysis of $[Ir(deeb)_2Cl_2]^+$, $[Ir(deeb)_2(dpp)]^{3+}$ and $[Ru(deeb)_2(dpp)]^{2+}$ on Y_2O_3 nanoparticles.

Mol %	Y_2O_3 modified with $[Ir(deeb)_2Cl_2]^+$	Y_2O_3 modified with $[Ir(deeb)_2(dpp)]^{3+}$	Y_2O_3 modified with $[Ru(deeb)_2(dpp)]^{3+}$
C	43.216	35.763	52.407
N	0	0	0.413
O	32.618	33.635	24.22
Cl	0.196	-	-
Y	23.251	29.867	22.841
Ir or Ru	0.720	0.735	0.119
Y/M ratio (M = Ir, Ru)	32.3	40.6	191.4
Γ (mol/cm^2)	1.04×10^{-10}	8.26×10^{-11}	1.75×10^{-11}

4.2 Photophysical Properties of Metal Complexes on Nanoparticles

Reflection spectra of ruthenium, rhodium and iridium complexes on Eu_2O_3 nanoparticles were obtained to determine if the photophysical properties of the complexes are retained when attached on Eu_2O_3 nanoparticles. As summarized in Figure 4.5, $[Rh(deeb)_2Cl_2](PF_6)$ has the ^{3}IL

state below the $^5D_0$ state of Eu_2O_3, which makes $[Rh(deeb)_2Cl_2](PF_6)$ a potential energy acceptor from Eu_2O_3 while $[Ir(deeb)_2Cl_2](PF_6)$ and $[Ir(deeb)_2(dpp)](PF_6)_3$ are potential energy donors to Eu_2O_3 nanoparticles.

4.2.1 Reflection Spectroscopy of Metal Complexes on Nanoparticles

The reflection spectrum of Eu_2O_3 nanoparticles with $[Ru(deeb)_2Cl_2]$ is shown in Figure 4.6a. Compared to the solution spectrum of $[Ru(deeb)_2Cl_2]$, the higher energy MLCT band at ~432 nm remains unshifted and the lower energy MLCT band is blue-shifted from 591 to 554 nm. The blue shift is consistent with previous reports for deeb-containing complexes upon hydrolysis of the ester moiety[8,137,151] and for dicarboxylic acid analogs upon deprotonation[14,105] when anchored to metal-oxide surfaces. The reflection spectrum of $[Ru(deeb)_2(dpp)](PF_6)_2$ on Eu_2O_3 in Figure 4.6b shows the $\pi\rightarrow\pi^*$ and $Ru(d\pi)\rightarrow dpp(\pi^*)$ as seen in the absorption spectrum of the complex

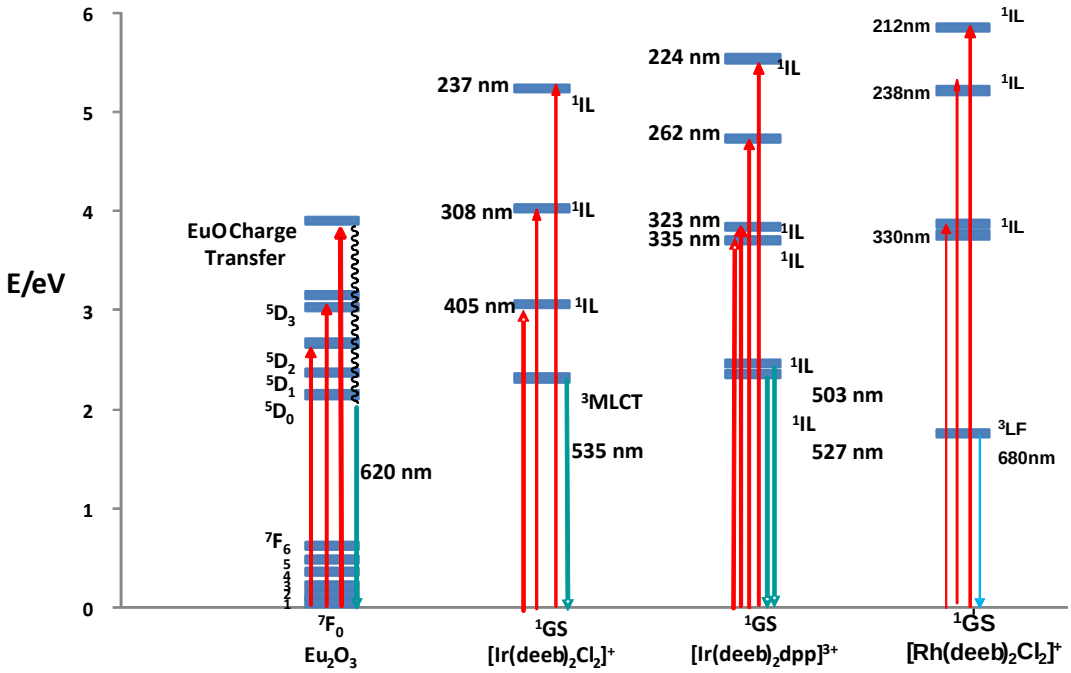

Figure 4.5. Energy diagram of Eu_2O_3, $[Rh(deeb)_2Cl_2](PF_6)$, $[Ir(deeb)_2Cl_2](PF_6)$ and $[Ir(deeb)_2(dpp)](PF_6)$.

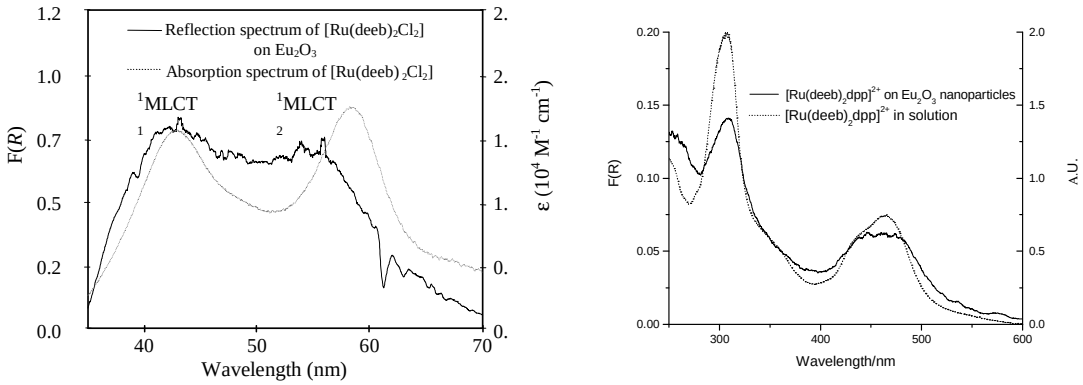

(a) (b)

Figure 4.6. Solid reflection spectrum of a) $[Ru(deeb)_2Cl_2]$ and Eu_2O_3 modified with $[Ru(deeb)_2Cl_2]$, and b) $[Ru(deeb)_2(dpp)](PF_6)_2$ and Eu_2O_3 modified with $[Ru(deeb)_2(dpp)](PF_6)_2$,where deeb = diethyl-2,2'-bipyridine-4,4'-dicarboxylate. F(*R*) is the Kubelka-Munk coefficient, $F(R) = (1-R)^2/2R$, where $R = J/J_{ref}$ and *J* is the reflected intensity of the sample.[112] The dotted line is the absorption spectrum in CH_2Cl_2 and CH_3CN solution (scale on right y-axis).

in solution. There were no significant shifts to the MLCT peak at 460 nm because there were no structural changes in the dpp ligand upon binding to the oxide. A spectrum for $[Rh(deeb)_2Cl_2](PF_6)$ is not shown due to instrumental limitations for peaks < 300 nm.

Figure 4.7a compares the electronic absorption spectrum of $[Ir(deeb)_2Cl_2]^+$ in CH_3CN and the reflection spectra of the complex attached on Y_2O_3 and Eu_2O_3. Both $\pi \rightarrow \pi^*$ and metal-to-ligand charge transfer (MLCT) transitions at 308 nm and 402 nm that are seen in the absorption spectrum of $[Ir(deeb)_2Cl_2]^+$ in CH_3CN are also discernible in the solid reflection spectrum of Y_2O_3 and Eu_2O_3 modified with $[Ir(deeb)_2Cl_2]^+$, with slight shifts as expected due to the conversion to the carboxylate upon covalent attachment. Figure 4.7b shows the electronic absorption and reflection spectra of $[Ir(deeb)_2(dpp)]^{3+}$ in CH_3CN and attached on Y_2O_3 and Eu_2O_3. The reflection spectra of $[Ir(deeb)_2(dpp)]^{3+}$ on the modified nanoparticles exhibit the internal ligand transition at ~ 330 nm also found in the absorption spectrum of the complex in solution, although not as shifted compared to the nanoparticles modified with $[Ir(deeb)_2Cl_2]^+$.

This could be due to the overlap of the deeb and bridging ligand (*e.g.* dpp) π→π* transitions at 300-320 nm as seen in ruthenium complexes with both ligands.[152] The reflection spectra of the Eu_2O_3 nanoparticles modified with the two complexes also feature absorption from 350-440 nm that may include absorption due to Eu_2O_3.

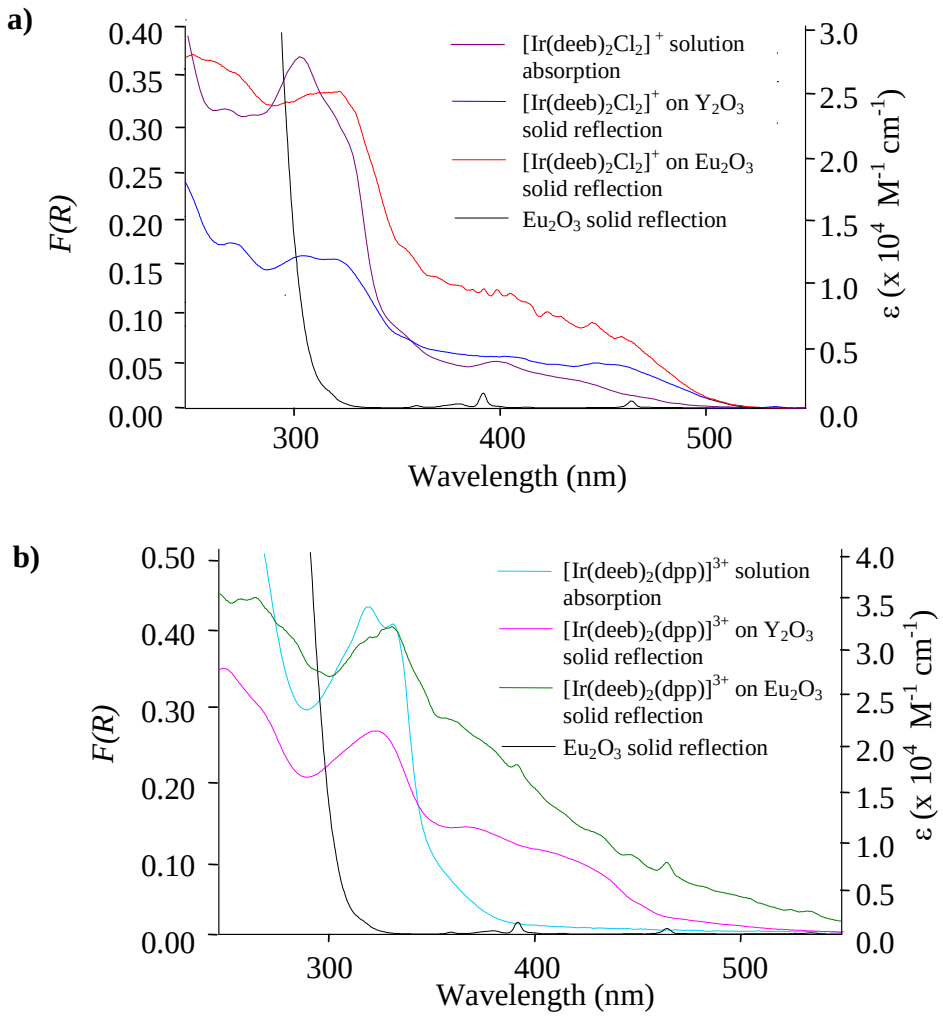

Figure 4.7. a) Solution absorption of $[Ir(deeb)_2Cl_2]^+$ and solid reflection spectra of modified Y_2O_3 and Eu_2O_3 nanoparticles; b) Solution absorption of $[Ir(deeb)_2(dpp)]^{3+}$ and solid reflection spectra of modified Y_2O_3 and Eu_2O_3 nanoparticles, where deeb = diethyl-2,2′-bipyridine-4,4′-dicarboxylate and dpp = 2,3-bis(2-pyridyl)pyrazine. *F(R)* is the Kubelka–Munk coefficient, $F(R) = (1-R)^2/2R$, where $R = J/J_{ref}$ and *J* is the reflected intensity of the sample.[140]

4.2.2 Emission Spectroscopy

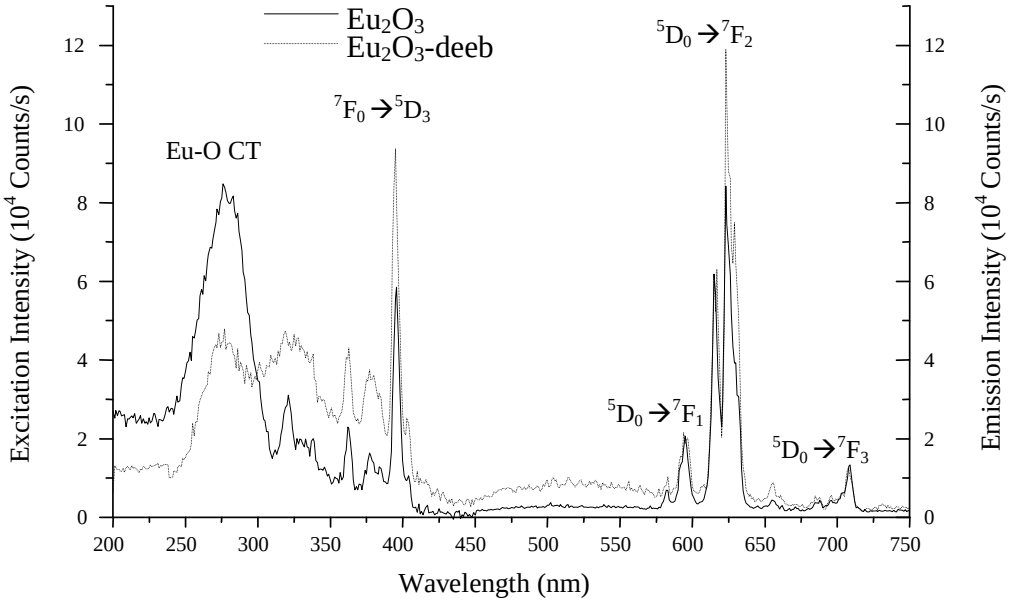

Figure 4.8. Excitation spectra (λ_{em} = 615 nm) and emission spectra (λ_{ex} = 394 nm) at room temperature of Eu_2O_3 and Eu_2O_3 modified with deeb = diethyl-2,2′-bipyridine-4,4′-dicarboxylate.

Even though the energy of the CT band is highly dependent on the coordination environment, there is no observable shift in the CT maximum for Eu_2O_3 modified with deeb shown in Figure 4.8. The intensity of the CT band is diminished for Eu_2O_3 modified with deeb probably due to a decrease in electron density on the oxide when deeb was adsorbed thereby reducing the chance for charge transfer to occur.

The solid-state emission spectra of $[Rh(deeb)_2Cl_2]^+$ on Eu_2O_3 nanoparticles were investigated at 77 K. Figure 4.9a and b show the emission spectra of unstained and stained Eu_2O_3 with $[Rh(deeb)_2Cl_2]^+$ exciting the $^7F_0 \rightarrow {}^5D_3$ (288 nm, a) and the $^7F_0 \rightarrow {}^5D_2$ (395 nm, b) transitions of Eu^{3+}. The data shows that it is possible to excite the nanoparticles through the coated surface to obtain the characteristic emission for a Eu_2O_3 nanoparticle. The emission of the rhodium complex at 680 nm was not observed upon excitation of Eu_2O_3 which suggests that energy

transfer did not occur for the modified nanoparticles. The ^{3}IL acceptor state of the rhodium complex albeit lower in energy compared to the $^5D_0$ state of Eu^{3+} may not be close enough to act as an acceptor state. When monitoring the characteristic Eu^{3+} emission at 615 nm in the excitation spectra in Figure 4.10a, a decrease in the relative intensity of Eu-O CT band at 288 nm compared to the $^7F_0 \rightarrow {}^5D_3$ of Eu^{3+} at 395 nm for Eu_2O_3 modified with $[Rh(deeb)_2Cl_2]^+$ was observed due to anchoring of the rhodium complex on the europium oxide surface. This is consistent with the partial removal of the electron density from the oxide ions in Eu_2O_3 when deeb was adsorbed thereby reducing the chance for charge transfer to occur. On the other hand, the theory of minimal to no energy transfer occuring is also supported by the excitation spectra in Figure 4.10b. When monitoring at the emission of $[Rh(deeb)_2Cl_2]^+$ at 680 nm, both the spectra of unstained and stained Eu_2O_3 nanoparticles show contribution from both the rhodium and europium species. However, after subtracting the contribution due to direct excitation of europium, the spectrum of the modified nanoparticles show mostly direct excitation of the rhodium species at 330 nm (^{1}IL state). Only a minimal contribution of the europium species excited at 400 nm was observed for the emission of the rhodium complex.

Figure 4.11a shows excitation spectra monitoring at 615 nm of Eu_2O_3 and $[Ir(deeb)_2Cl_2]^+$ on Y_2O_3 and Eu_2O_3. It is evident from the reflection spectra in Figure 4.7c and the Eu_2O_3 excitation spectrum in Figure 3.17b that the iridium complex absorbs at 440 nm while Eu_2O_3 does not. In the emission spectra in Figure 4.11a, $[Ir(deeb)_2Cl_2]^+$ on Y_2O_3 exhibits emission from the ^{3}MLCT state centered at 567 nm when excited with 440 nm light as expected of the iridium complex, while no Eu_2O_3 emission is observed. However, Eu_2O_3 modified with $[Ir(deeb)_2Cl_2]^+$ shows emission characteristic of both the iridium complex and Eu^{3+} upon 440 nm excitation, a wavelength that excites only the iridium complex. This observation is consistent with energy

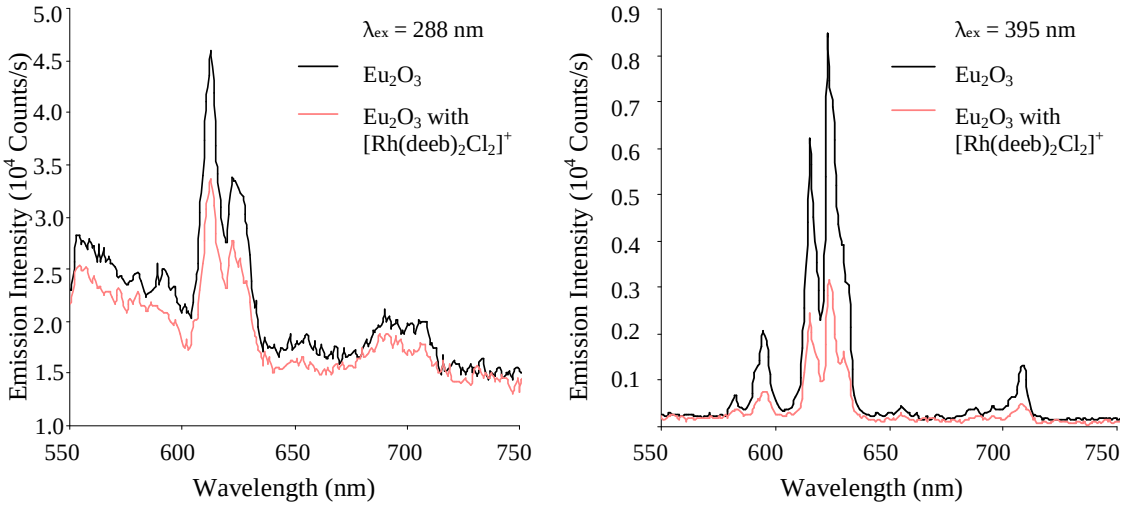

(a) (b)

Figure 4.9. Emission spectra exciting at a) λ_{ex} = 288 nm and b) λ_{ex} = 394 nm at 77 K of Eu_2O_3 and Eu_2O_3 modified with $[Rh(deeb)_2Cl_2]^+$, where deeb = diethyl-2,2'-bipyridine-4,4'-dicarboxylate.

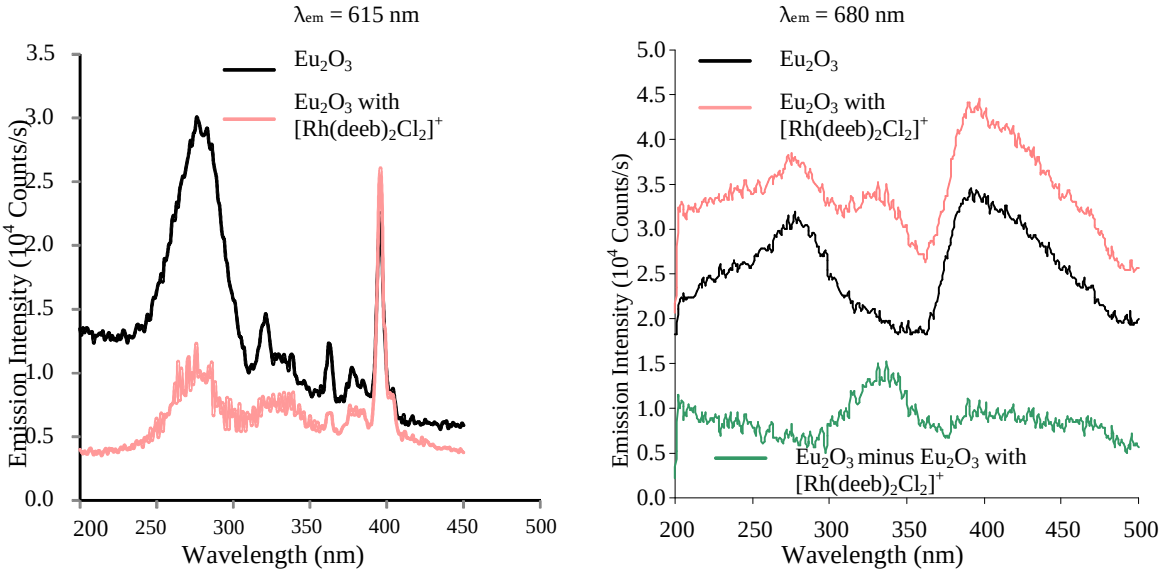

(a) (b)

Figure 4.10. Excitation spectra emitting at a) λ_{em} = 615 nm, and b) λ_{ex} = 395 nm at 77 K of Eu_2O_3 and Eu_2O_3 modified with $[Rh(deeb)_2Cl_2]^+$, where deeb = diethyl-2,2'-bipyridine-4,4'-dicarboxylate.

transfer from the iridium complex to Eu_2O_3 across the surface interface made possible by the very close energies of the ^{3}MLCT state of the Ir complex and the $^5D_0$ state of Eu^{3+} as shown in Figure 4.5. The excitation spectrum of Eu_2O_3 modified with $[Ir(deeb)_2Cl_2]^+$ monitoring the 615 nm Eu^{3+} emission shows an spectrum similar to $[Ir(deeb)_2Cl_2]^+$ on Y_2O_3 (maximum at 330 nm) that has a broad peak with a maximum at 338 nm and some faint trace of direct excitation of Eu^{3+} at 394 and 466 nm. This suggests that the Eu^{3+} emission from the modified Eu_2O_3 at 615 nm is mostly due to ET from $[Ir(deeb)_2Cl_2]^+$ and not mainly due to Eu_2O_3.

Figure 4.11b shows the excitation spectra monitoring at 615 nm and emission spectra exciting at 340 nm of Eu_2O_3 and $[Ir(deeb)_2(dpp)]^{3+}$ on Y_2O_3 and Eu_2O_3. The emission spectra of both Y_2O_3 and Eu_2O_3 modified with $[Ir(deeb)_2(dpp)]^{3+}$ when excited at 340 nm show a broad emission band centered at 610 nm due to the iridium species. Aside from the broad band, the emission spectrum of Eu_2O_3 modified with $[Ir(deeb)_2(dpp)]^{3+}$ also contains the sharp emission bands at 613 and 622 nm characteristic of Eu_2O_3. The excitation spectrum of Eu_2O_3 modified with $[Ir(deeb)_2(dpp)]^{3+}$ monitoring at 615 nm includes both a broad band centered at 330 nm characteristic of $[Ir(deeb)_2(dpp)]^{3+}$ as well as sharp bands at 394 and 466 nm characteristic of Eu_2O_3, but has more contribution from Eu_2O_3 compared to what is seen in $[Ir(deeb)_2Cl_2]^+$ on Eu_2O_3 (Figure 4.9a). This suggests that emission of Eu_2O_3 modified with $[Ir(deeb)_2(dpp)]^{3+}$ at 615 nm is due to a combination of direct excitation of Eu^{3+} and ET from $[Ir(deeb)_2(dpp)]^{3+}$. The lower surface coverage of $[Ir(deeb)_2(dpp)]^{3+}$ on Eu_2O_3 compared to that of $[Ir(deeb)_2Cl_2]^+$ from the EDX experiments could be one reason for the larger contribution of Eu_2O_3 in the 615 nm emission of Eu_2O_3 modified with $[Ir(deeb)_2(dpp)]^{3+}$.

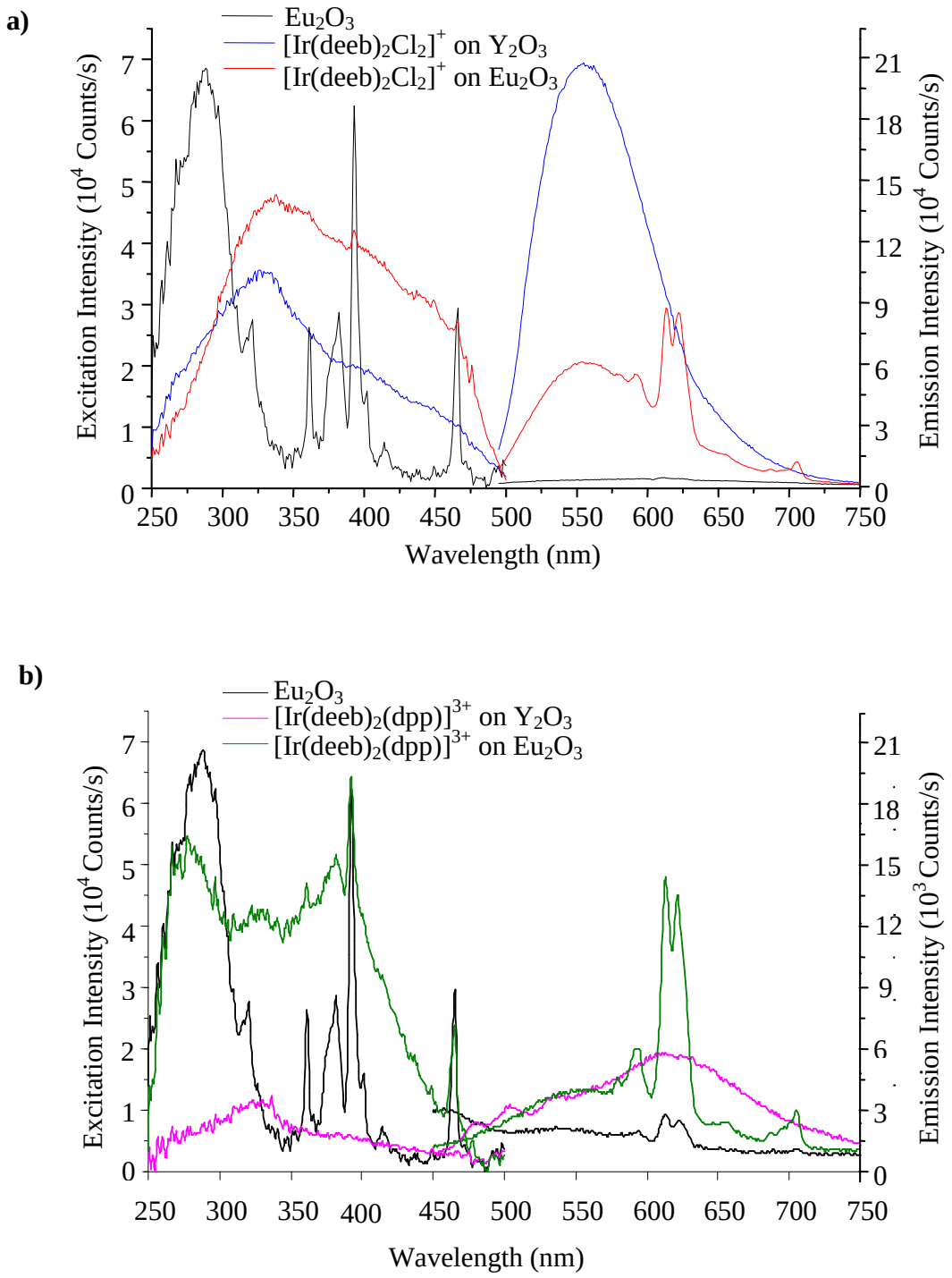

Figure 4.11. Excitation (λ_{em} = 615 nm) and emission spectra (λ_{ex} = 440 nm) at room temperature of a) Eu_2O_3, Y_2O_3 modified with $[Ir(deeb)_2Cl_2]^+$ and Eu_2O_3 modified with $[Ir(deeb)_2Cl_2]^+$; b) Eu_2O_3, Y_2O_3 modified with $[Ir(deeb)_2(dpp)]^{3+}$ and Eu_2O_3 modified with $[Ir(deeb)_2(dpp)]^{3+}$, where deeb = diethyl-2,2′-bipyridine-4,4′-dicarboxylate and dpp = 2,3-bis(2-pyridyl)pyrazine. A 340-nm bandpass filter and a 500 nm cut-off filter are used in the excitation and emission monochromators, respectively.

4.2.3 Lifetime Studies

The solid state lifetimes decay curves shown in Figure 4.12 were of Eu_2O_3 and Eu_2O_3 modified with $[Rh(deeb)_2Cl_2]^+$ at 77 K. The lifetime obtained for Eu_2O_3 at 77 K is higher compared to that at RT as shown in Figure 3.17 as expected. A decrease in the Eu_2O_3 cubic phase lifetime from 327 µs to 152 µs was observed which could either be due to energy transfer or quenching of the Eu_2O_3 lifetime due to surface adsorption of the rhodium complex. The rhodium complex may have been preventing the excitation of Eu_2O_3 by blocking the surface and block Eu^{3+} ions on the nanoparticle. Because this factor competes with establishing the energy transfer phenomenon, an opposite system where Eu^{3+} acts as the acceptor, as in the Eu^{3+}-Ir^{3+} systems, was investigated instead.

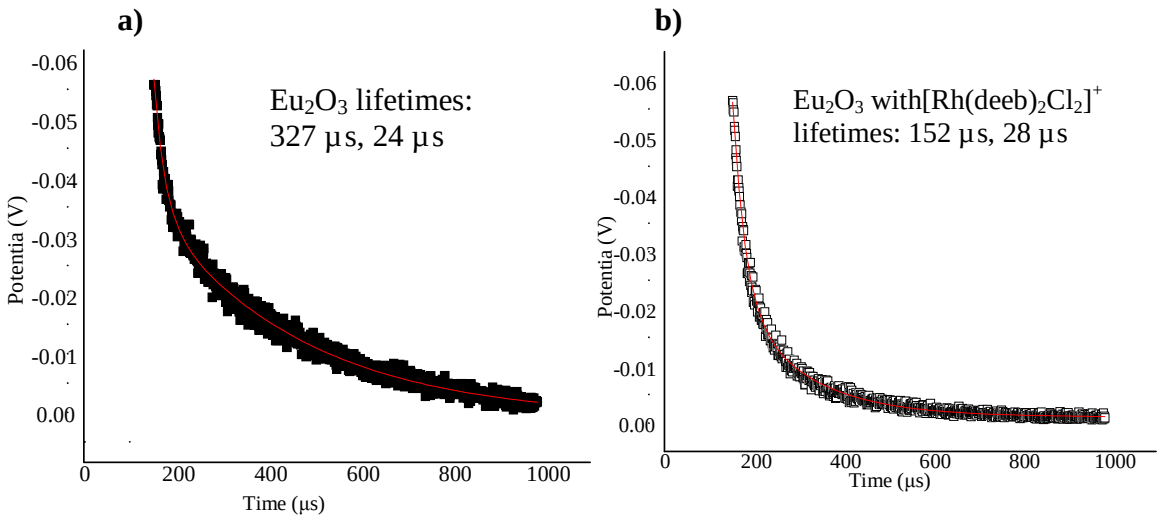

Figure 4.12. Lifetime decay profile of (a) as-prepared Eu_2O_3 nanoparticles synthesized at 100 Torr N_2 and (b) Eu_2O_3 nanoparticles modified with $[Rh(deeb)_2Cl_2]^+$ (λ_{ex} = 395 nm, λ_{em} = 615 nm) at 77 K with a gate width of 0.1 ms, where deeb = diethyl-2,2′-bipyridine-4,4′-dicarboxylate and dpp = 2,3-bis(2-pyridyl)pyrazine.

In the time-resolved phosphorescence spectroscopy of Eu_2O_3 and the $[Ir(deeb)_2Cl_2]^+$ complex on Y_2O_3 and Eu_2O_3, the characteristic emission light of the emitting species were

visually observed as the N_2 dye laser beam excites the solid samples. The unmodified Eu_2O_3 nanoparticles emit red light, $[Ir(deeb)_2Cl_2]^+$ on Y_2O_3 emits green light, and $[Ir(deeb)_2Cl_2]^+$ on Eu_2O_3 emits white light, similar to that observed by Coppo *et. al.* for their Ir-Eu-Ir trimetallic complex.[41] Luminescence lifetime decay curves obtained after excitation at 396 nm and monitoring at the emission wavelengths of the iridium complexes on Y_2O_3 and Eu_2O_3 are shown in Figure 4.13. A large decrease in emission lifetime from 0.28 to 0.09 μs at 555 nm, where $[Ir(deeb)_2Cl_2]^+$ emits, is observed in Figure 4.13a for $[Ir(deeb)_2Cl_2]^+$ attached on Eu_2O_3. This is consistent with energy transfer (68% efficiency as calculated using eq. 13) from the ^{3}MLCT state of the iridium complex to the $^5D_0$ state of Eu_2O_3. The calculated ET rate constant, k_T, for $[Ir(deeb)_2Cl_2]^+$ attached on Eu_2O_3 using eqs. (11) and (12) is 1.1 x 10^{-5} s^{-1} as shown on Table 4.4. Assuming the quantum yield of $[Ir(deeb)_2Cl_2]^+$ (ϕ_D) in solution remains the same when anchored on Y_2O_3, the radiative decay rate constant k_D and non-radiative decay rate constant k_{Di} of $[Ir(deeb)_2Cl_2]^+$ were calculated to be 1.2 x 10^{-6} and 2.4 x 10^{-6} s^{-1}, respectively, using eqs. (5), (6) and (7). Note that the above rate constants are very small quantities because the processes involved are in the solid state. Consequently, the quantum yield of $[Ir(deeb)_2Cl_2]^+$ on (ϕ_{DA}) Eu_2O_3 and the ratio of the Forster distance R_0 to the donor-acceptor distance R were found to be 0.080 and 1.2, respectively.

The lifetime decay curves of $[Ir(deeb)_2(dpp)]^{3+}$ on Y_2O_3 and Eu_2O_3 shown in Figure 4.13b are measured at 565 nm instead of the emission maximum of $[Ir(deeb)_2(dpp)]^{3+}$ on Y_2O_3 at 610 nm so that the Eu_2O_3 emission would not overlap. When excited at 396 nm the lifetime of $[Ir(deeb)_2(dpp)]^{3+}$ is reduced from 0.20 to 0.10 μs when attached to Eu_2O_3 also consistent with ET (50% efficiency) of $[Ir(deeb)_2(dpp)]^{3+}$ to Eu_2O_3. The lower ET efficiency observed in the $[Ir(deeb)_2(dpp)]^{3+}$ system compared to that in $[Ir(deeb)_2Cl_2]^+$ is consistent with the excitation

spectra of the modified Eu_2O_3 nanoparticles and is again attributed to a lower surface coverage of $[Ir(deeb)_2(dpp)]^{3+}$ than $[Ir(deeb)_2Cl_2]^+$ on Eu_2O_3. Kinetic parameters were also calculated for $[Ir(deeb)_2(dpp)]^+$on Eu_2O_3 as shown in Table 4.4, again assuming that the quantum yield for $[Ir(deeb)_2(dpp)]^+$on Y_2O_3 is the same for $[Ir(deeb)_2(dpp)]^+$ in solution. The energy transfer rate constant for $[Ir(deeb)_2(dpp)]^+$on Eu_2O_3 was very similar to that for $[Ir(deeb)_2Cl_2]^+$ on Eu_2O_3 which suggests a similar change in the quantum yields of both systems in solution and after anchoring on Eu_2O_3, and hence a similar manner of coordination for the two complexes on Eu_2O_3.

It must be noted that aside from energy transfer, quenching of the Ir^{3+} emissions may also occur because no risetime in the lifetime transients were observed. Also, as mentioned before, excitation of both the complexes and europium occur to cause emission from both species.

Table 4.4. Kinetic parameters for energy transfer of $[Ir(deeb)_2Cl_2]^+$ and $[Ir(deeb)_2(dpp)]^{3+}$ on Y_2O_3 and Eu_2O_3.

	$[Ir(deeb)_2Cl_2]^+$ on Y_2O_3	$[Ir(deeb)_2Cl_2]^+$ on Eu_2O_3	$[Ir(deeb)_2(dpp)]^{3+}$ on Y_2O_3	$[Ir(deeb)_2(dpp)]^{3+}$ on Eu_2O_3
λ_{ex} (nm)	396		396	
λ_{em} (nm)	555		565	
τ (us)	0.28	0.09	0.20	0.10
ϕ	0.33 (solution)	0.080	0.013 (solution)	0.0043
E		0.68		0.50
k_T (s^{-1})		1.1×10^{-5}		1.0×10^{-5}
k_D (s^{-1})	1.2×10^{-6}		6.5×10^{-8}	
k_{Di} (s^{-1})	2.4×10^{-6}		4.9×10^{-6}	
R_0/R	1.2		1.1	

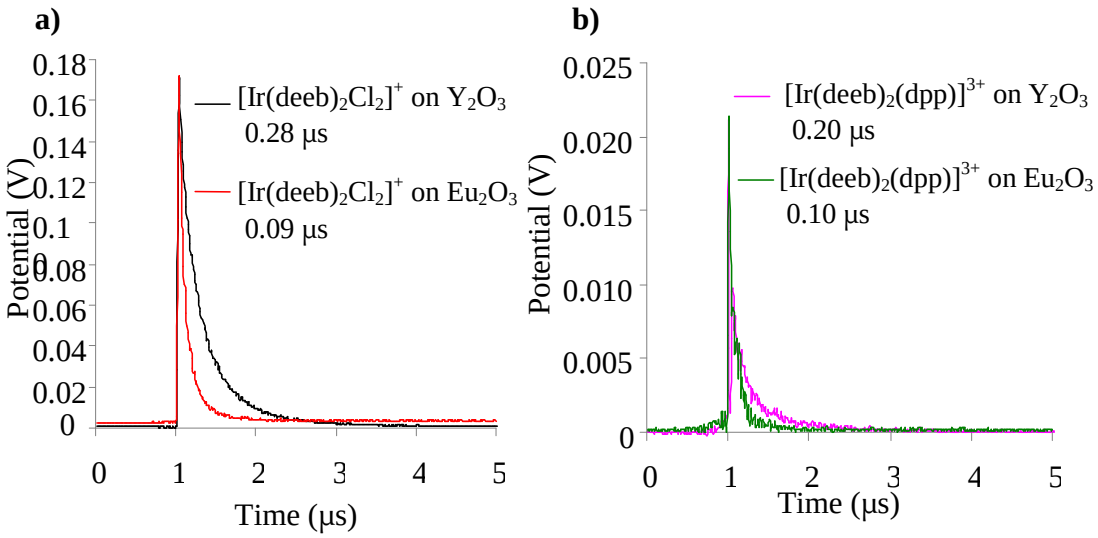

Figure 4.13. Lifetime decay profiles of (a) $[Ir(deeb)_2Cl_2]^+$ anchored on nanocrystalline Y_2O_3 and Eu_2O_3 (λ_{ex} = 396 nm, λ_{em} = 555 nm); and (b) $[Ir(deeb)_2(dpp)]^{3+}$ anchored on nanocrystalline Y_2O_3 and Eu_2O_3 (λ_{ex} = 396 nm, λ_{em} = 565 nm) at RT, where deeb = diethyl-2,2′-bipyridine-4,4′-dicarboxylate and dpp = 2,3-bis(2-pyridyl)pyrazine. 560-nm and 600-nm bandpass filters in the emission monochromator are used for $[Ir(deeb)_2Cl_2](PF_6)$ and $[Ir(deeb)_2(dpp)](PF_6)_3$, respectively.

Chapter 5 - Conclusions and Future Work

Ruthenium complexes $[Ru(deeb)_2Cl_2]$ and $[Ru(deeb)_2(dpp)](PF_6)_2$, the rhodium complex $[Rh(deeb)_2Cl_2](PF_6)$ and iridium complexes $[Ir(deeb)_2Cl_2](PF_6)$ and $[Ir(deeb)_2(dpp)](PF_6)_3$ which contain the deeb ligand were synthesized and characterized by ^1H NMR and mass spectroscopies. Europium oxide nanoparticles are synthesized by gas phase condensation and characterized by SEM and Xray diffraction. The surface of europium oxide nanoparticles can be modified with metal complexes by equilibrating solutions of metal complexes with the nanoparticles. Metal complexes bind to europium oxide by forming a monolayer of metal complexes through a mixture of different modes of binding. Reflection spectra of modified nanoparticles are consistent with electronic absorption spectra of the complexes in solution which suggests retention of the metal complex excited states upon binding. Emission and excitation spectra of Eu_2O_3 modified with $[Rh(deeb)_2Cl_2]^+$ only show characteristics from Eu_2O_3 without evidence of energy transfer to the rhodium complex. The emission spectrum of Eu_2O_3 modified with $[Ir(deeb)_2Cl_2]^+$ show maxima for both the iridium complex and Eu_2O_3 upon excitation of only the iridium complex. Excitation spectra of Eu_2O_3 modified with $[Ir(deeb)_2Cl_2]^+$ monitoring the Eu^{3+} emission show excitation mainly due to $[Ir(deeb)_2Cl_2]^+$. The emission spectrum of Eu_2O_3 modified with $[Ir(deeb)_2(dpp)]^{3+}$ also shows characteristic bands of Eu_2O_3 and $[Ir(deeb)_2(dpp)]^{3+}$, and the excitation spectrum of the modified nanoparticles show contribution from both Eu_2O_3 and $[Ir(deeb)_2(dpp)]^{3+}$ to induce emission from Eu^{3+}. Reduction in the lifetimes of both $[Ir(deeb)_2Cl_2]^+$ and $[Ir(deeb)_2(dpp)]^{3+}$ was observed upon binding to Eu_2O_3. Both steady-state and time-resolved luminescence experiments indicate energy transfer of the iridium complexes to to Eu_2O_3 nanoparticles.

To further investigate the possibility of energy transfer from Eu_2O_3 to a rhodium complex, a control complex that would produce a similar extent of coverage on Eu_2O_3 but would not act as an energy acceptor from Eu_2O_3 could be employed to determine the decrease in intensity steady-state measurements and reduction in lifetime in time-resolved. To improve surface coverage of the metal complexes on nanoparticles, ligands with single carboxylate groups could be used. Also, addition of other metal complex moieities via bridging ligands on the nanoparticle surface to increase functionality and luminescence can be conducted for future work. Removal of the adsorbed carbonates by annealing and varying properties of the metal oxide by doping are also expected to produce greater luminescence intensity to these materials.

Appendices

Appendix A – 2D ^{1}H NMR Spectra of $[Rh(deeb)_2Cl_2](PF_6)$, $[Ir(deeb)_2Cl_2](PF_6)$ and $[Ir(deeb)_2(dpp)](PF_6)_3$

COSY ^{1}H NMR Spectrum of $[Rh(deeb)_2Cl_2](PF_6)$:

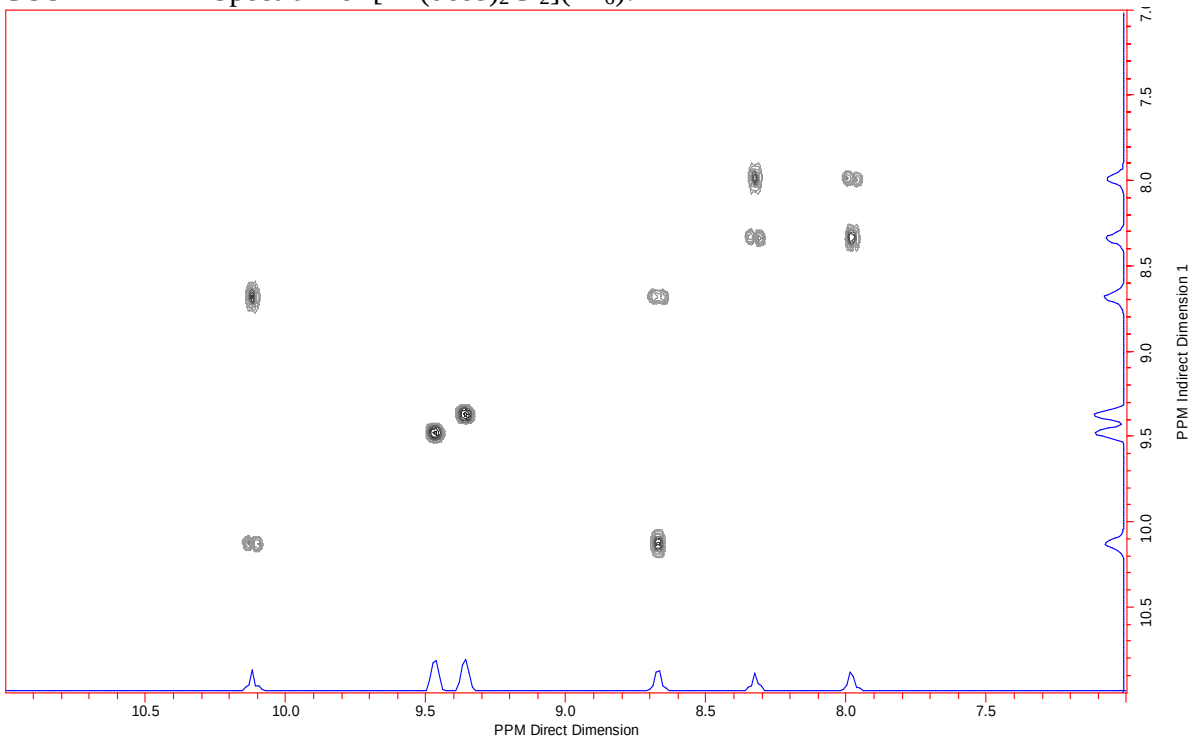

NOESY ^{1}H NMR Spectrum of $[Rh(deeb)_2Cl_2](PF_6)$:

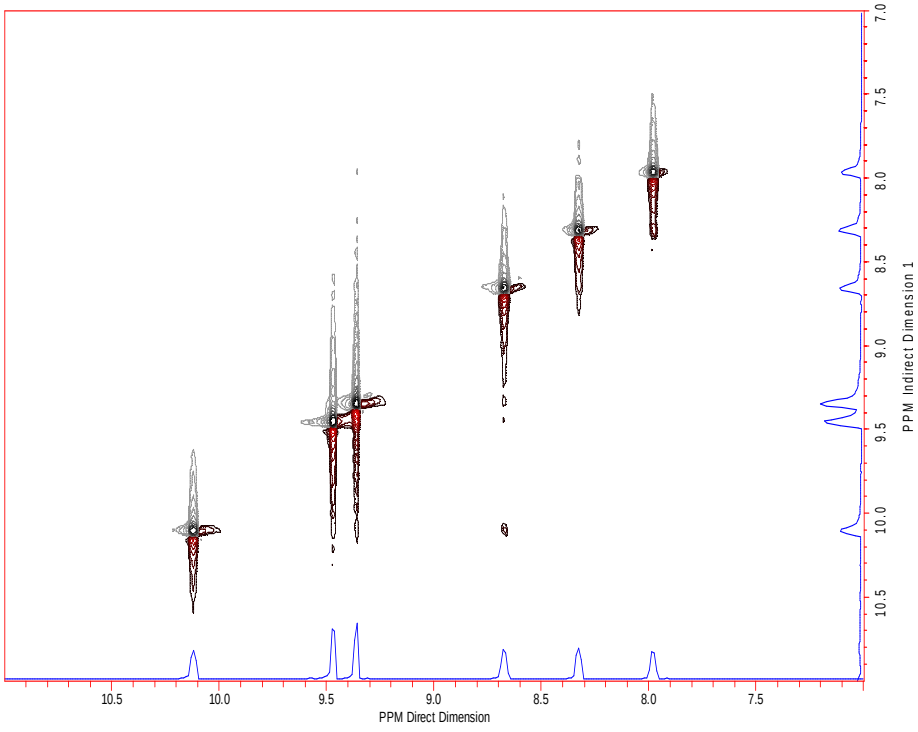

COSY ^{1}H NMR Spectrum of $[Ir(deeb)_2Cl_2](PF_6)$:

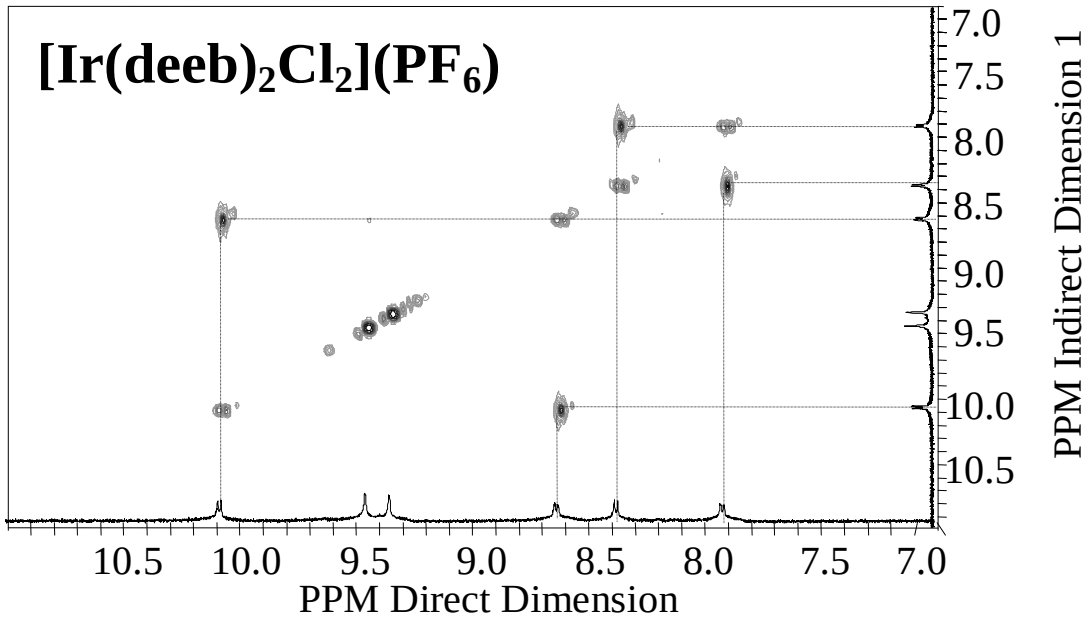

COSY ^{1}H NMR Spectrum of $[Ir(deeb)_2(dpp)](PF_6)_3$:

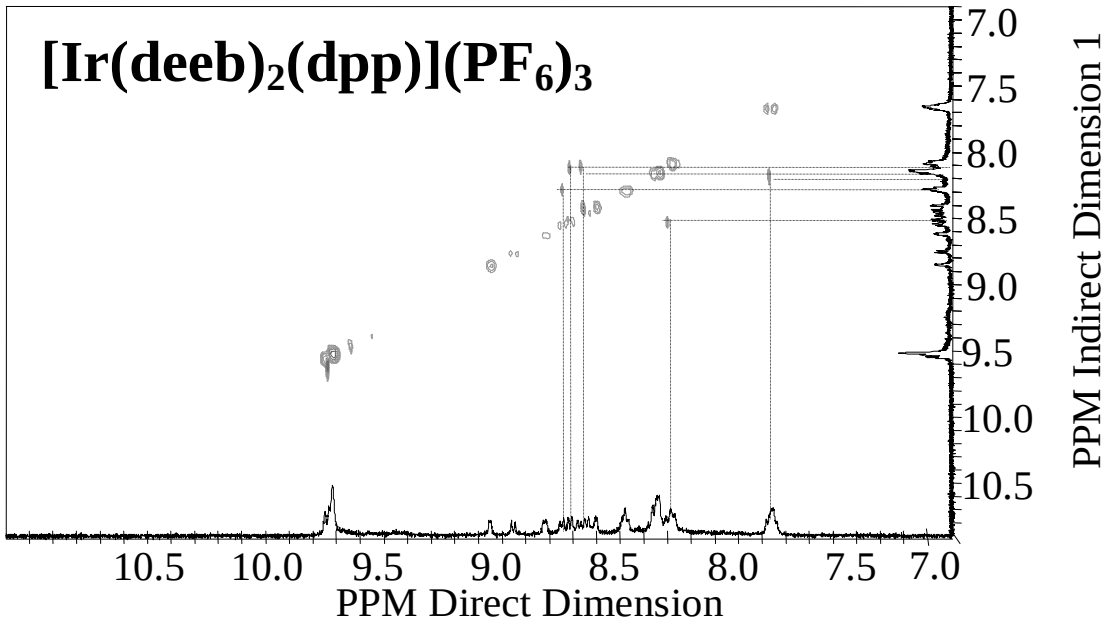

Appendix B – Mass Spectra of $[Rh(deeb)_2Cl_2](PF_6)$, $[Ir(deeb)_2Cl_2](PF_6)$ and $[Ir(deeb)_2(dpp)](PF_6)_3$

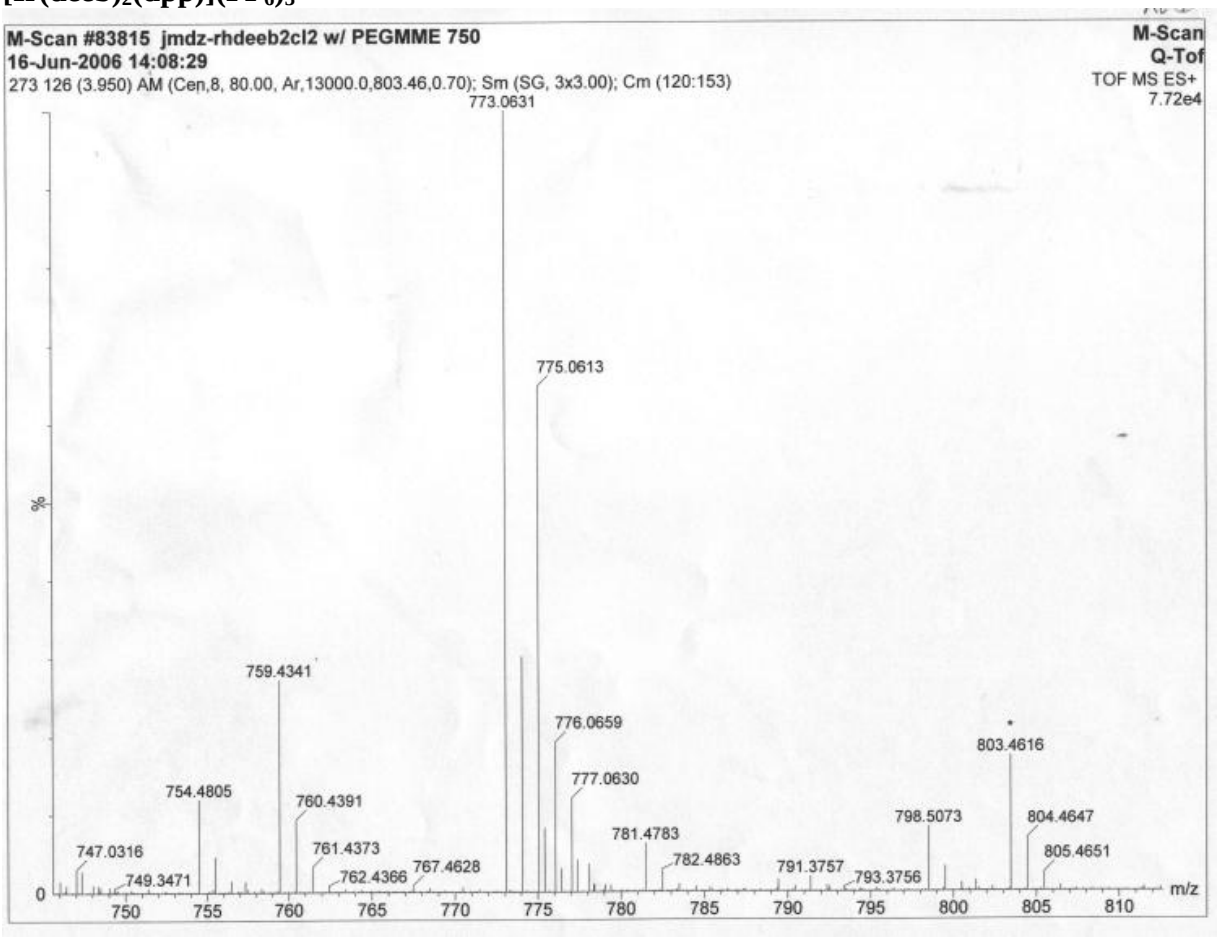

Qualitative Compound Report

Data File	jz_irdbcl_esi_3u.d	**Sample Name**	jz_irdbcl
Sample Type	Sample	**Position**	P1-C2
Instrument Name	Instrument 1	**User Name**	
Acq Method	MMI_esi_union.m	**IRM Calibration Status**	Success
DA Method	msautoproc.m	**Comment**	429210

Compound Table

Compound Label	RT	Mass	Abund	Formula	Tgt Mass	Diff (ppm)
Cpd 1: C32 H32 N4 O8 Cl2 [193Ir]	0.259	863.1207	194849	C32 H32 N4 O8 Cl2 [193Ir]	863.1226	-2.19

Compound Label	RT	Algorithm	Mass
Cpd 1: C32 H32 N4 O8 Cl2 [193Ir]	0.259	Find By Formula	863.1207

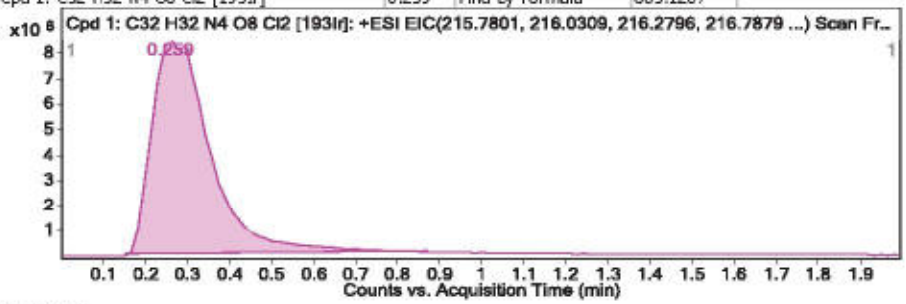

MS Spectrum

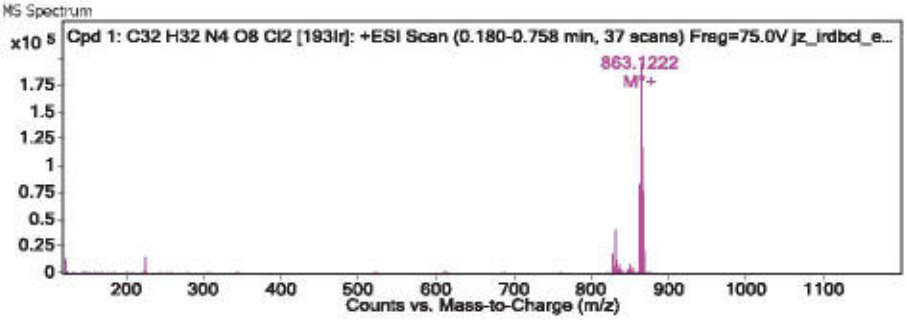

Qualitative Compound Report

MS Zoomed Spectrum

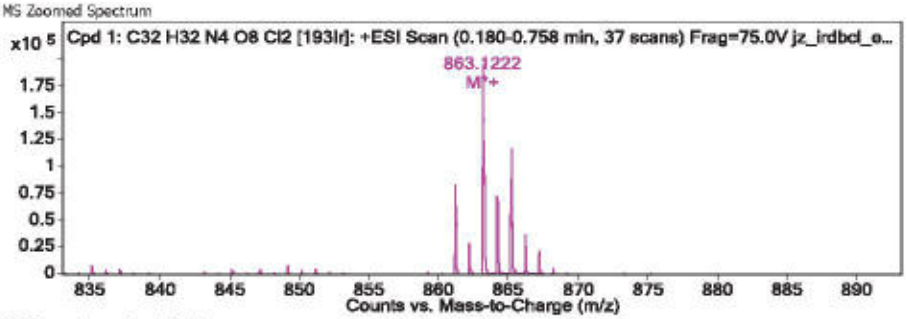

MS Spectrum Peak List

m/z	Calc m/z	Diff(ppm)	z	Abund	Formula	Ion
861.1204				83801		
862.1228				28435		
863.1222	863.1221	0.16		198712	C32 H32 N4 O8 Cl2 [193Ir]	M*+
863.3781				4571		
864.1242	864.1252	-1.2		73147	C32 H32 N4 O8 Cl2 [193Ir]	M*+
865.1204	865.1201	0.3		119206	C32 H32 N4 O8 Cl2 [193Ir]	M*+
866.1222	866.128	-6.67		37242	C32 H33 Cl2 [193Ir] N4 O8	(M+H)+
867.1189	867.1306	-13.44		20724	C32 H33 Cl2 [193Ir] N4 O8	(M+H)+
868.1201				5831		
868.1201	868.1272	-8.13	1	5831	C32 H33 Cl2 [193Ir] N4 O8	(M+H)+

--- End Of Report ---

Qualitative Compound Report

Data File	irdeeb2_dpp_esi_2u.d	**Sample Name**	irdeeb2_dpp
Sample Type	Sample	**Position**	P1-A9
Instrument Name	Instrument 1	**User Name**	
Acq Method	MMI_esi_union.m	**IRM Calibration Status**	All Ions Missed
DA Method	msautoproc.m	**Comment**	455087

Compound Table

Compound Label	RT	Mass	Abund	Formula	Tgt Mass	Diff (ppm)
Cpd 1: C46 H42 N8 O8 Ir	0.467	1025.2704	421593	C46 H42 N8 O8 Ir	1025.2732	-2.65

Compound Label	RT	Algorithm	Mass
Cpd 1: C46 H42 N8 O8 Ir	0.467	Find By Formula	1025.2704

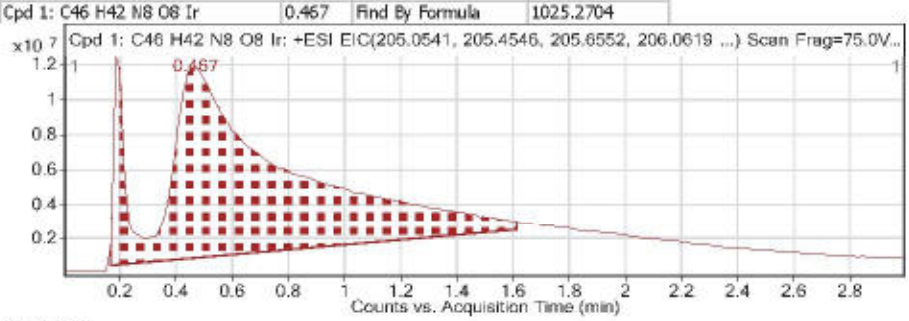

MS Spectrum

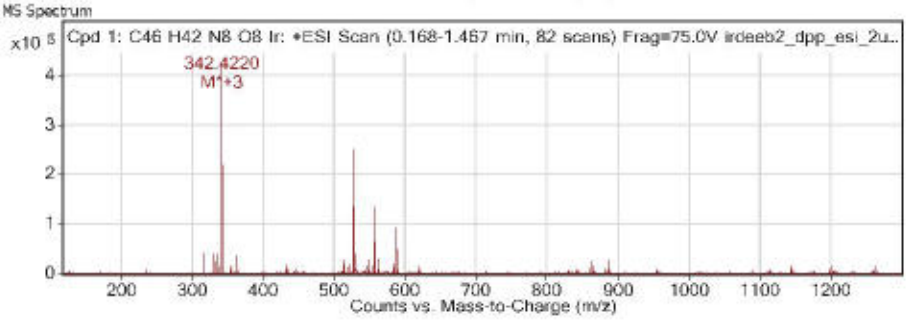

Qualitative Compound Report

MS Zoomed Spectrum

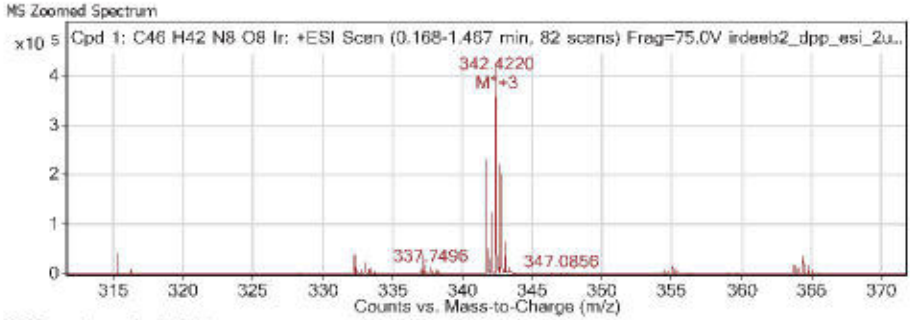

MS Spectrum Peak List

m/z	Calc m/z	Diff(ppm)	Abund	Formula	Ion
337.7496			14215		
338.2347			7237		
341.7543	341.7572	-8.4	235037	C46 H42 N8 O8 Ir	M*+3
342.0886	342.0915	-8.5	123286	C46 H42 N8 O8 Ir	M*+3
342.422	342.4247	-7.84	426006	C46 H42 N8 O8 Ir	M*+3
342.5904			14799		
342.7563			219160		
342.9244			7786		
343.0903			63640		
343.4242			14101		

--- End Of Report ---

Appendix C – EDX Spectra of Metal Complexes on Eu_2O_3 and Y_2O_3 Nanoparticles

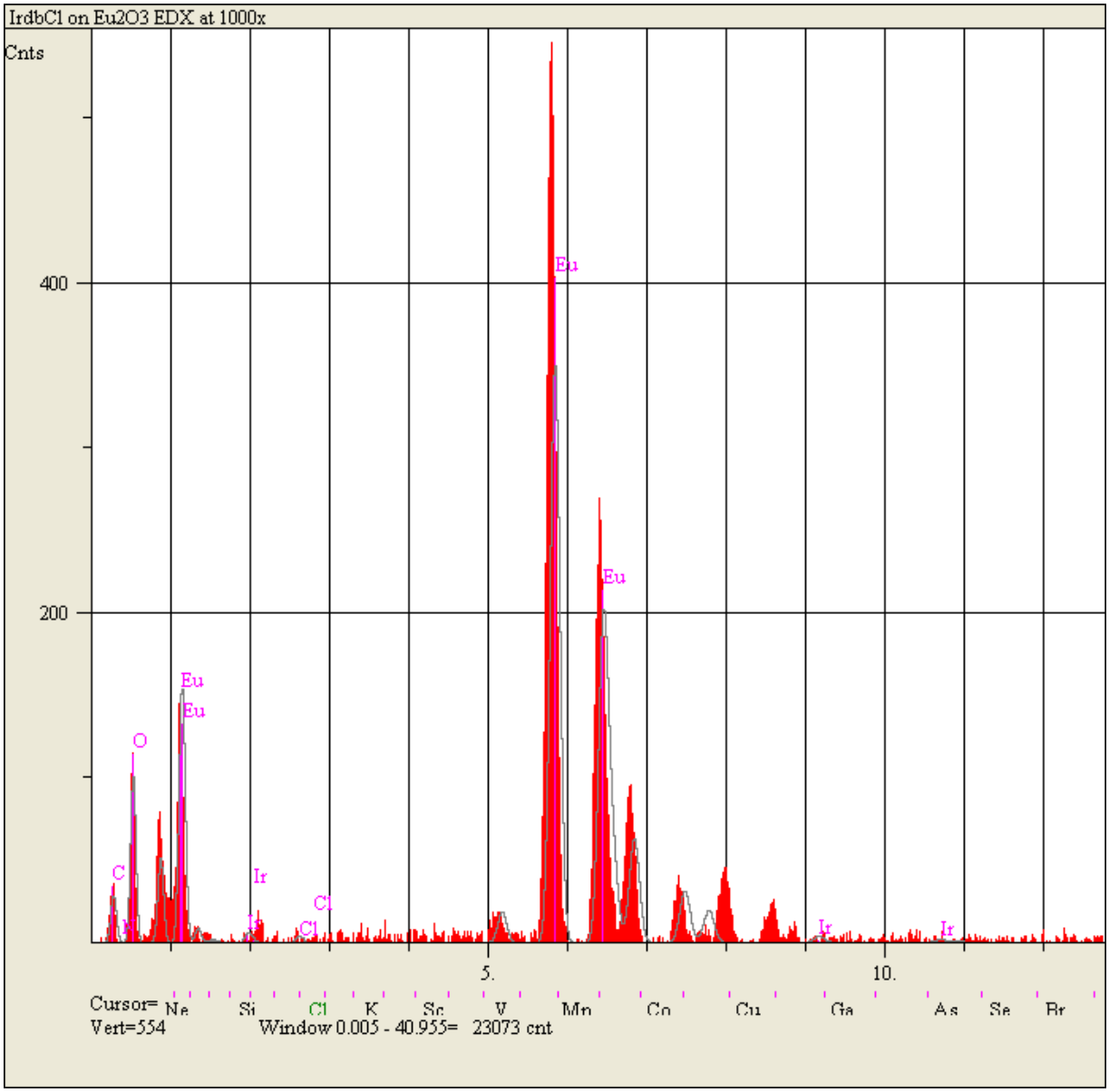

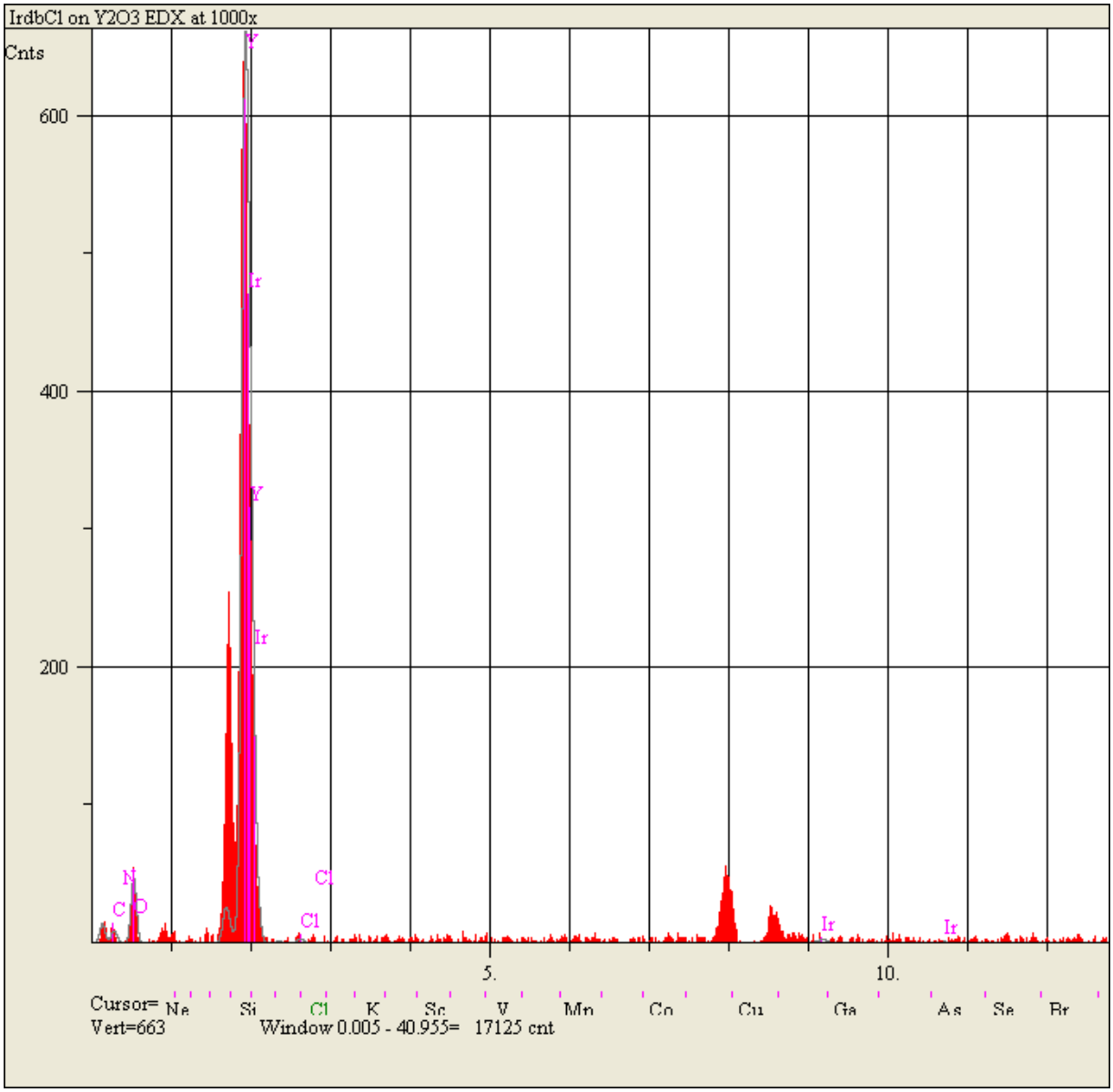
IrdbCl on Y2O3 EDX at 1000x
Cnts
600
400
200
Y
Ir
Y
Ir
N
C
O
Cl
Cl
Ir
Ir
5.
10.
Cursor= Ne Si Cl K Sc V Mn Co Cu Ga As Se Br
Vert=663
Window 0.005 - 40.955= 17125 cnt

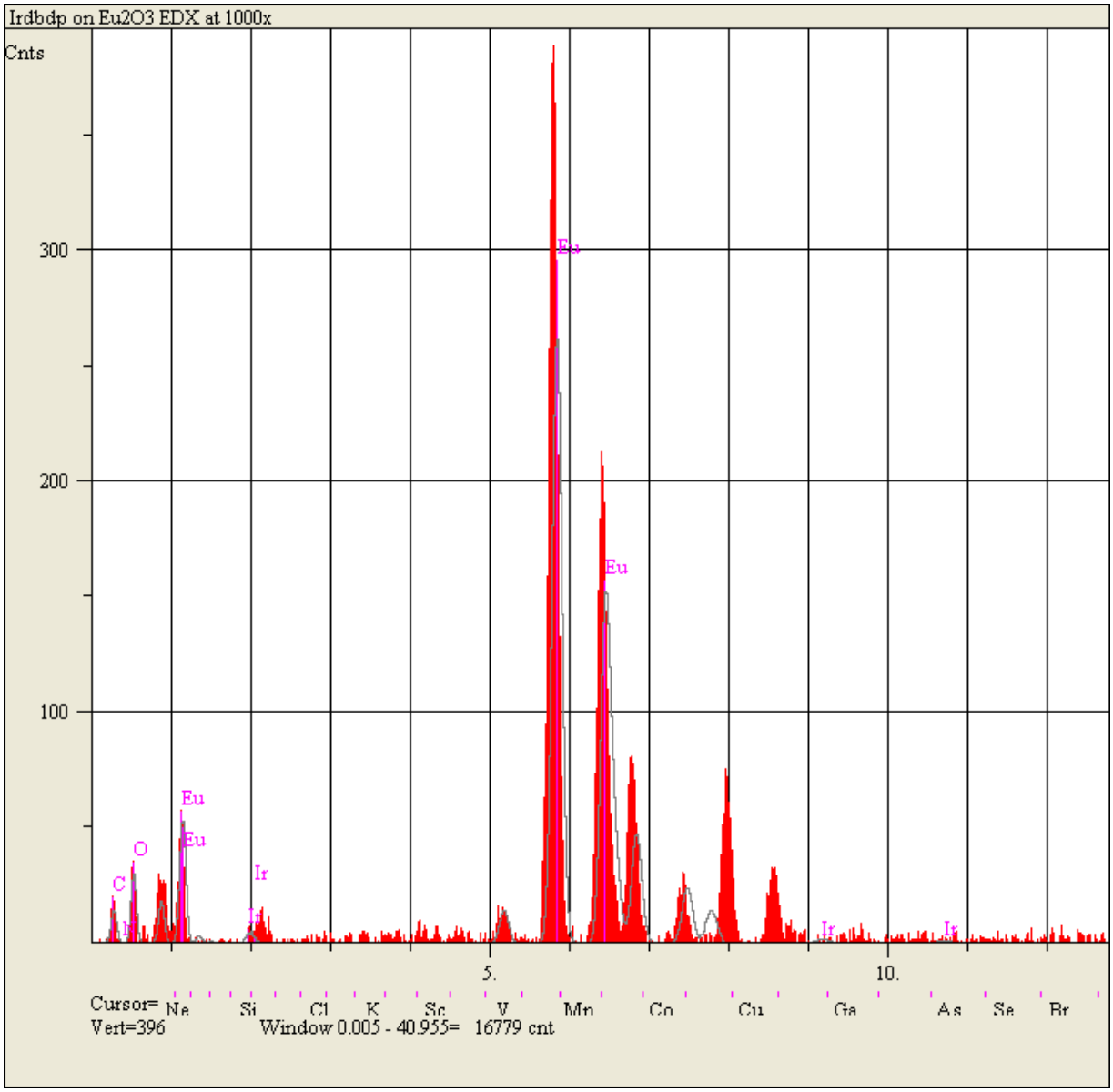
Irdbdp on Eu2O3 EDX at 1000x
Cnts
300
200
100
Eu
Eu
Eu
O
C
Ir
Ir
Ir
Ir
5.
10.
Cursor=
Vert=396
Ne
Si
Cl
K
Sc
V
Mn
Co
Cu
Ga
As
Se
Br
Window 0.005 - 40.955= 16779 cnt

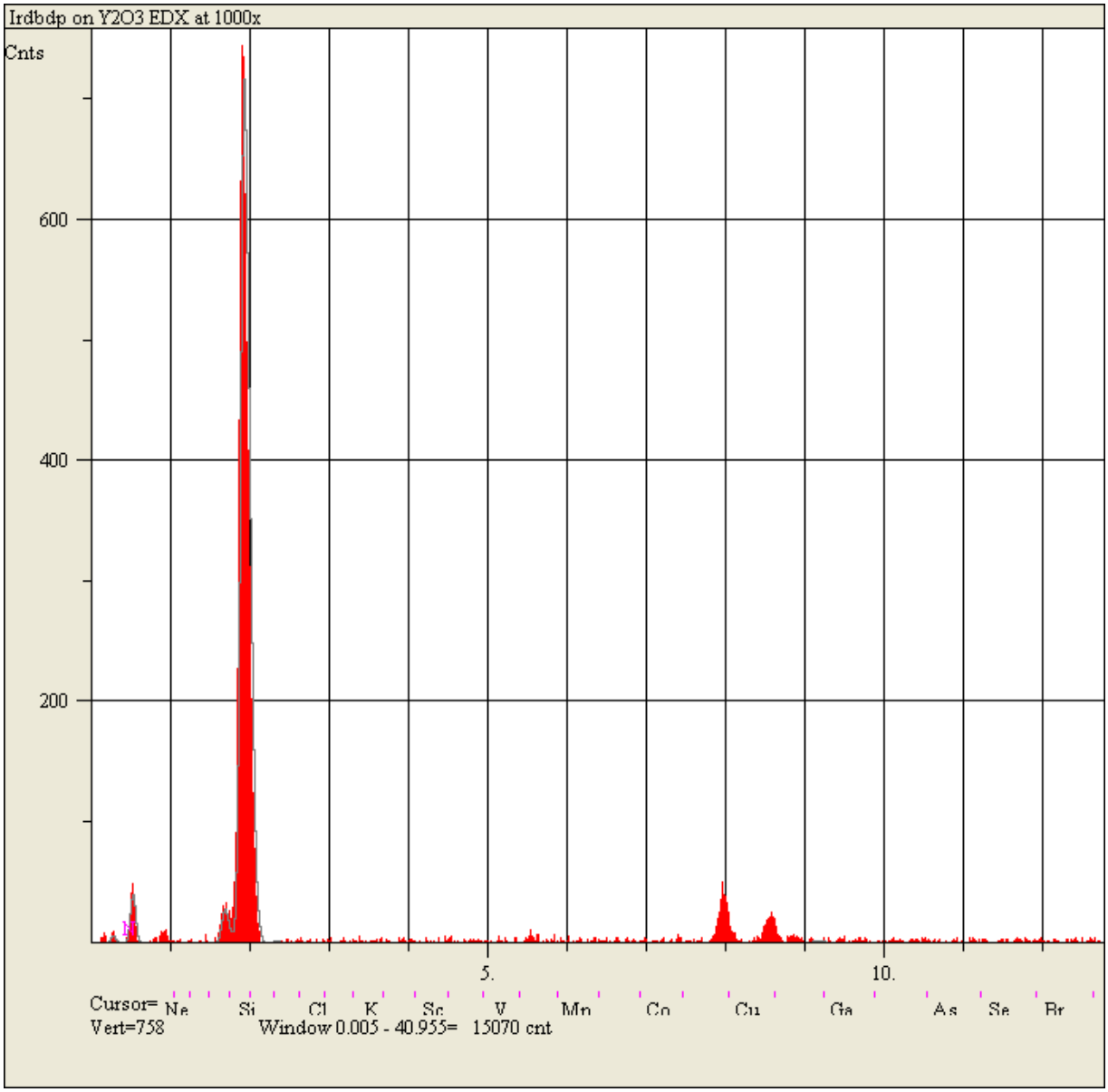
Irdbdp on Y2O3 EDX at 1000x
Cnts
600
400
200
5.
10.
Cursor= Ne Si Cl K Sc V Mn Co Cu Ga As Se Br
Vert=758
Window 0.005 - 40.955= 15070 cnt

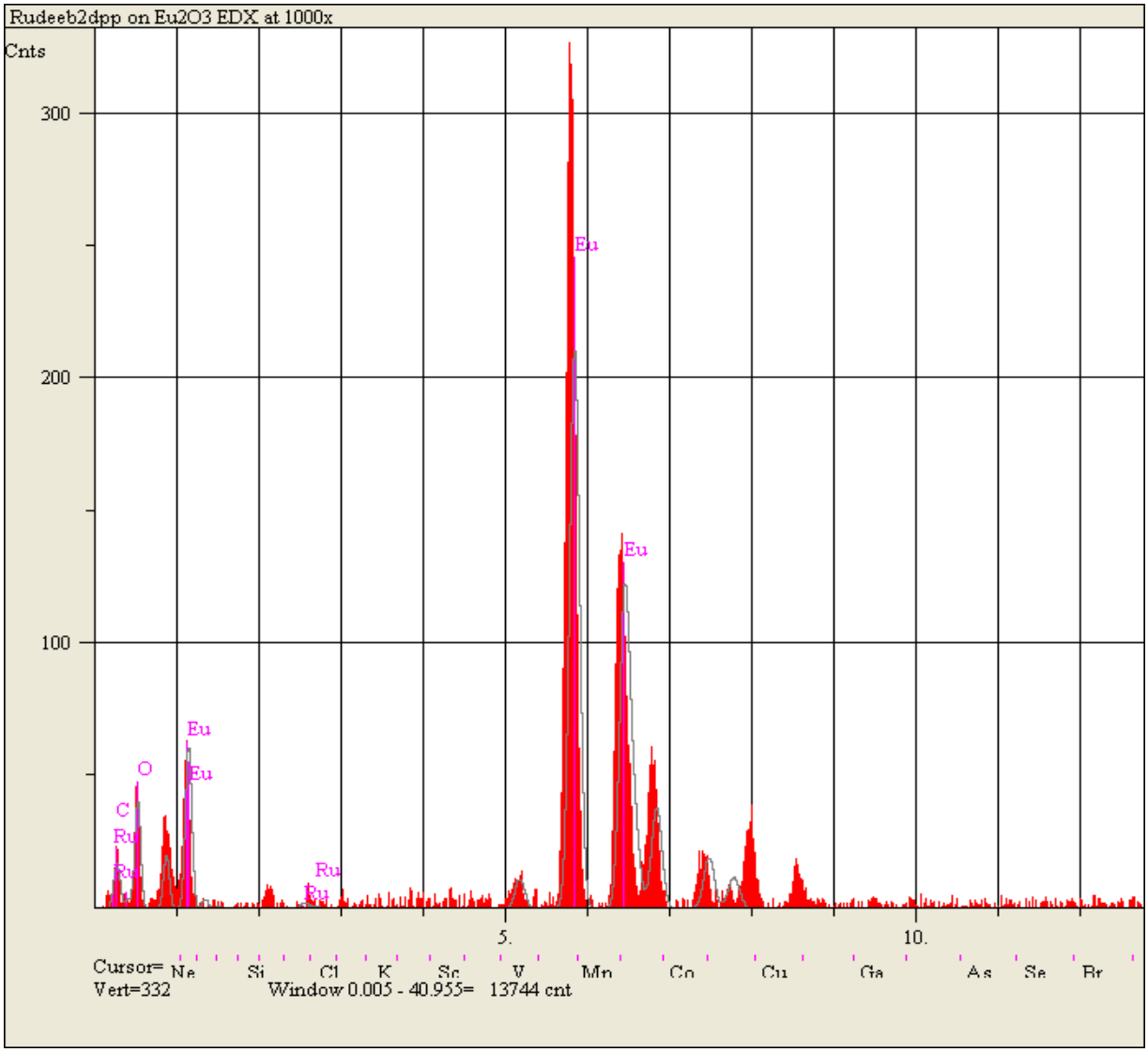
Rudeeb2dpp on Eu2O3 EDX at 1000x
Cnts
300
200
100
Eu
Eu
Eu
O
C
Ru
Ru
Ru
Ru
5.
10.
Cursor=
Vert=332
Window 0.005 - 40.955= 13744 cnt

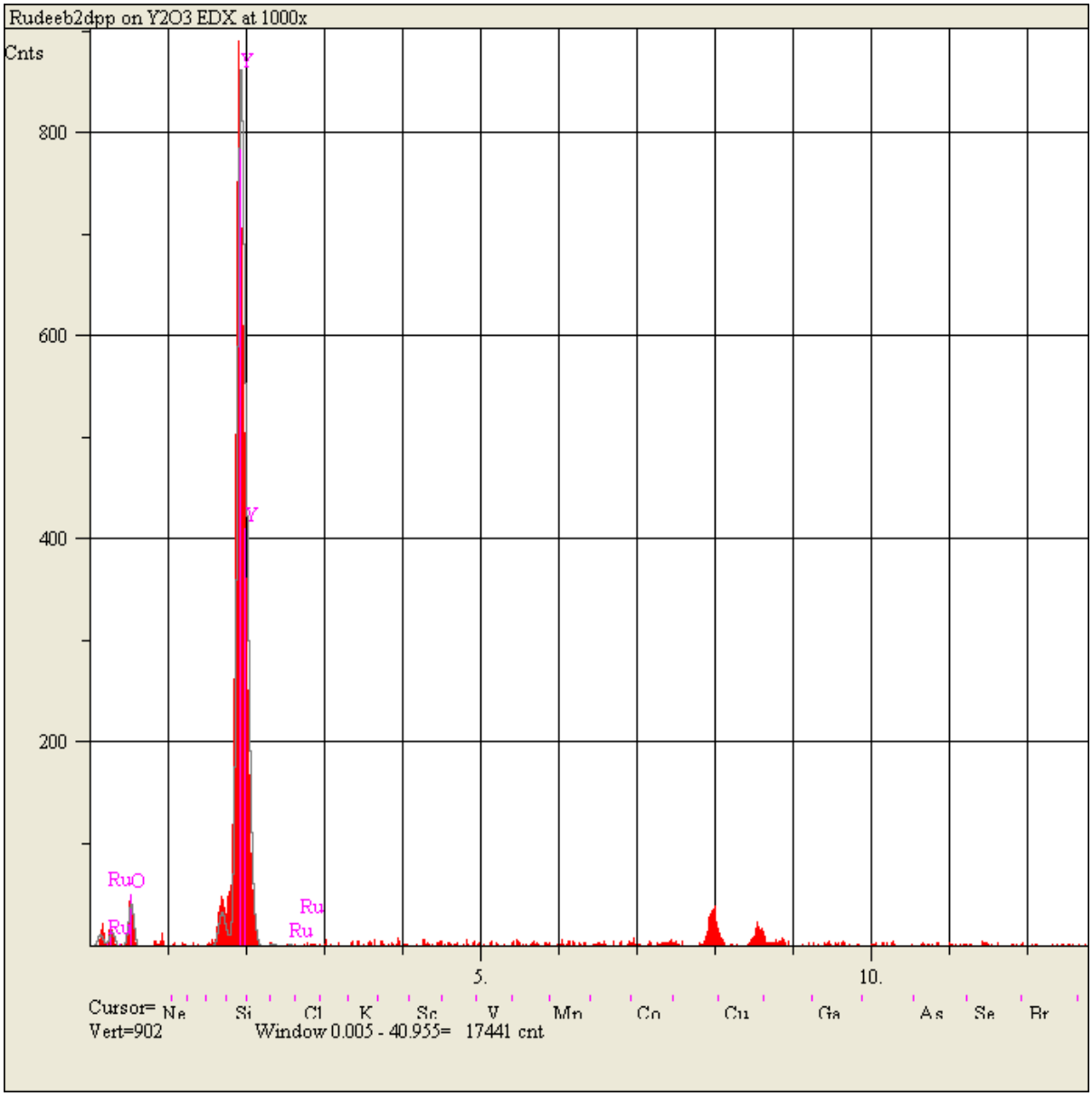
Rudeeb2dpp on Y2O3 EDX at 1000x
Cnts
800
600
400
200
Y
Y
RuO
Ru
Ru
Ru
5.
10.
Cursor=
Vert=902
Ne
Si
Cl
K
Sc
V
Mn
Co
Cu
Ga
As
Se
Br
Window 0.005 - 40.955= 17441 cnt

References

(1) Si, R.; Zhang, Y.-W.; Zhou, H.-P.; Sun, L.-D.; Yan, C.-H. *Chemistry of Materials* **2007**, *19*, 18.
(2) Yu, K.; Qiu, X.; Xu, X.; Wei, W.; Peng, B.; Zhou, Z. *Applied Physics Letters* **2007**, *90*, 091916/1.
(3) Yang, J.; Nie, Z.; Wang, Y. *Applied Surface Science* **2003**, *215*, 87.
(4) Bell, A. T. *Science (Washington, DC, United States)* **2003**, *299*, 1688.
(5) Blasse, G. *Handb. Phys. Chem. Rare Earths* **1979**, *4*, 237.
(6) Blasse, G.; Grabmaier, B. C. *Luminescent materials*; Springer-Verlag: Berlin; New York, 1994.
(7) Dieke, G. H.; Crosswhite, H. M. *Applied Optics* **1963**, *2*, 675.
(8) Dieke, G. H. *Spectra and Energy Levels of Rare Earth Ions in Crystals*; Interscience Publishers: New York, NY, 1968.
(9) Cotton, S. *Lanthanide and actinide chemistry*; Wiley: Chichester, England; Hoboken, NJ, 2006.
(10) Higgins, G. T.; Bergeron, B. V.; Hasselmann, G. M.; Farzad, F.; Meyer, G. J. *Journal of Physical Chemistry B* **2006**, *110*, 2598.
(11) Meyer, G. J. *Inorganic Chemistry* **2005**, *44*, 6852.
(12) Meyer, G. J. *Journal of Photochemistry and Photobiology, A: Chemistry* **2003**, *158*, 119.
(13) Qu, P.; Meyer, G. J. *Langmuir* **2001**, *17*, 6720.
(14) Qu, P.; Thompson, D. W.; Meyer, G. J. *Langmuir* **2000**, *16*, 4662.
(15) Kelly, C. A.; Farzad, F.; Thompson, D. W.; Stipkala, J. M.; Meyer, G. J. *Langmuir* **1999**, *15*, 7047.
(16) Kelly, C. A.; Farzad, F.; Thompson, D. W.; Meyer, G. J. *Langmuir* **1999**, *15*, 731.
(17) Blasse, G.; Sabbatini, N. *Materials Chemistry and Physics* **1987**, *16*, 237.
(18) Gschneidner, K. A.; Eyring, L. *Handbook on the physics and chemistry of rare earths*; North-Holland ; sole distributors for the U.S.A. and Canada, Elsevier North-Holland: Amsterdam; New York; New York, NY, USA, 1994; Vol. 18.
(19) Balzani, V.; Bergamini, G.; Ceroni, P. *Coordination Chemistry Reviews* **2008**, *252*, 2456.
(20) Ward, M. D. *Annual Reports Section "A" (Inorganic Chemistry)* **2005**, *101*, 649.
(21) Rao, C. N. R.; Mueller, A.; Cheetham, A. K.; Editors *The Chemistry of Nanomaterials: Synthesis, Properties and Applications in 2 Volumes. (Volume 1 or 2) [In: Chem. Nanomater.; 2004, 1]*, 2004.
(22) Charra, F.; Gota-Goldmann, S. *Springer Handbook of Condensed Matter and Materials Data* **2005**, 1031.
(23) Flytzanis, C. *Journal of Physics B: Atomic, Molecular and Optical Physics* **2005**, *38*, S661.
(24) Zhang, L. Z.; Sun, W.; Cheng, P. *Molecules* **2003**, *8*, 207.
(25) Hase, T.; Kano, T.; Nakazawa, E.; Yamamoto, H. In *Advances in Electronics and Electron Physics*; Peter, W. H., Ed.; Academic Press: 1990; Vol. Volume 79, p 271.
(26) Trice, B. E.; Tissue, B. M. *Spectroscopy Letters* **2007**, *40*, 333.
(27) Bünzli, J.-C. G.; Comby, S.; Chauvin, A.-S.; Vandevyver, C. D. B. *Journal of Rare Earths* **2007**, *25*, 257.
(28) Tanner, P. A.; Duan, C.-K. *Coordination Chemistry Reviews* **2010**, *254*, 3026.

(29) Faulkner, S.; Natrajan, L. S.; Perry, W. S.; Sykes, D. *Dalton Transactions* **2009**, 3890.
(30) Iki, N. *Supramolecular Chemistry* **2011**, *23*, 160.
(31) Alstrum-Acevedo, J. H.; Brennaman, M. K.; Meyer, T. J. *Inorganic Chemistry* **2005**, *44*, 6802.
(32) Balzani, V.; Juris, A.; Venturi, M.; Campagna, S.; Serroni, S. *Chemical Reviews (Washington, D. C.)* **1996**, *96*, 759.
(33) Flamigni, L.; Barbieri, A.; Sabatini, C.; Ventura, B.; Barigelletti, F. *Topics in Current Chemistry* **2007**, *281*, 143.
(34) Ardo, S.; Meyer, G. J. *Chemical Society Reviews* **2009**, *38*, 115.
(35) Gratzel, M. *Accounts of Chemical Research* **2009**, *42*, 1788.
(36) O'Regan, B.; Graetzel, M. *Nature (London, United Kingdom)* **1991**, *353*, 737.
(37) Indelli, M. T.; Bignozzi, C. A.; Harriman, A.; Schoonover, J. R.; Scandola, F. *Journal of the American Chemical Society* **1994**, *116*, 3768.
(38) Lei, Y.; Buranda, T.; Endicott, J. F. *Journal of the American Chemical Society* **1990**, *112*, 8820.
(39) Dixon, I. M.; Collin, J. P.; Sauvage, J. P.; Flamigni, L.; Encinas, S.; Barigelletti, F. *Chemical Society Reviews* **2000**, *29*, 385.
(40) Clemente-Leon, M.; Coronado, E.; Lopez-Munoz, A.; Repetto, D.; Ito, T.; Konya, T.; Yamase, T.; Constable, E. C.; Housecroft, C. E.; Doyle, K.; Graber, S. *Langmuir* **2010**, *26*, 1316.
(41) Coppo, P.; Duati, M.; Kozhevnikov, V. N.; Hofstraat, J. W.; De Cola, L. *Angewandte Chemie, International Edition* **2005**, *44*, 1806.
(42) Chen, F.-F.; Bian, Z.-Q.; Liu, Z.-W.; Nie, D.-B.; Chen, Z.-Q.; Huang, C.-H. *Inorganic Chemistry (Washington, DC, United States)* **2008**, *47*, 2507.
(43) Tart, N. M.; Sykes, D.; Sazanovich, I.; Tidmarsh, I. S.; Ward, M. D. *Photochemical & Photobiological Sciences* **2010**, *9*, 886.
(44) Chen, F. F.; Bian, Z. Q.; Lou, B.; Ma, E.; Liu, Z. W.; Nie, D. B.; Chen, Z. Q.; Bian, J.; Chen, Z. N.; Huang, C. H. *Dalton Transactions* **2008**, 5577.
(45) Chen, Z. Q.; Bian, Z. Q.; Huang, C. H. *Advanced Materials (Weinheim, Germany)* **2010**, *22*, 1534.
(46) Rasmussen, S. C.; Richter, M. M.; Yi, E.; Place, H.; Brewer, K. J. *Inorganic Chemistry* **1990**, *29*, 3926.
(47) Cavazzini, M.; Quici, S.; Scalera, C.; Puntoriero, F.; La Ganga, G.; Campagna, S. *Inorganic Chemistry (Washington, DC, United States)* **2009**, *48*, 8578.
(48) Sabatini, C.; Barbieri, A.; Barigelletti, F.; Arm, K. J.; Williams, J. A. G. *Photochemical & Photobiological Sciences* **2007**, *6*, 397.
(49) Welter, S.; Lafolet, F.; Cecchetto, E.; Vergeer, F.; De Cola, L. *ChemPhysChem* **2005**, *6*, 2417.
(50) Whittle, V. L.; Williams, J. A. G. *Dalton Transactions* **2009**, 3929.
(51) Gratzel, M. *Inorganic chemistry* **2005**, *44*, 6841.
(52) Alstrum-Acevedo, J. H.; Brennaman, M. K.; Meyer, T. J. *Inorganic Chemistry* **2005**, *44*, 6802.
(53) Bisquert, J.; Cahen, D.; Hodes, G.; Ruehle, S.; Zaban, A. *Journal of Physical Chemistry B* **2004**, *108*, 8106.
(54) Ramamurthy, V.; Schanze, K. S. *Semiconductor Photochemistry and Photophysics. [In: Mol. Supramol. Photochem., 2003; 10]*, 2003.

(55) Charbonniere, L. J.; Hildebrandt, N.; Ziessel, R. F.; Loehmannsroeben, H.-G. *Journal of the American Chemical Society* **2006**, *128*, 12800.
(56) Hildebrandt, N.; Charbonniere, L.; Ziessel, R. F.; Loehmannsroeben, H.-G. *Proceedings of SPIE-The International Society for Optical Engineering* **2006**, *6191*, 61910W/1.
(57) Hildebrandt, N.; Charbonniere, L. J.; Beck, M.; Ziessel, R. F.; Loehmannsroeben, H.-G. *Angewandte Chemie, International Edition* **2005**, *44*, 7612.
(58) Beck, M.; Hildebrandt, N.; Loehmannsroeben, H.-G. *Proceedings of SPIE-The International Society for Optical Engineering* **2006**, *6191*, 61910X/1.
(59) Yanagida, S. *Comptes Rendus Chimie* **2006**, *9*, 597.
(60) Altobello, S.; Argazzi, R.; Caramori, S.; Contado, C.; Da Fre, S.; Rubino, P.; Chone, C.; Larramona, G.; Bignozzi, C. A. *Journal of the American Chemical Society* **2005**, *127*, 15342.
(61) Trammell, S. A.; Meyer, T. J. *Langmuir* **2003**, *19*, 6081.
(62) Trammell, S. A.; Yang, J.; Sykora, M.; Fleming, C. N.; Odobel, F.; Meyer, T. J. *Journal of Physical Chemistry B* **2001**, *105*, 8895.
(63) Meyer, T. J.; Meyer, G. J.; Pfennig, B. W.; Schoonover, J. R.; Timpson, C. J.; Wall, J. F.; Kobusch, C.; Chen, X.; Peek, B. M.; et al. *Inorganic Chemistry* **1994**, *33*, 3952.
(64) Yan, S. G.; Hupp, J. T. *Journal of Physical Chemistry B* **1997**, *101*, 1493.
(65) Hoertz, P. G.; Staniszewski, A.; Marton, A.; Higgins, G. T.; Incarvito, C. D.; Rheingold, A. L.; Meyer, G. J. *Journal of the American Chemical Society* **2006**, *128*, 8234.
(66) Liu, F.; Meyer, G. J. *Inorganic Chemistry* **2005**, *44*, 9305.
(67) Lee, S.; Park, K.; Kim, K.; Choi, K.; Kwon, I. C. *Chem. Commun. (Cambridge, U. K.)* **2008**, 4250.
(68) Miller, J. N. *Analyst (Cambridge, U. K.)* **2005**, *130*, 265.
(69) Roda, A.; Guardigli, M.; Michelini, E.; Mirasoli, M. *Anal. Bioanal. Chem.* **2009**, *393*, 109.
(70) Sahoo, H. *J. Photochem. Photobiol., C* **2011**, *12*, 20.
(71) Buenzli, J.-C. G. *Chem. Rev. (Washington, DC, U. S.)* **2010**, *110*, 2729.
(72) Laquai, F.; Park, Y.-S.; Kim, J.-J.; Basche, T. *Macromol. Rapid Commun.* **2009**, *30*, 1203.
(73) Ye, S.; Xiao, F.; Pan, Y. X.; Ma, Y. Y.; Zhang, Q. Y. *Mater. Sci. Eng., R* **2010**, *R71*, 1.
(74) Zhang, Q. Y.; Huang, X. Y. *Prog. Mater. Sci.* **2010**, *55*, 353.
(75) Forster, T. *Discussions of the Faraday Society* **1959**, *No. 27*, 7.
(76) Dexter, D. L. *Journal of Chemical Physics* **1953**, *21*, 836.
(77) Montalti, M. A. C. L. P. M. T. G. *Handbook of Photochemistry*; Third ed.; Taylor & Francis Group: FL, 2006.
(78) Van Der Meer, B. W.; Coker, G., III; Chen, S. S. Y. *Resonance Energy Transfer: Theory and Data*, 1994.
(79) Henderson, B. I., G.F. *Optical Spectroscopy of Inorganic Solids*; Oxford University Press: NY, 1989.
(80) Inokuti, M.; Hirayama, F. *Journal of Chemical Physics* **1965**, *43*, 1978.
(81) Selvin, P. R. *IEEE Journal of Selected Topics in Quantum Electronics* **1996**, *2*, 1077.
(82) Porter, G. B. *Journal of Chemical Education* **1983**, *60*, 785.
(83) Kuhn, H. J.; Braslavsky, S. E.; Schmidt, R. *Pure and Applied Chemistry* **2004**, *76*, 2105.
(84) Simons, J. P. *Photochemistry and spectroscopy*; Wiley-Interscience: London; New York, 1971.
(85) Lakowicz, J. R.; SpringerLink; Springer: New York, 2006.

(86) Mehlstaeubl, M.; Kottas, G. S.; Colella, S.; De Cola, L. *Dalton Transactions* **2008**, 2385.
(87) Joshi, B. C. *Journal of Non-Crystalline Solids* **1995**, *180*, 217.
(88) Ishizaka, T.; Nozaki, R.; Kurokawa, Y. *Journal of Physics and Chemistry of Solids* **2002**, *63*, 613.
(89) Li, Q.; Li, T.; Wu, J. *J. Phys. Chem. B* **2001**, *105*, 12293.
(90) Anh, T. K.; Benalloul, P.; Barthou, C.; Giang, L. T. K.; Vu, N.; Minh, L. Q. *Journal of Nanomaterials* **2007**, 1.
(91) Anh, T. K.; Minh, L. Q.; Vu, N.; Huong, T. T.; Huong, N. T.; Barthou, C.; Strek, W. *J. Lumin.* **2003**, *102-103*, 391.
(92) Singh, L. R.; Ningthoujam, R. S. *Journal of Applied Physics* **2010**, *107*, 104304/1.
(93) Wang, D. D.; Xing, G. Z.; Yang, J. H.; Yang, L. L.; Gao, M.; Cao, J.; Zhang, Y. J.; Yao, B. *Journal of Alloys and Compounds* **2010**, *504*, 22.
(94) Fu, L.; Liu, Z.; Liu, Y.; Han, B.; Wang, J.; Hu, P.; Cao, L.; Zhu, D. *J. Phys. Chem. B* **2004**, *108*, 13074.
(95) Bunzli Jean-Claude, G.; Piguet, C. *Chem Soc Rev* **2005**, *34*, 1048.
(96) Casanova, D.; Giaume, D.; Beaurepaire, E.; Gacoin, T.; Boilot, J.-P.; Alexandrou, A. *Applied Physics Letters* **2006**, *89*, 253103/1.
(97) Casanova, D.; Giaume, D.; Gacoin, T.; Boilot, J.-P.; Alexandrou, A. *Journal of Physical Chemistry B* **2006**, *110*, 19264.
(98) Casanova, D.; Giaume, D.; Amirtha, T.; Gacoin, T.; Boilot, J. P.; Alexandrou, A. *Proceedings of SPIE-The International Society for Optical Engineering* **2006**, *6096*, 60960J/1.
(99) Zhang, L.; Liu, H.-G.; Kang, S.-Z.; Mu, Y.-D.; Qian, D.-J.; Lee, Y.-I.; Feng, X.-S. *Thin Solid Films* **2005**, *491*, 217.
(100) Zhang, M.-S.; Yin, W.; Su, Q.; Zhang, H.-J. *Materials Letters* **2002**, *57*, 940.
(101) Clapp, A. R.; Medintz, I. L.; Mattoussi, H. *ChemPhysChem* **2006**, *7*, 47.
(102) Clapp, A. R.; Medintz, I. L.; Fisher, B. R.; Anderson, G. P.; Mattoussi, H. *Journal of the American Chemical Society* **2005**, *127*, 1242.
(103) Sykora, M.; Petruska, M. A.; Alstrum-Acevedo, J.; Bezel, I.; Meyer, T. J.; Klimov, V. I. *Journal of the American Chemical Society* **2006**, *128*, 9984.
(104) Wolfbauer, G.; Bond, A. M.; MacFarlane, D. R. *Inorganic Chemistry* **1999**, *38*, 3836.
(105) Bergeron, B. V.; Meyer, G. J. *Journal of Physical Chemistry B* **2003**, *107*, 245.
(106) Rasmussen, S. C.; Richter, M. M.; Yi, E.; Place, H.; Brewer, K. J. *Inorganic Chemistry* **1990**, *29*, 3926.
(107) Elemental analysis showed C, 39.7%, H, 3.2%, N, 5.8% (calculated C, 41.8%, H, 3.5%, N, 6.1%).
(108) Eilers, H.; Tissue, B. M. *Mater. Lett.* **1995**, *24*, 261.
(109) Eilers, H.; Tissue, B. M. *Materials Letters* **1995**, *24*, 261.
(110) Panayotov, D. A.; Burrows, S. P.; Morris, J. R. *J. Phys. Chem. C* **2012**, *116*, 6623.
(111) Gottlieb, H. E.; Kotlyar, V.; Nudelman, A. *The Journal of Organic Chemistry* **1997**, *62*, 7512.
(112) Hermann, R.; Graetzel, M.; Nissen, H. U.; Shklover, V.; Nazeeruddin, M. K.; Zakeeruddin, S. M.; Barbe, C.; Kay, A.; Haibach, T.; Steurer, W. *Chemistry of Materials* **1997**, *9*, 430.
(113) Zapiter, J. M. D.; Tissue, B. M.; Brewer, K. J. *Inorganic Chemistry Communications* **2008**, *11*, 51.
(114) DeSimone, R. E.; Drago, R. S. *Inorganic Chemistry* **1969**, *8*, 2517.

(115) Demas, J. N.; Harris, E. W.; Flynn, C. M., Jr.; Diemente, D. *Journal of the American Chemical Society* **1975**, *97*, 3838.
(116) Watts, R. J.; Efrima, S.; Metiu, H. *Journal of the American Chemical Society* **1979**, *101*, 2742.
(117) Divisia, B.; Ford, P. C.; Watts, R. J. *Journal of the American Chemical Society* **1980**, *102*, 7264.
(118) He, W.; Zu, D.-j.; Liu, D.-m.; Cheng, R. *Inorganica Chimica Acta* **2011**, *365*, 78.
(119) Talarico, A. M.; Aiello, I.; Bellusci, A.; Crispini, A.; Ghedini, M.; Godbert, N.; Pugliese, T.; Szerb, E. *Dalton Transactions* **2010**, *39*, 1709.
(120) Watts, R. J.; Missimer, D. *Journal of the American Chemical Society* **1978**, *100*, 5350.
(121) Flynn, C. M., Jr.; Demas, J. N. *J. Amer. Chem. Soc.* **1974**, *96*, 1959.
(122) Kahl, J. L.; Hanck, K. W.; DeArmond, K. *Journal of Physical Chemistry* **1978**, *82*, 540.
(123) Tissue, B. M.; Bihari, B. *Journal of Fluorescence* **1998**, *8*, 289.
(124) Doss, C. J.; Zallen, R. *Physical Review B: Condensed Matter and Materials Physics* **1993**, *48*, 15626.
(125) Mo, Z.; Deng, Z.; Guo, R.; Fu, Q.; Feng, C.; Liu, P.; Sun, Y. *Materials Science and Engineering: B* **2012**, *177*, 121.
(126) Benfer, S.; Hofmann, P.; Knozinger, E. *J. Mol. Struct.* **1997**, *410-411*, 115.
(127) Mahajan, S. V.; Dickerson, J. H. *Nanotechnology* **2007**, *18*, 325605/1.
(128) Goldsmith, J. A.; Ross, S. D. *Spectrochimica Acta Part A: Molecular Spectroscopy* **1967**, *23*, 1909.
(129) Tang, C.-q.; Tang, R.-r.; Tang, C.-h.; Zeng, Z.-w. *Bull. Korean Chem. Soc.* **2010**, *31*, 1283.
(130) Runde, W.; Van Pelt, C.; Allen, P. G. *Journal of Alloys and Compounds* **2000**, *303–304*, 182.
(131) Hussein, G. A. M.; Gates, B. C. *J. Catal.* **1998**, *176*, 395.
(132) Baltrusaitis, J.; Schuttlefield, J.; Zeitler, E.; Grassian, V. H. *Chem. Eng. J. (Amsterdam, Neth.)* **2011**, *170*, 471.
(133) Suarez, D. L.; Goldberg, S.; Su, C. In *Mineral-Water Interfacial Reactions*; American Chemical Society: 1999; Vol. 715, p 136.
(134) White, W. B. *Appl. Spectrosc.* **1967**, *21*, 167.
(135) Skandan, G.; Foster, C. M.; Frase, H.; Ali, M. N.; Parker, J. C.; Hahn, H. *Nanostruct. Mater.* **1992**, *1*, 313.
(136) Dexpert-Ghys, J.; Faucher, M.; Caro, P. *Physical Review B: Condensed Matter and Materials Physics* **1981**, *23*, 607.
(137) Sheng, K. C.; Korenowski, G. M. *Journal of Physical Chemistry* **1988**, *92*, 50.
(138) Bihari, B.; Eilers, H.; Tissue, B. M. *Journal of Luminescence* **1997**, *75*, 1.
(139) Renouard, T.; Fallahpour, R. A.; Nazeeruddin, M. K.; Humphry-Baker, R.; Gorelsky, S. I.; Lever, A. B. P.; Grätzel, M. *Inorganic Chemistry* **2002**, *41*, 367.
(140) Kubelka, P. *J. Opt. Soc. Am.* **1948**, *38*, 448.
(141) Torrents, A.; Stone, A. T. *Environ. Sci. Technol.* **1991**, *25*, 143.
(142) Argazzi, R.; Bignozzi, C. A.; Heimer, T. A.; Castellano, F. N.; Meyer, G. J. *Inorganic Chemistry* **1994**, *33*, 5741.
(143) Meyer, T. J.; Meyer, G. J.; Pfennig, B. W.; Schoonover, J. R.; Timpson, C. J.; Wall, J. F.; Kobusch, C.; Chen, X.; Peek, B. M.; et al. *Inorganic Chemistry* **1994**, *33*, 3952.
(144) Pretsch, E.; Bühlmann, P.; Badertscher, M. **2009**, 1.

(145) Toupet, L.; Dixneuf, P. H.; Akkurt, M.; Daoudi, M.; Sam, N.; Kerbal, A.; Chohan, Z. H.; Ben, H. T. *J. Chem. Crystallogr.* **2009**, *39*, 423.
(146) Bergeron Bryan, V.; Marton, A.; Oskam, G.; Meyer Gerald, J. *The journal of physical chemistry. B* **2005**, *109*, 937.
(147) Hoertz, P. G.; Staniszewski, A.; Marton, A.; Higgins, G. T.; Incarvito, C. D.; Rheingold, A. L.; Meyer, G. J. *Journal of the American Chemical Society* **2006**, *128*, 8234.
(148) Dakhel, A. A. *The European Physical Journal - Applied Physics* **2004**, *28*, 59.
(149) Hou, Y.-j.; Xie, P.-h.; Zhang, B.-w.; Cao, Y.; Xiao, X.-r.; Wang, W.-b. *Inorganic Chemistry* **1999**, *38*, 6320.
(150) Heimer, T. A.; D'Arcangelis, S. T.; Farzad, F.; Stipkala, J. M.; Meyer, G. J. *Inorganic Chemistry* **1996**, *35*, 5319.
(151) Zapiter, J. M. D., Tissue, Brian M., Brewer, Karen J. *Journal of Coordination Chemistry* **2011**, *Manuscript in preparation.*
(152) Kubelka, P. *J. Opt. Soc. Am.* **1948**, *38*, 448.